Acoustic particle detection

Direction and source location reconstruction techniques

Akustische Teilchendetektion
Richtungs- und Ortsrekonstruktionsstrategien

Der Naturwissenschaftlichen Fakultät
der Friedrich-Alexander-Universität Erlangen-Nürnberg
zur
Erlangung des Doktorgrades Dr. rer. nat.

vorgelegt von
Carsten Richardt

aus Nördlingen

Als Dissertation genehmigt von den Naturwissenschaftlichen Fakultäten
der Universität Erlangen-Nürnberg

Tag der mündlichen Prüfung:	29. Juli 2010
Vorsitzender der Promotionskommision:	Prof. Dr. Eberhard Bänsch
Erstberichterstatter:	Prof. Dr. Gisela Anton
Zweitberichterstatter:	Prof. Dr. Klaus Helbing

Contents

Chapter 1

Introduction

...Space, the final frontier. These are the voyages of the Starship Enterprise. Its five year mission: to explore strange new worlds. To seek out new life and new civilizations. To boldly go where no man has gone before... [1]

Unlike the Starship Enterprise, we are bound to our home planet and its immediate surrounding to explore the mysteries of the Universe. For centuries this was done by observing the sky using optical telescopes. In the 20th century, technological advances allowed to further increase our knowledge of the Universe by observing the sky in different frequencies of the electromagnetic spectrum other than the visible light. But it was another discovery that opened up a whole new window to the cosmos. In the year 1912, an Austrian physicist named Victor Hess investigated the altitude dependence of ionizing radiation during a number of balloon flights. The ionizing radiation was believed to originate from natural radioactivity of the earth and therefore decreases with altitude. But in contrast, Viktor Hess discovered an increase [2] during his balloon flight. This was later confirmed in a separate experiment. Since the increase was observation time independent, Viktor Hess drew the conclusion that the measured radiation must be of extra terrestrial origin other than the sun. This radiation was called cosmic rays. This gave birth to a new field of research with a lot of interesting questions. Among them, the composition and the sources of these cosmic rays. While the composition, mainly consisting of protons, helium nuclei and electrons, was quickly revealed, the sources especially for the highest energies are still a mystery. A mystery that might be solved with the help of another particle, the neutrino. This particle was discovered as recently as 1956 by the experiment *Poltergeist* [3, 4]. Its properties, electric neutrality and a tiny cross-section, made it hard to detect but also make it the ideal messenger particle as it is not deflected in the interstellar magnetic fields or hardly absorbed by matter. Due to the small cross-section huge detector volumes are needed as realized in the ANTARES or the even larger IceCube detector using water or ice as the detection medium. Neutrino detectors usually make use of the so called Cerenkov light, produced by charged particles moving faster than the speed of light in a given medium, in order to measure neutrino nucleon interactions. While the detection of charged particles, produced in neutrino interactions, with Cerenkov light is a proven and well working detection technique, the short absorption length of blue light in water of $\approx$ 60 m poses a problem when it comes to large detector volumes. It

requires a dense instrumentation and therefore is cost intensive. A new technique, the acoustic detection, might offer the possibility to monitor large volumes with a lot fewer sensors due to the absorption length of sound in water of $\approx 1\,\mathrm{km}$ as opposed to $\approx 60\,\mathrm{m}$ for light. The detection principle is the following: a neutrino particle interaction produces an acoustic pulse which is then measured. When a particle interaction takes place energy is deposited in the medium of the interaction. The deposited energy results in a rise of temperature which in turn creates a measurable pressure fluctuation.
Acoustic particle detection is a new field of research. To investigate the feasibility, 36 acoustic sensors (under-water microphones, so-called hydrophones), part of the so-called AMADEUS system, have been deployed as a part of the ANTARES experiment. The 36 hydrophones are distributed in six local clusters of about one cubic meter each. To unambiguously identify a neutrino source in the end a good directional and source location accuracy is essential. In this work intensive studies of different direction and source location reconstruction techniques are presented and the feasibility of acoustic particle detection is proven. The directional reconstruction, which greatly profits from the use of the local clusters is explained in Sec. 7. In Sec. 8 the position reconstruction of acoustic sources will be explained and the capabilities of the AMADEUS system demonstrated. Finally a signal source density in the vicinity of the detector will be presented.

Chapter 2

Astro-particle Physics

Contents

Astrophysics deals with the physics of the universe. The different disciplines in astrophysics range from mechanics over relativity to particle physics. Particle physics investigates the matter in our universe, the particles that form our universe and their interactions. Astro-particle physics, a relatively young field in physics, utilises messenger particles from outer space to understand certain aspects of our universe like the production and acceleration mechanisms in high energy sources. First measurement of particles from outer space, the cosmic rays, where performed by Viktor Hess [2] in the attempt to show the altitude dependence of ionizing radiation present at the Earth's surface. The discovery of cosmic rays opened a whole now window to the cosmos and also introduced a set of question regarding the origin and acceleration of these particles. V. Hess did not observe cosmic rays directly, but rather their charged secondaries created in interaction in the atmosphere. To understand the acceleration mechanisms of cosmic rays, astro-particle physics makes use of a number of particles travelling through space. Charged particles are the prime candidate but pose one big problem: due to their charge, the particles are deflected in the interstellar magnetic field, thereby loosing all their directional information. Only for highly energetic ($> 10^{19}$ eV) charged particles, the influence of magnetic fields can be neglected and an almost straight line propagation assumed, allowing to observe objects in our universe in a different *light*. Another problem is that charged particles, and also neutral gamma rays, can be absorbed by other stars, planets but mostly by interstellar dust. The only known particles that are not deflected by electromagnetic fields and only weakly absorbed by matter are neutrinos. This makes them the ideal messenger particle, but also very hard to detect.

In the following, the neutrino, a cosmic acceleration method, and candidates for cosmic high energy accelerators will be presented.

2.1 Neutrinos

In the early 20th century the explanation of the beta decay (neutron decay) posed a big problem. The energy of the neutron did not match the energy of the observed particles produced in the decay, in this case the electron and the proton. To solve the energy balance violation, Wolfgang Pauli (1900-1958) postulated the existence of a new light, uncharged particle, the neutrino. The name *neutrino*, Italian for small and neutral, perfectly describes the particle. Small in the sense that it has a tiny cross section and neutral since it has no charge. Both properties are ideal for a messenger particle. As it has no charge, the particle will not be deflected in magnetic fields. The small cross section, a result of it only weakly interacting, makes matter almost transparent to neutrinos, allowing for free propagation from its origin. All these properties make it the perfect messenger particle to study distant or dense sources, but also makes it very hard to detect. It is no real surprise that it took until the year 1956 to verify its existence[3, 4].

The experiment *Poltergeist* for the first time measured neutrinos via the reaction $\bar{\nu} + p \rightarrow e^+ + n$, thereby proving their existence. Given the existence of the neutrino, the beta decay could finally be described by the reaction formula

$$n \rightarrow p^+ + e^- + \bar{\nu}_e.$$

Neutrinos are generated in weak interactions, decays mainly. Today six types of neutrinos are known to exist, the electron-neutrino, the muon-neutrino, the tau-neutrino and their respective antiparticles.

Neutrinos	ν_e	ν_μ	ν_τ
Anti-Neutrinos	$\bar{\nu}_e$	$\bar{\nu}_\mu$	$\bar{\nu}_\tau$

The neutrino-nucleon cross section of a neutrino of 10^{16} eV $\leq E_\nu \leq 10^{21}$ eV is [5]

$$\sigma_{tot}(\nu N) = 7.84 \times 10^{-36}\text{cm}^2 \left(\frac{E_\nu}{1\text{GeV}}\right)^{0.363} \tag{2.1}$$

It is dependent on the neutrino's energy, slowly increasing with energy. In addition, neutrinos are abundant. Practically, a human body is penetrated by about 10^{15} neutrinos in one second. Within one year about 75 of these neutrinos interact with the human body.

2.2 Fermi-acceleration

In order to understand the energy spectrum of cosmic rays, and thus the generation of high energy neutrinos, the acceleration mechanisms present in our universe have to be understood. Since neutrinos can't be accelerated themselves, they have to be created in reactions by particles previously accelerated to high energies. Charged particles can be accelerated in magnetic fields. One acceleration method capable of accelerating particles to high energies is the Fermi-acceleration. Acceleration in this case is achieved by repetitive scattering of charged particles from moving magnetized plasma. First order Fermi-acceleration describes the acceleration of particles by them scattering on plane waves which, for example, occurs in shock fronts of Super Novas Remnants. This acceleration method, although there are others, will be explained in order to illustrate how particles reach these high energies.
A particles change in energy per scattering is $\Delta E = \epsilon E$. After n encounters with the shock wave the particle has an energy of $E_n = E_0(1+\epsilon)^n$, E_0 being the initial energy. Given an escape probability P_{esc}, which is the probability of the particle to escape from the acceleration region, the probability of a particle still being present after n encounters is $(1-P_{esc})^n$. In order to reach an energy E a particle has to scatter

$$n = \frac{\ln(E/E_0)}{\ln(1+\epsilon)} \tag{2.2}$$

times. The portion of particles with an energy greater E is given by

$$N(>E) \sim \sum_{m=n}^{\infty} (1-P_{esc})^m = \frac{(1-P_{esc})^n}{P_{esc}} \tag{2.3}$$

combined the equations yield

$$N(>E) \sim \frac{1}{P_{esc}} \left(\frac{E}{E_0}\right)^{-\gamma} \tag{2.4}$$

with $\gamma = \frac{\ln(1/1-P_{esc})}{\ln(1+\epsilon)} \approx \frac{P_{esc}}{\epsilon} = \frac{1}{\epsilon}\frac{T_{cycle}}{T_{esc}}$, where T_{cycle} is the typical time for the acceleration and T_{esc} the typical time for a particle to remain in the accelerator. Their quotient is the escape probability. So the energy after a time t is

$$E_{max} \leq E_0(1+\epsilon)^{\frac{t}{T_{cycle}}} \tag{2.5}$$

Since T_{cycle} is also a function of the energy the particle spectrum is given by

$$\frac{dN(E)}{dE} \sim E^{-(\gamma+1)}. \tag{2.6}$$

Second order Fermi-acceleration occurs on randomly distributed magnetic mirrors. In order for this acceleration mechanism to work strong magnetic fields and large dimensions are required. Protons, accelerated in such a mechanism, can reach high energies. When escaping the sources, they can react with ambient matter and the photo-field. One possible reaction creating neutrinos is

$$
\begin{aligned}
p + \gamma \rightarrow \Delta^{+}(1232) \rightarrow \quad & \pi^{+} \quad +n \\
\rightarrow \quad & \mu^{+} + \nu_{\mu} \\
& \rightarrow e^{+} + \bar{\nu_{\mu}} + \nu_{e}
\end{aligned}
$$

where the photons may be infra-red photons from the star light or photons from the cosmic microwave background. This reaction results in a cut-off at high energies known as the GZK-cut-off, see Sec. 2.3.4 and produces high energy neutrinos.

2.3 Sources for high-energy cosmic rays

Cosmic rays are composed of electromagnetic waves and a variety of particles. Among these particles are protons, alpha particles (helium nuclei), heavier nuclei, electrons and neutrinos. Possibly originating from a variety of sources, cosmic rays cover a broad range of energies. Figure 2.1 shows the differential flux of the cosmic rays as a function of the energy. The spectrum covers 12 orders of magnitude in energy, and shows a power law decrease of the particle flux with rising energies.

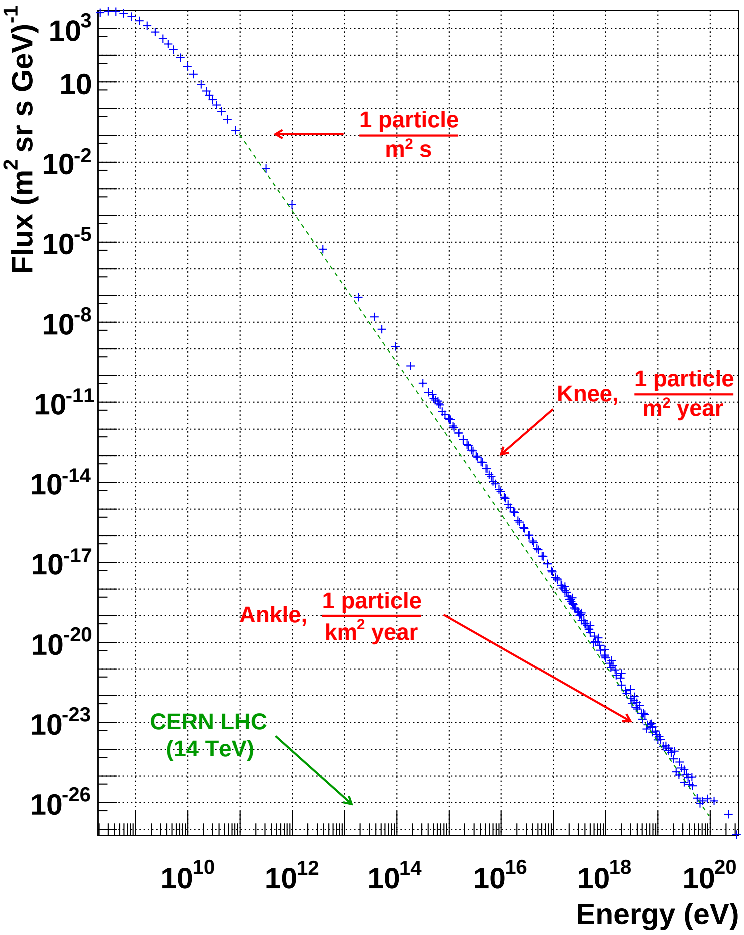

Figure 2.1: Particle flux over particle energy of cosmic rays [6]. The extremely low flux at high energies requires the instrumentation of huge volumes to detect particles.

Some of the potential sources contributing to the cosmic ray spectrum will be introduced in the following.

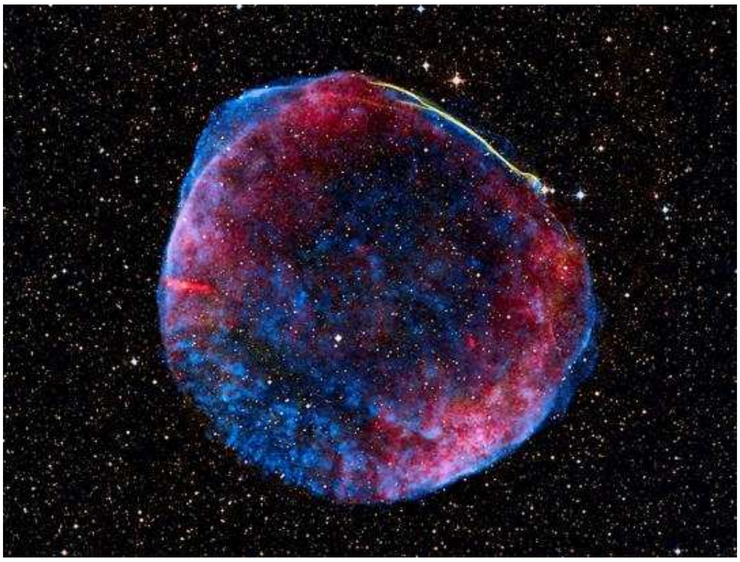

Figure 2.2: A multi wave length image (X-ray (blue); Radio (red); Optical (yellow and orange)) of the Supernova Remnant SN1006. This Supernova was observed in the year 1006 and is considered the brightest Super Nova recorded on Earth.

2.3.1 Supernova Remnants (SNR)

During a supernova, huge quantities of neutrinos are produced, as 99% of the supernova's energy is dissipated in the form of neutrinos. Due to their relatively low energies (MeV scale) they are however not of central interest to high energy astro physics. Neutrinos created in proton-proton or proton-gamma reactions after the acceleration of the nucleons in the shock fronts of the supernova remnant, can have much higher energies. The matter blown out into space serves charged particles as a shock front and can, via the Fermi-mechanism, accelerate protons to energies up to 10^{15} eV. An image of a super nova remnant is displayed in Fig. 2.2.

2.3.2 Active galactic nuclei (AGN)

Active galaxies are typical galaxies with super massive ($M_{BH} \approx 10^8 M_\odot$, $M_\odot$ is the mass of the sun) black holes at their centres. The black hole accretes matter and emits in the radio, infra-red, optical, ultra-violet, X-ray and gamma ray wavebands. Perpendicular to the accretion disk, a collimated jet is formed accelerating particles to energies up to 10^{21} eV via the Fermi-acceleration, see Sec. 2.2. Figure 2.3 shows a schematic drawing of an Active Galactic Nucleus. The AGN's spectrum will vary depending on the observers position relative to the AGN. An observer looking at the accretion disk edge-on will mainly see a strong radio source since the visible light is usually absorbed by the surrounding molecular clouds. Looking straight into the jet one will observe an object of high luminosity and variability, a *blazar*.

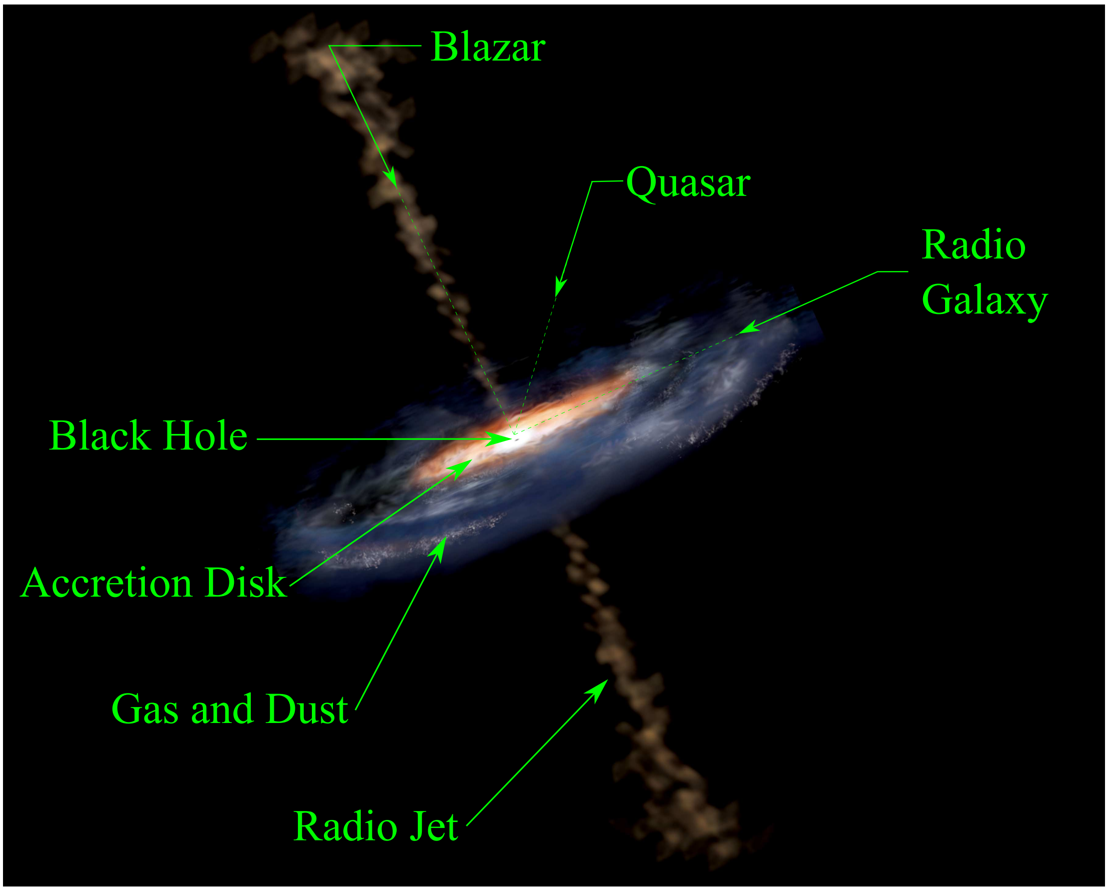

Figure 2.3: An Active Galactic Nucleus (AGN): The characteristics observed depend on the position of the observer relative to the galaxy. Looking into the jet a blazar, at an angle a quasar and onto the disk a radio galaxy is observed. (Picture taken from [7])

2.3.3 Gamma Ray Bursts (GRB)

GRBs were discovered accidentally in the 1960's by the Vela satellite designed to monitor nuclear explosions which might violate a nuclear test ban treaty. Lasting from milliseconds to several minutes these bursts are over a hundred times brighter than typical supernovae and are probably the most extreme form of energy bursts in the Universe. The distribution of GRBs over the sky is isotropic and their spectra have a high red-shift, indicating great distances to their origin. These distances allow an estimation for the energy released in such a burst, which is about 10^{21} greater than the energy emitted by the sun. The created shock fronts are assumed to accelerate electrons and protons which will react to create neutrinos which then propagate through space.

2.3.4 GZK-mechanism

The already shown proton-gamma interaction via the Δ resonance, see Chapter 2.2, is responsible for the so-called "GZK neutrinos". Greisen, Zatsepin and Kuzim (GZK) [8, 9] formulated a threshold for the proton energy required for the production of the $\Delta(1232)$ resonance interacting with the 2.7 Kelvin microwave background. Protons that reach that threshold lose their energy, which limits the protons ranges to a ~ 50 Mpc. The postulated GZK cut-off would lead to a drop in the cosmic ray spectrum at $\approx 10^{19.5}$ eV and result in neutrino energies of the same energy scale. The effect has not yet been unambiguously measured, see Fig. 2.4. The confirmation of the expected GZK-cut-off is of extreme importance to cosmology. If it is not confirmed, there must be unknown sources producing high energy protons close to us. Current data clearly indicate the existence of a cut-off. Either there is a cut-off or cosmic accelerators reach a natural limit resulting in an extreme reduction in the flux.

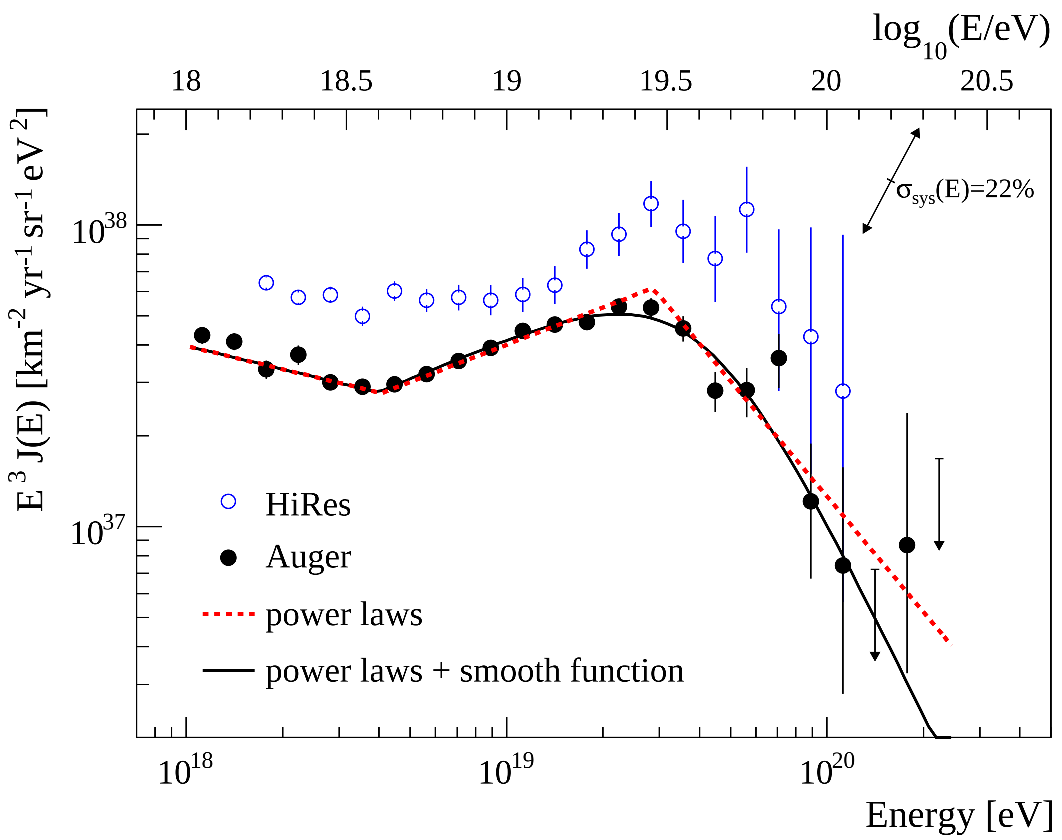

Figure 2.4: The energy spectrum of the Auger Observatory is fitted with two functions and compared to data from the HiRes instrument. The systematic uncertainty of the flux scaled by E^3 is due to the uncertainty of the energy scale (22%). It is indicated by arrows. [10]

Measuring neutrinos produced by the GZK mechanism is of special interest as they could confirm the existence of the GZK-cut-off.

Chapter 3

ANTARES and AMADEUS

Contents

The ANTARES neutrino telescope (Astronomy with a Neutrino Telescope and Abyss environmental RESearch) is a water-Cherenkov detector located in the Mediterranean Sea roughly 30 kilometres south of Toulon, France, at a depth of 2400 meters, see Fig. 3.1. Water- or ice-Cherenkov detectors are designed to mainly measure upward going charged particles. The detector's depth results in a large mass of water on top of the detector which serves as a shield to cosmic ray secondaries coming from above. Neutrinos are the only known particles that can freely propagate through the Earth which is the reason for such a neutrino detector looking downwards. The ANTARES detector consists of 12 vertical structures, so-called strings, measuring 480 meters in height, that are fixed to the sea bed by a dead weight. Each string is kept taut by a large buoy at the upper end of the string. The strings are arranged in form of an octagon on the sea floor and measure about 70 meters between each other comprising a total detector volume of about 0.01km^3 (see Fig. 3.2).

Each string consists of 25 storeys which are instrumented with three photomultipliers (PMs) each. The photomultipliers are oriented around the vertical axis at an angular distance of 120° and are looking downwards by 45° from the horizontal plane.The photomultipliers detect Cherenkov light produced by charged particles travelling faster than the speed of light in water. These particles can be produced by neutrinos interacting with a nucleus creating a secondary particle such as a muon which then travels through the medium. In addition to the detection of Cherenkov light, another method for particle detection is being investigated: Particle cascades can also be detected by acoustic sensors which will be discussed in detail in Chapter 3.1.

The first storey of each line is located 100 m above the sea bed followed by 24 storeys spaced

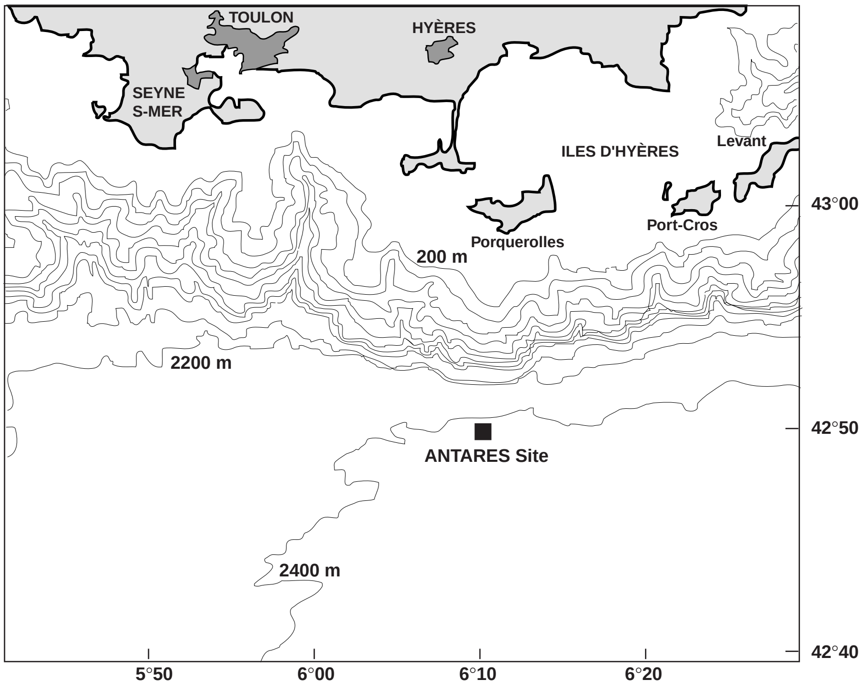

Figure 3.1: Location of the ANTARES detector

evenly with a distance of 14.5 meters. Signals measured by the photomultipliers are digitised at a storey level and sent to shore via the so-called junction box, to which all strings are connected. The junction box is connected to the control and data collecting computers on shore by a 40 km long opto-electrical cable. This cable also provides the power to the detector. In addition to the 12 detector lines a 13th line, the Instrumentation Line (IL07), was deployed to monitor environmental parameters.

The main goals of the ANTARES collaboration are:

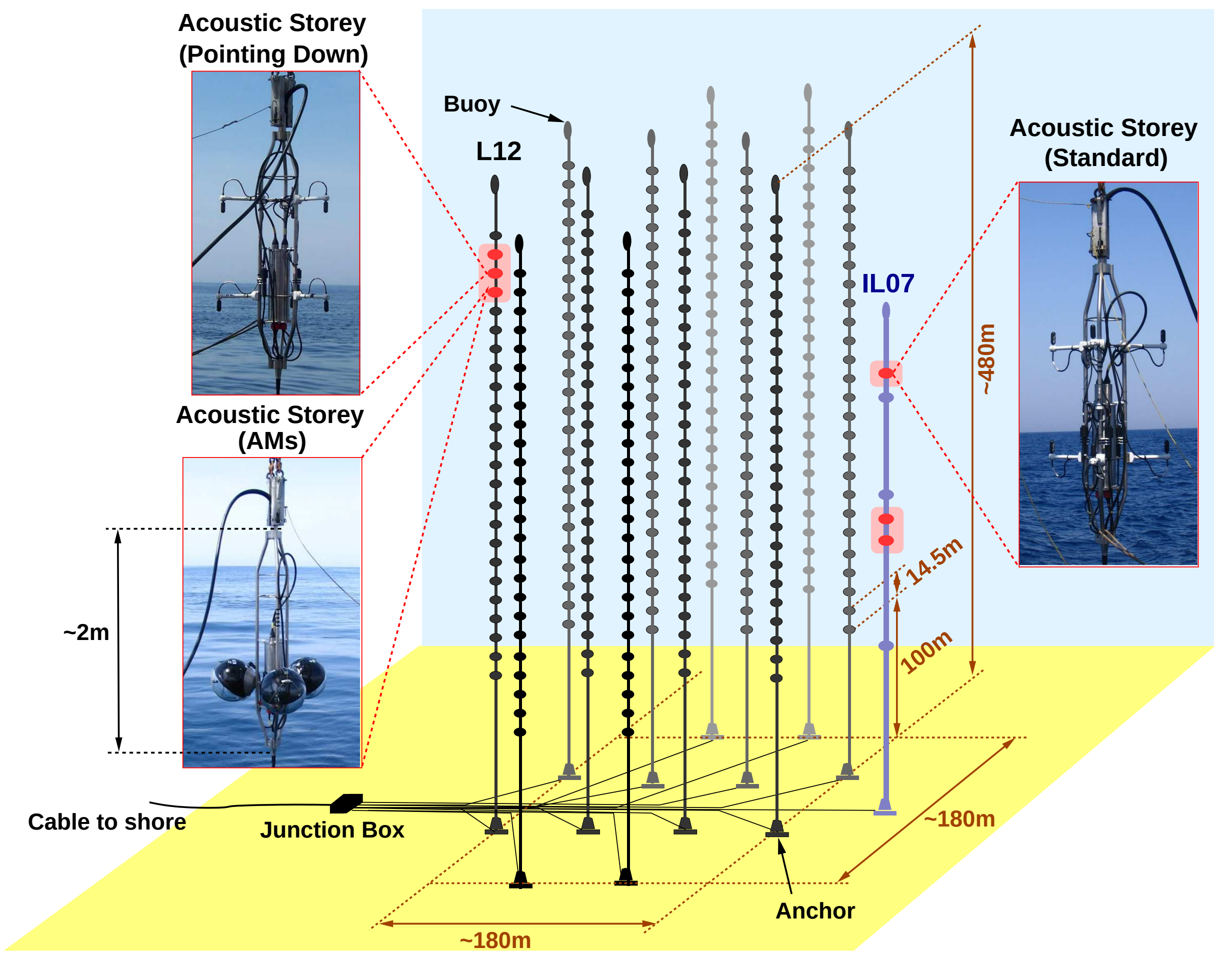

Figure 3.2: The ANTARES detector. Twelve strings support up to 25 storeys of three photomultipliers each. Additionally a 13th line was installed to monitor environmental parameters. The highlighted storeys are *acoustic storeys* each supporting six acoustic sensors. Each line is connected to the junction box which is connected to the shore station by a 40 kilometre long submarine cable.

- Search for point sources of cosmic neutrinos and for diffuse neutrino flux from the universe (in the range of a few 10 GeV to about 1 PeV).

- Measurement of the energy spectrum of atmospheric neutrinos.

- Search for neutrinos from the annihilation of WIMPs (Weakly Interacting Massive Particles e.g. neutralinos) which may be gravitationally trapped in the centre of our galaxy, in the Sun or in the Earth.

3.1 AMADEUS

AMADEUS (ANTARES Modules for Acoustic DEtection Under the Sea) is a subsystem of the ANTARES detector with the goal of investigating the feasibility of acoustic particle detection. Towards this aim six storeys were modified to support acoustic sensors instead of photomultipliers. One such storey consists of six acoustic sensors. These acoustic storeys are located on the Instrumentation Line (IL07) and on the Line 12, see Fig. 3.3. The horizontal spacing between the two lines is about 240 meters. On the IL07 the first storey is located about 180 meters above the sea floor followed by a second storey with a vertical distance of 14.5 meters. The third storey on the IL07 is located about 300 meters above the sea floor. On Line 12 three storeys are equally spaced between 390 and 420 meters above the sea floor. Placing six hydrophones on one storey, thus forming a small local cluster, and applying the mentioned spacing of the clusters allow for noise and transient signal correlation studies with inter sensor spacing ranging from about 1 m to 350 m at a water depth of 2050 to 2300 m. Additionally local clusters offer the advantage of quick direction reconstruction, thereby simplifying source position reconstruction, discussed in the Sec. 7 and 8. AMADEUS was designed to investigate the background of events mimicking particle interactions, to study the deep sea noise and to evaluate signal filtering and source-position reconstruction techniques. It also serves as a test bed for different sensor designs. All design parameterd are essential to evaluate the feasibility of acoustic particle detection in a possible future large-volume detector.

3.1.1 Hardware

One of the construction guide-lines in building the AMADEUS system was to use as much of the ANTARES infrastructure as possible. Nevertheless, some parts had to be replaced by custom-made ones. The optical sensors had to be replaced by acoustic sensors and the data acquisition cards by custom ones meeting the requirements for acoustic particle detection. For the sensors two strategies were followed. One was to use standard hydrophones, commercial and custom-built units developed at the Erlangen Centre for Astroparticle Physics (ECAP). The other strategy was to test so called *acoustic modules*. In the following section the different sensor designs are discussed and the data acquisition is described.

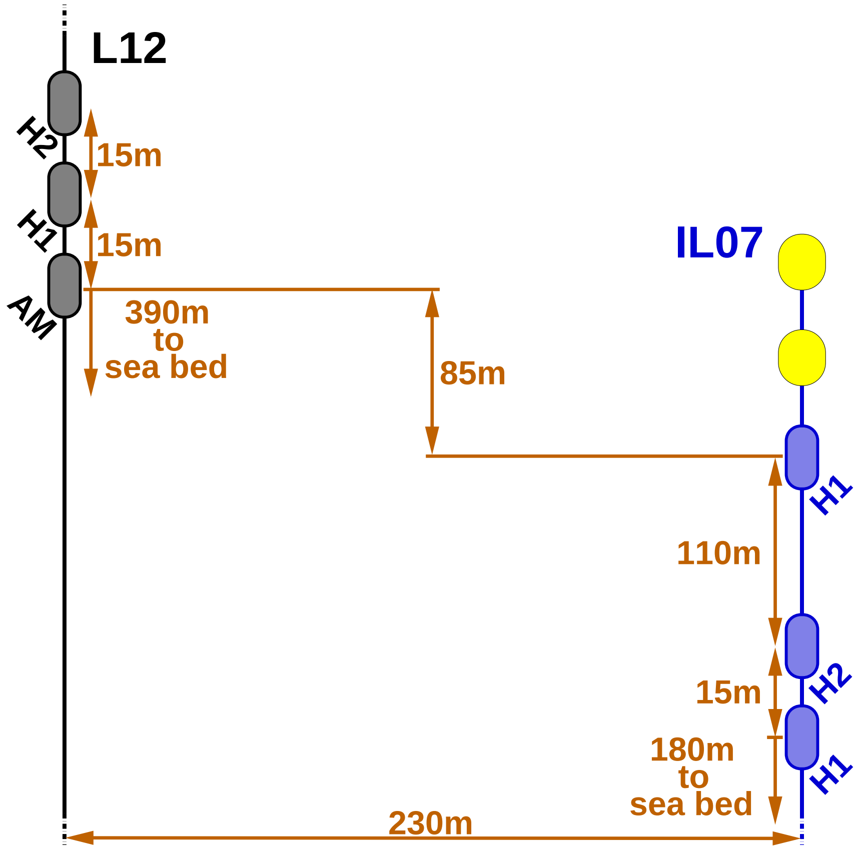

Figure 3.3: Schematic of the AMADEUS setup. Storeys labelled H1 are equipped with commercial hydrophones while the ones labelled H2 use custom-designed hydrophones. The storey labelled AM holds acoustic modules.

3.1.2 Acoustic sensors

The hydrophones used in the AMADEUS project utilise the piezo-electric effect for converting pressure fluctuations into an electric potential, typically in the order of μV/Pa without amplification. They consist of a piezo ceramic with a pre-amplifier (gain $\approx$ 50 dB) in a polyurethane housing protecting the electronics from the harsh environment in the deep sea. Figure 3.4 shows a custom-built hydrophone used in the AMADEUS system [11]. Fixation of the hydrophones is realised by plastic *arms*. These arms, within one horizontal plane, are aligned at an angle of 120° with respect to each other supporting one hydrophone each, see Fig. 3.5. One storey consists of two horizontal planes comprising a local cluster of six hydrophones. The distance between two hydrophone planes is about 0.85 m while the distance between two hydrophones within one plane is about 0.90 m. The sensor supports allow for the sensors to be mounted pointing either upward or downward. For the Instrumentation Line all sensors were installed pointing upward. This was done given the large volume of water above the the hydrophones and the directional sensitivity of the hydrophone. On Line 12 however one storey was configured with sensors pointing down-

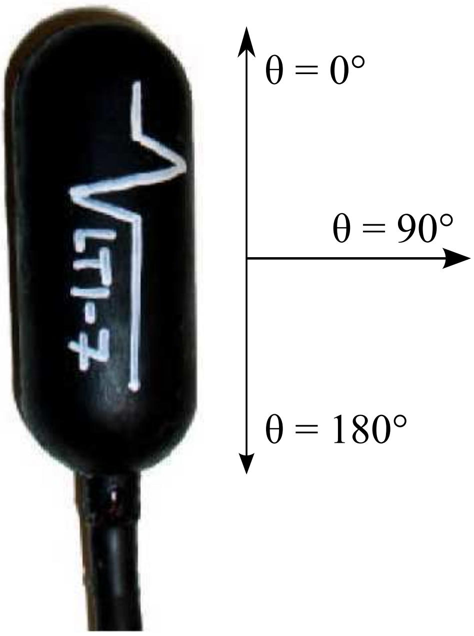

Figure 3.4: A custom built hydrophone developed at the Erlangen Centre for Astroparticle physics. The sensor element, a piezo ceramic, and a pre-amplifier, tuned for the frequencies relevant for acoustic particle detection, are coated in a polyurethane housing.

wards allowing for comparison between the two configurations and for drawing conclusions on the ambient noise directivity.

Figure 3.5: Support of the hydrophones. Six such supports are mounted on each acoustic storey.

The second approach in sensor design taken was the development of acoustic modules. The sensors, like hydrophones, consist of a piezo ceramic and a pre-amplifier, but instead of placing them in a polyurethane housing they were glued to the inside of a glass sphere. The glass sphere is of the same type as used for the photomultiplier housing in the ANTARES project, protecting the sensors from the high pressure. Ideas behind this approach are to investigate the possibility of creating a dual sensor module consisting of a photomultiplier and an acoustic sensor accommodated in the same housing and protecting them from the high pressure. A picture of such an acoustic module can be seen in Fig. 3.6. It comprises two acoustic sensors within one glass sphere. The storey equipped with acoustic modules consists of three such spheres attached to a

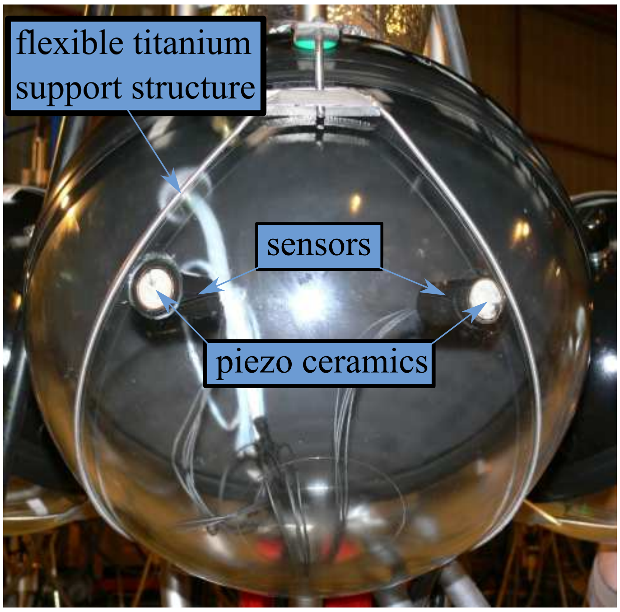

Figure 3.6: Picture of an acoustic module, three of such AMs are mounted on one storey.

standard ANTARES storey frame.
The frequency range of all acoustic sensors (1 to 50 kHz) is matched to the one relevant for acoustic particle detection, see Fig. 4.1. The average sensitivity ranges from 140 to 145 dB re 1 V/μPa (0.05 to 0.1 V/Pa) at an inherent noise level of 105 to 120 dB re 1V/$\sqrt{\text{Hz}}$ (1 to 5 μV^2/Hz).
Detailed studies regarding the sensitivity as a function of frequency and its angular dependence were conducted. The results are shown in Fig. 3.7. Features below 10 kHz are caused by the experimental set-up. The commercial hydrophone has a relatively flat sensitivity curve for the relevant frequencies while the custom-designed version shows some more pronounced features. Clearly visible for both sensors are their global maximums, at 31 kHz for the custom-designed and 45 kHz for the commercial hydrophone, indicating the resonance frequency of the respective piezo element. The directional sensitivity for a commercial sensor is shown in Fig. 3.8. In the horizontal plane, defined by $\theta = 90^\circ$, the sensor shows very little variation, i.e. it has a uniform sensitivity in all directions. In the vertical plane (θ) however, the sensor shows some more pronounced features for frequencies greater 60 kHz where the overall sensitivity drops for angles $< 60^\circ$ or $> 100^\circ$. For frequencies above 60 kHz it is most sensitive to horizontal directions. Signals from directions with angular values exceeding 165° are essentially shielded by the

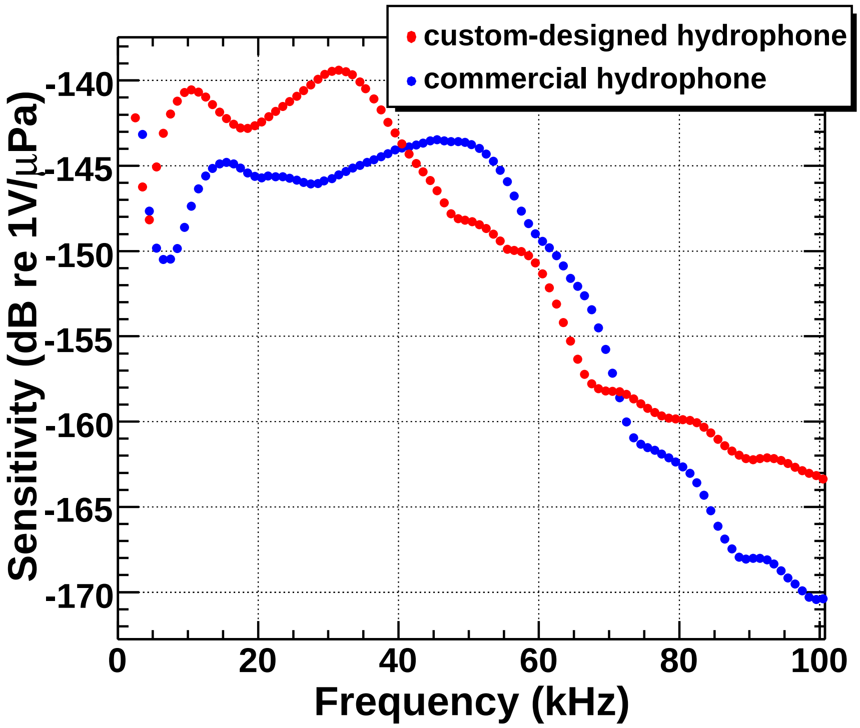

Figure 3.7: Mean sensitivity of a custom hydrophone (red) and a commercial hydrophone (blue)[11]. The resonant frequencies of the piezo element manifests itself by a local maximum at 31 kHz for the custom hydrophones and 45 kHz for the commercial hydrophones.

electronics and the cable attached.

The directional sensitivity changes the signal shape dependent on the angle of incidence. Furthermore, for each direction the signal is distorted due to the signal transfer function of the sensors. This has to be taken into account in order to accurately identify an acoustic signal. Figure 3.9 shows the response of a hydrophone to a bipolar signal. Both the expected and the measured signal are shown indicating the good understanding of the sensor element.

3.1.3 Signal digitisation

The signal generation principle of the acoustic sensors as well as the necessary sampling time and resolution greatly differ from that of photomulitpliers. Hence the ANTARES digitisation boards inside the storeys were substituted by the so-called AcouADC boards (see Fig. 3.10) especially designed for the needs of acoustic particle detection.

The analogue part of the AcouADC board filters the sensor signal with a band-pass filter matched to the desired frequency range of about 1 kHz to about 100 kHz and amplifies it. The amplification is done in two stages, the first one has three settings, 1.00, 10.0 and 100 while the seconds stage offers four settings, 1.00, 1.78, 3.16 and 5.62, allowing for a total range of 1 to 562. The maximum sampling rate of the AcouADC is 500 kSamples/s with the possibility

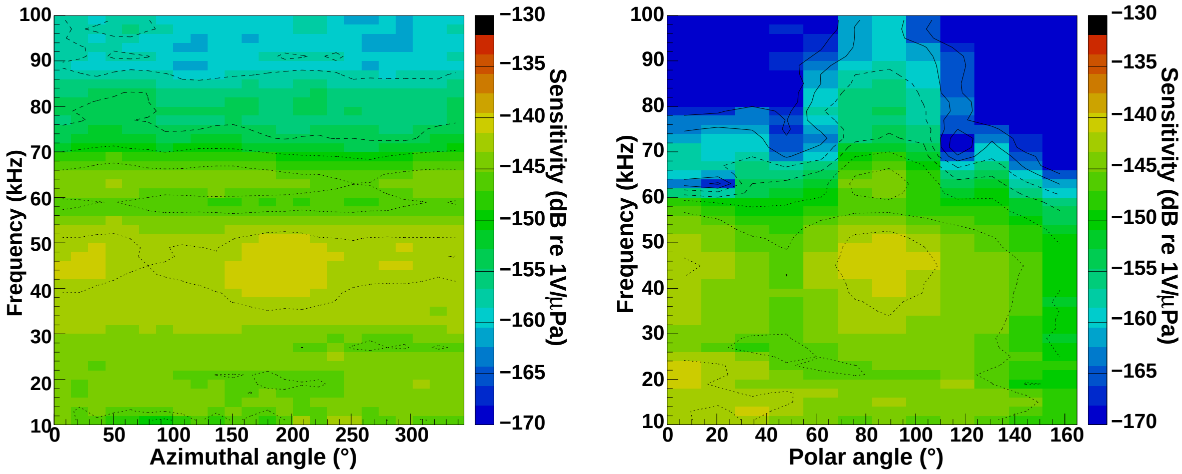

Figure 3.8: Directional sensitivity of a commercial hydrophone used in the AMADEUS system, on the left for the azimuthal (ϕ) and on the right for the polar (θ) direction. While the sensor can be regarded uniformly sensitive in the azimuth, deviation can be observed for vertical angles. For angles greater than 165° to the polar axis the sensor is shielded by the electronics and the attached cable.

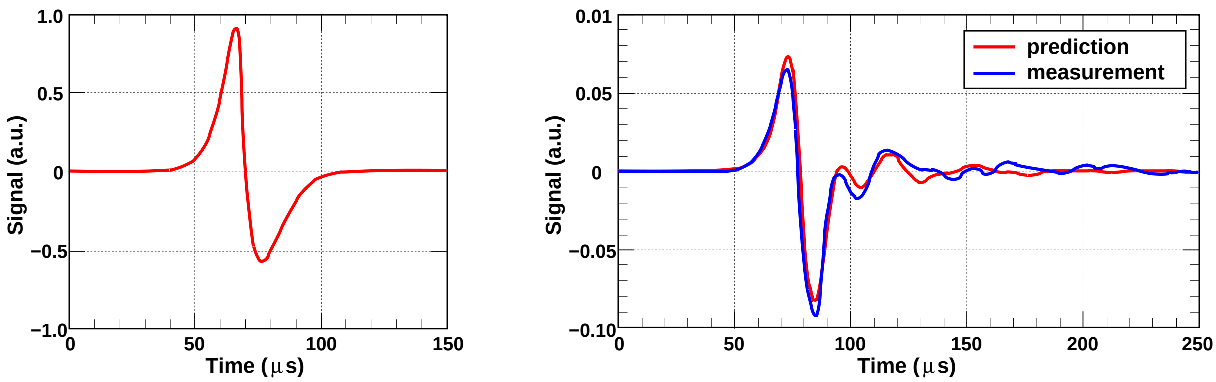

Figure 3.9: Response of a hydrophone (right) to a bipolar signal produced by a transducer (left). The recorded signal quite well matches the expected signal. Both, the sensitivity of the hydrophone and the characteristics of the transducer were taken into account.[11]

to digitally down-sample to 250 kSps and 125 kSps. The digital part of the AcouADC mainly consists of a Field Programmable Gate Array (FPGA) and a micro-controller. It handles the data of the sensors, transforms the data into the ANTARES data format and communicates with the data acquisition on shore. It is programmable from the shore and receives the operation settings used for both the digital and analogue part. The FPGA is synchronised by a 20MHz clock giving

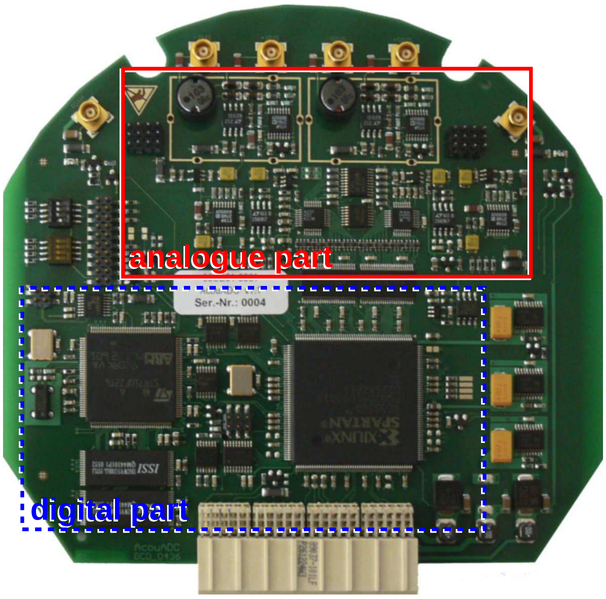

Figure 3.10: AMADEUS data acquisition hardware. The card consists of an analogue and a digital part. The analogue part of the final design is shielded to minimise interference with other electronics.

a synchronous start time of the acoustic storeys with an absolute uncertainty of 100 ns.

3.1.4 Detector operation

AMADEUS uses its own operation control program which is running on a server dedicated to acoustic particle detection only. Using separate hard- and software ensures no interference between the AMADEUS system and ANTARES. In addition three server-type computers for data filtering and storage of acoustic data were installed, for more details see [12]. Standard detector operation settings are a gain factor of 10.0 and a sampling rate of 250 kSamples/s. The gain factor of 10.0 is motivated by the ambient noise at the sensor sensitivity. The down-sampling by a factor of two is due to the maximum transfer rate of each storey and the sensitivity of the sensors. Data rates for the complete AMADEUS system (36 sensors) are about 140 Mbps.

Chapter 4

Acoustic signals signals and background

Contents

4.1 Particle induced acoustic signals

In 1957, G.A. Askarian first discussed the thermo-acoustic model setting the base for acoustic particle detection [13, 14]. The thermo-acoustic model describes the creation of sound waves induced by a local energy deposition, e.g. from a particle cascade, in a medium. The energy deposition heats the medium locally resulting in a pressure change and thus a sound wave. Test measurements using proton and laser beams have been performed, verifying the theory [15, 16]. For neutrino astrophysics this presents a possible method for detecting ultra-high energy neutrinos. Since the absorption length of sound in water (1 km @ 10 kHz) is significantly larger than the attenuation length of light (60 m for blue light), much larger volumes can be instrumented with the same amount of sensors for the same costs compared to current Cherenkov detectors. Acoustic neutrino detection can't however be regarded as a possible replacement of Cherenkov detectors but rather as a supplement, which will be discussed later.

4.2 Signal generation

When a neutrino passes through a medium it can interact either via neutral or charged current reactions, generating a cascade composed of a hadronic and/or an electromagnetic part. The particles in the cascade deposit energy along their tracks and locally heat up the medium, water in case of ANTARES/AMADEUS. The change in temperature of the water causes the water to expand, at a water temperature of greater than four degrees Celsius. The expansion of the water, which is fast with respect to hydrodynamic time scales of a μs, results in a pressure change which creates an acoustic signal. The time scale of the energy deposition is in a time frame of $t_K = \frac{L}{c}$, where L is the length of the particle track and c the velocity of light ($v_{particle} \approx c$). Since the time scales of energy dissipation is much larger the energy deposition can be regarded as instantaneous. The signal process is theoretically explained by the thermo-acoustic model mentioned above. It explains the creation of sound signals due to a sudden expansion of the heated water in the region where the cascade deposits its energy. The time and space signature of the pressure signal (acoustic signal) $P(\vec{r}, t)$ is given by an inhomogeneous wave equation. The inhomogeneity is due to the energy distribution $q(\vec{r}, t)$ of the cascade. [14]

$$\Delta P - \frac{1}{c_s^2}\frac{\partial^2 P}{\partial t^2} = -\frac{\alpha}{C_p}\frac{\partial^2 q(\vec{r}, t)}{\partial t^2} \tag{4.1}$$

α is the heat expansion coefficient, C_p the specific heat capacity of the water and c_s the speed of sound. The solution of the equation is the Kirchhoff-Integral,

$$P(r, t) = \frac{\alpha}{4\pi C_p}\int \frac{dV'}{\left|\vec{r} - \vec{r'}\right|}\frac{\partial^2}{\partial t^2} q\left(\vec{r'}, t - \frac{\left|\vec{r} - \vec{r'}\right|}{c_s}\right) \tag{4.2}$$

which is integrated over the entire volume. The energy deposition is assumed to be instantaneous, therefore

$$\frac{\partial}{\partial t} q(\vec{r}, t) = q(\vec{r})\delta(t) \tag{4.3}$$

With this assumption one obtains:

$$P(\vec{r}, t) = \frac{\alpha}{4\pi C_p} c_s^2 \frac{\partial}{\partial R}\int_{S_{\vec{r}}^R} d\sigma \frac{q(\vec{r'})}{R} \tag{4.4}$$

The integration over the surface of a sphere $S_{\vec{r}}^R$ with the radius $R = c_s t$, the observer is at the midpoint $\vec{r}$ of the sphere.
The signal depends on the shape and size of the energy deposition and the properties of the water like the medium properties of the water, the heat expansion coefficient α, the specific heat capacity C_p and the velocity of sound c_s. The properties of the medium are sometimes combined in the 'Grüneisen-Parameter' parameter

$$\gamma = \frac{\alpha c_s^2}{C_p} \tag{4.5}$$

The factor α is strongly temperature dependent. At 4° C it is equal to zero and therefore no acoustic signal will be generated at this critical temperature. This was confirmed in laser beam

measurements [17].
The acoustic signal is of bipolar shape and its amplitude is $A \approx 10\,\mathrm{mPa}\,\frac{E_{casc}}{1EeV}$ @ 200 m distance. The length of the signal (peak-to-peak) is about 15 μs and its peak frequency about 11 kHz @ 1000m. An example of a simulated signal is shown in Fig. 4.1.

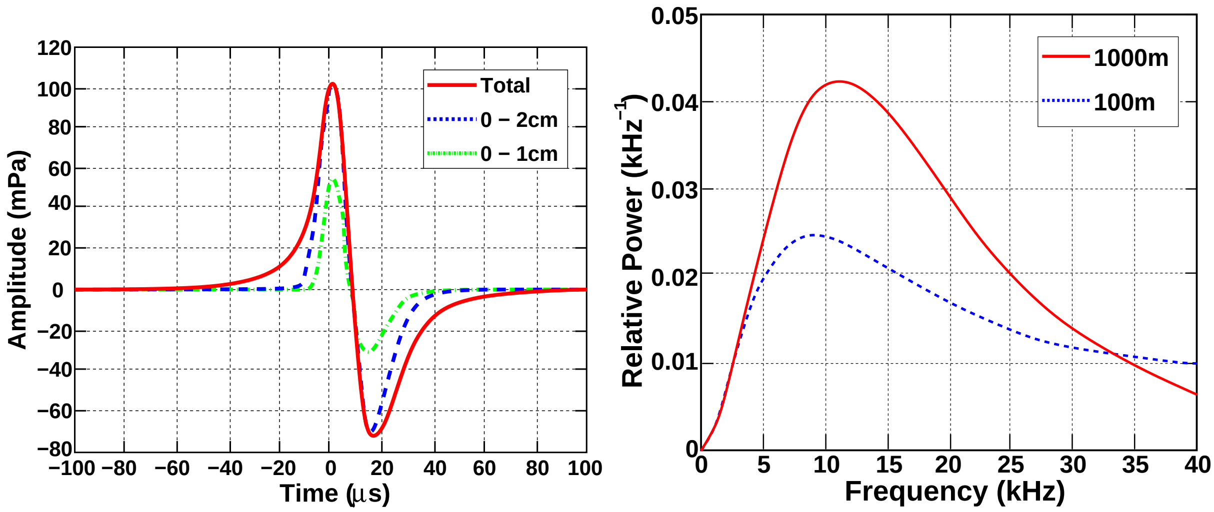

Figure 4.1: Left: Simulated bipolar pressure pulse created by a 10^{20} eV hadronic cascade at a radial distance of 1 km. Roughly half of the pressure pulse is produced within a lateral radius of 1 cm (dash-pointed line) of the cascade, whereas the energy distribution within a radius of 2 cm (dashed line) is nearly completely responsible for the final signal shape (solid line). Figure adapted from [18]. Right: The power spectral density of the signal.

4.3 Signal propagation

In this section the propagation of the acoustic signal produced by a neutrino-induced cascade is discussed. As shown above, the shape and the propagation geometry of an acoustic signal greatly depend on the energy deposition density $q(\vec{r}, t)$. In the case of a neutrino-induced cascade the typical dimensions are tens of meters in their longitudinal and a few centimetres in their lateral direction [19]. Therefore the pressure pulse propagates as a ring perpendicular to the axis of the cascade, the thickness of the ring is specified by the length of the cascade and is rotationally symmetric to the cascade long axis, see Fig. 4.2.

The sound front is getting wider as it propagates through the water. The disk shaped expansion, assuming a sufficiently instrumented detector, allows to reconstruct the direction of the cascade, using the orientation of the disk, and thus the directional information of the primary particle. The signal amplitude profile inside the disk is shown in Fig. 4.3. A significant dependence on the position along the axis of the cascade can be seen.

Due to the cylindrical emission geometry, the signal amplitude is proportional to $1/\sqrt{r}$ in the near field and it is proportional to $1/r$ in the far field, where r is the lateral distance from the

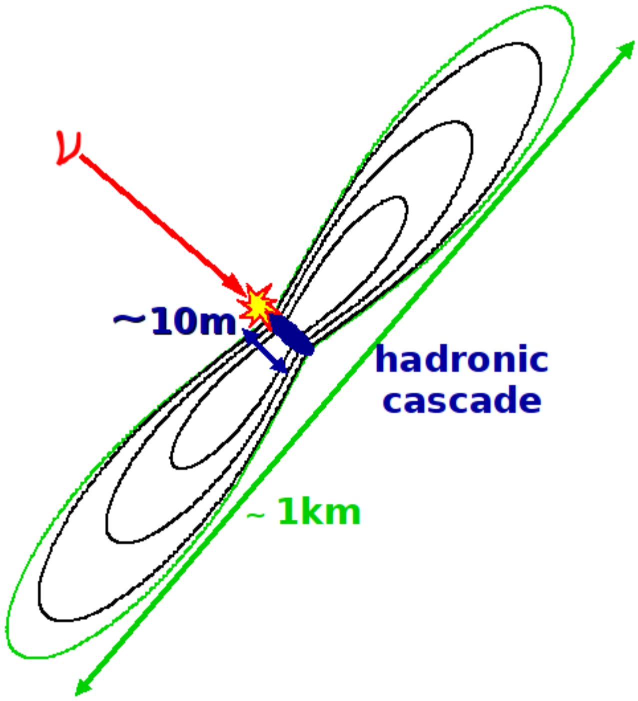

Figure 4.2: Visualisation of a neutrino induced sound wave. The neutrino induced cascade deposits its energy in a narrow region of about 10 m length and a few cm width. This energy deposition geometry results in a pancake like propagation geometry.

source. The transition from near field to far field is at a distance in the order of 100 m. Figure 4.3 shows the amplitude as a function of the distance from the centre of the cascade. It also accounts for the attenuation length of sound in water which is large compared to light ($\approx$ 60 m). The attenuation length ranges from 70 km at 1 kHz to 100 m at 100 kHz. For the maximum relative signal power around 11 kHz the attenuation length is about 3 km.
The sound velocity depends on several factors like the density of the medium. Thus a sound velocity profile evolves in a medium. This can cause refraction of the signal. For the AMADEUS detector the sound velocity changes due to the change in pressure and the density which is a function of the depth.

4.3.1 Velocity of sound in water

The propagation of sound rays primarily depends on the density of the medium. In case of AMADEUS the medium is salt-water, therefore the density ρ_w depends on the salinity S, the temperature T and the pressure P. This, as already mentioned in the previous chapter, results in a velocity profile. Figure 4.4 shows the velocity of sound and the temperature, each as a function of depth at the location of the AMADEUS system. Both plots show a decrease for the first 100 m. At greater depths the temperature is more or less constant while the sound velocity

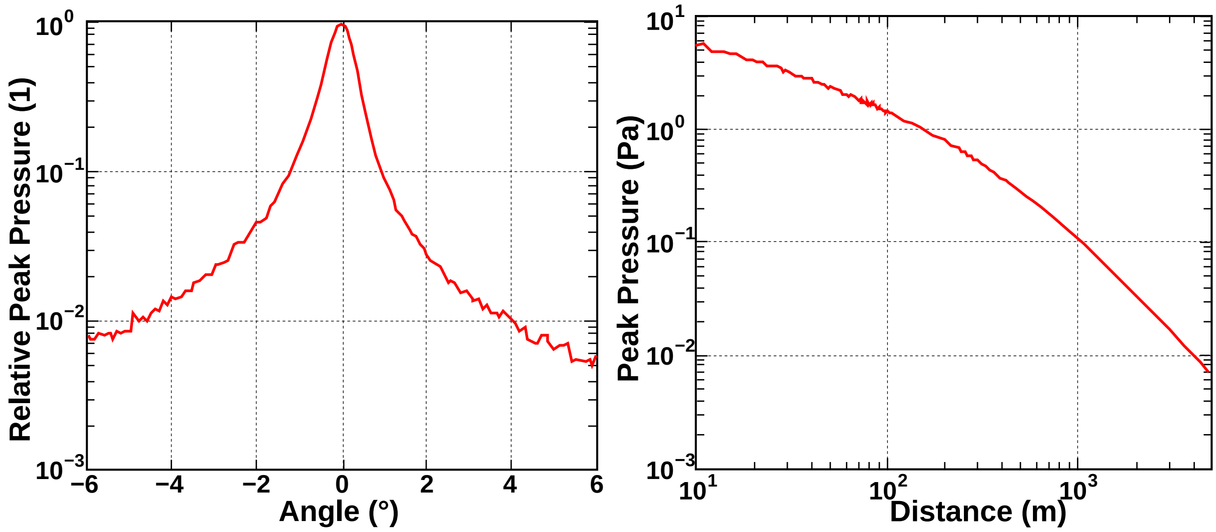

Figure 4.3: Left: Simulated signal directionality for a 10^{20} eV shower at 1 km distance from the origin, normalised to the peak pressure at 0° (perpendicular to the shower axis). Right: Peak pressure as a function of the distance from a cascade with the same energy.

increases linearly. The measured data are consistent with the calculated values resulting from the evaluation of the *UNESCO* algorithm [20].

A good approximation for the increase in velocity is 5 m/s for each degree in temperature and 0.02 m/s for a depth change of one meter. This change in the velocity of sound has to be taken into account when reconstructing source locations at a distance of more than 1 km since the refraction then starts to significantly alter the angle of incidence on a sensor. Refraction effects will be discussed in more detail in the following.

4.3.2 Refraction

Changes in the velocity of sound cause acoustic signals to be refracted along their path. To get an idea of the magnitude of the direction change, the difference between straight line propagation and the actual signal propagation was evaluated. In order to simplify the calculations the following assumptions were made: The water is horizontally translation invariant, the sound waves propagate planar in a coordinate system with the z-axis pointing vertically upward and the x-axis pointing horizontally; sound propagation is in the (x, z)-plane, a third dimension is not needed given the horizontal translation invariance. The velocity of sound is $c(z) = c_0 - kz$, where $c_0 = 1.546 \times 10^3$ m/s and the sound velocity gradient $k = 0.01654/$ s, typical values for the ANTARES site.

Two sound rays with a vertical distance Δz will experience two different sound velocities given by the sound velocity gradient k. This results in a slight difference in path length δs for a travel time t of the two sound rays. This change in path length causes the common wave front of the sound rays to be refracted upwards, see Fig. 4.5.

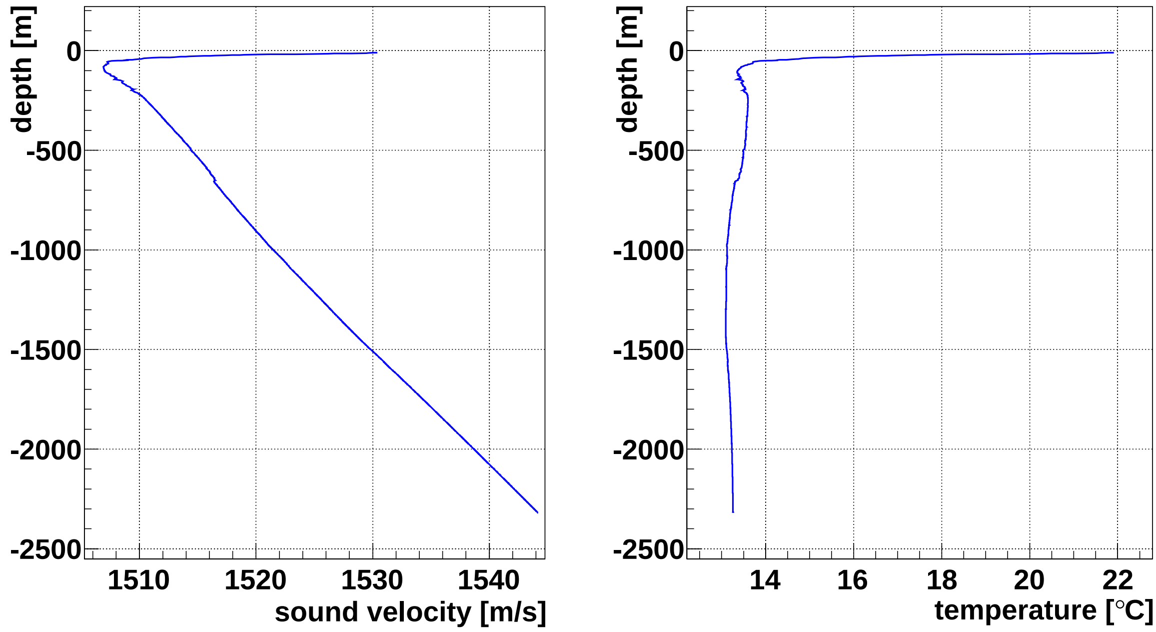

Figure 4.4: Left: The sound velocity as a function of the depth measured at the site of the ANTARES detector. Right: The temperature profile at the ANTARES site. The impact of the temperature on the sound velocity can clearly be seen. Below 100 m the temperature is about constant resulting in a steady increase of the sound velocity with the depth.

Their path lengths during this time interval differ by

$$\delta s = t\,[c(z) - c(z+\Delta z)] = t \cdot k\Delta z\ . \tag{4.6}$$

With $\delta x = c(z)t \cdot \cos\alpha$ (see Fig. 4.5) this gives

$$\delta s = \frac{\delta x \cdot k\Delta z}{c(z)\cos\alpha}\ . \tag{4.7}$$

From the geometry of the triangle ABC we obtain:

$$\delta s = \overline{\mathrm{AC}} \cdot \tan(\delta\alpha) = \frac{\Delta z}{\cos\alpha} \cdot \delta\alpha\ . \tag{4.8}$$

The comparison of equations the (4.7) and (4.8) results in

$$\frac{\delta\alpha}{\delta x} = \frac{k}{c(z)}\ . \tag{4.9}$$

In order to eliminate $\delta\alpha$ and δx, we use $\mathrm{d}z/\mathrm{d}x = \tan\alpha$:

$$\frac{\mathrm{d}^2 z}{\mathrm{d}x^2} = \frac{\mathrm{d}\tan\alpha}{\mathrm{d}\alpha} \cdot \frac{\mathrm{d}\alpha}{\mathrm{d}x} = \left(1 + \tan^2\alpha\right)\frac{\mathrm{d}\alpha}{\mathrm{d}x}\ . \tag{4.10}$$

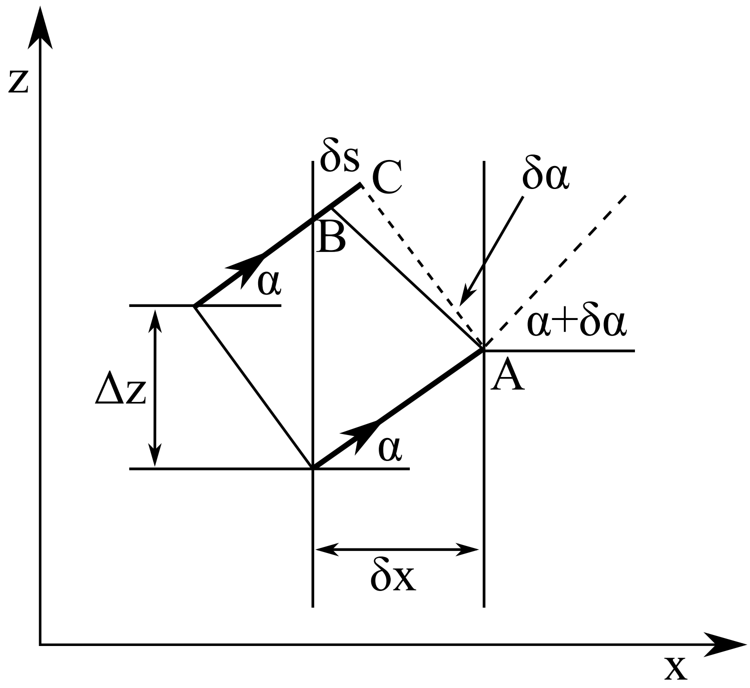

Figure 4.5: Two parallel sound rays, with a vertical distance of Δz, propagating through an infinitesimal volume of water. The z dependence of the sound velocity tilts the wave front by an angle $\delta\alpha$

With $\delta\alpha \equiv \mathrm{d}\alpha$ and $\delta x \equiv \mathrm{d}x$ this gives: results in

$$\frac{\mathrm{d}^2 z}{\mathrm{d}x^2} = \left[1 + \left(\frac{\mathrm{d}z}{\mathrm{d}x}\right)^2\right] \cdot \frac{k}{c(z)} \tag{4.11}$$

or, in simplified notation

$$z'' = k \cdot \frac{1 + (z')^2}{c_0 - kz} \ . \tag{4.12}$$

For short distances, i.e. in the order of one kilometer, the term in the denominator of equation (4.12) can be approximated by $c_0 - kz \approx c_0$ without much loss of accuracy ($< 1\%$). The resulting differential equation is

$$z'' = \frac{k}{c_0}\left(1 + (z')^2\right) \ , \tag{4.13}$$

which can be solved analytically by the ansatz

$$z'(x) = \tan\left(\frac{k}{c_0}(x - \xi)\right) \ , \tag{4.14}$$

with ξ being an integration constant. Analytic integration yields

$$z(x) = -\frac{c_0}{k} \cdot \ln\left[\cos\left(\frac{k}{c_0}(x - \xi)\right)\right] + \zeta \tag{4.15}$$

with a further integration constant ζ.

The integration constants need to be determined from the initial/boundary conditions. For this work $z_0 = z(x_0)$ and $z'_0 = z'(x_0)$ were chosen. This corresponds to the emission of the signal with known direction and origin. Without loss of generality we can set $x_0 = 0$; ξ and ζ are then given by

$$z'_0 = -\tan\frac{k\xi}{c_0} \quad \Rightarrow \quad \xi = -\frac{c_0}{k}\arctan(z'_0) \tag{4.16}$$

and, since $\cos x = 1/\sqrt{1+\tan^2 x}$,

$$\begin{aligned} z_0 &= z(0) = -\frac{c_0}{k}\ln\left[\cos\left(\arctan(z'_0)\right)\right] + \zeta = \frac{c_0}{2k}\ln\left(1+(z'_0)^2\right) + \zeta \\ \Rightarrow \quad \zeta &= z_0 - \frac{c_0}{2k}\ln\left(1+(z'_0)^2\right) \ . \end{aligned} \tag{4.17}$$

With these results, $z(x)$ can be written as

$$z(x) = z_0 - \frac{c_0}{k}\ln\left[\sqrt{1+(z'_0)^2}\cos\left(\frac{kx}{c_0} + \arctan(z'_0)\right)\right] \ ; \tag{4.18}$$

using the relations $\cos(x+y) = \cos x \cos y - \sin x \sin y$ and $\sin x = \tan x/\sqrt{1+\tan^2 x}$, Equation (4.18) can finally be simplified to

$$z(x) = z_0 - \frac{c_0}{k}\ln\left[\cos\left(\frac{kx}{c_0}\right) - z'_0\sin\left(\frac{kx}{c_0}\right)\right] \ . \tag{4.19}$$

The results of Eq. 4.19 for the propagation of sound rays are given in Fig. 4.6 and 4.7.

In this work the sound sources studied are in close proximity of the detector. Following the results explained in this Section, refraction for such sources can be neglected.

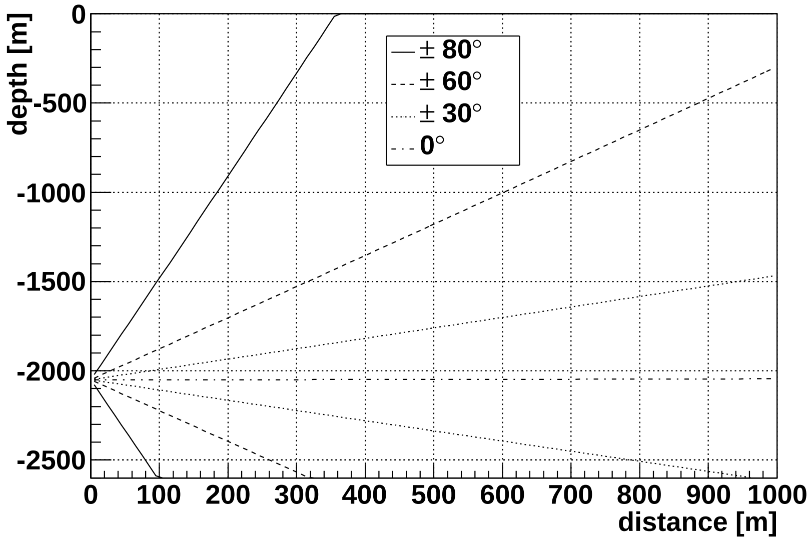

Figure 4.6: Propagation of sound rays emitted at different angles from a position of $z = -2050\,\mathrm{m}$. Their propagation takes refraction into account. The propagation appears almost linear, for differences to straight line propagation see Fig. 4.7. Temperature effects of the top 100 m were ignored.

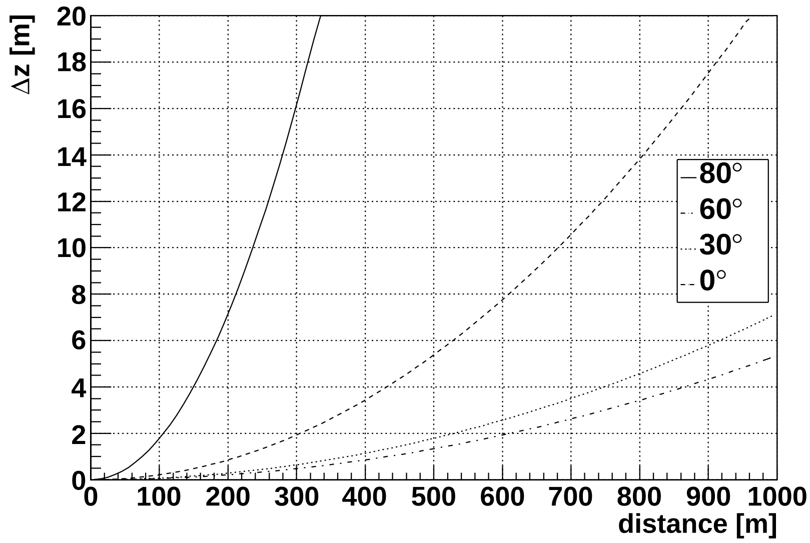

Figure 4.7: Difference (Δz) between linear propagation and a refracted sound wave. As expected, the effect is relatively large for sound waves experiencing a great change in sound velocity.

4.4 Acoustic background in the deep sea

Acoustic particle detection in the deep sea is challenging especially due to the wide range of background sources. Among them are:

- Seismic activities
- Pressure changes due to current induced turbulences
- Ships
- Wind, rain, waves and spray
- Biological sources (e.g. whales, dolphins)
- Thermal noise (due to molecular movement of the water)

These background sources can be grouped into two different types. One consists of transient background signals. These signals, created by ships and biological sources, for example, contribute to the overall noise but are not present all the time. Noise created by the wave movement and thermal noise, so called persistent or ambient noise, is not correlated with activities around the detector except for the weather which fluctuates on much larger times scales than the presence of dolphins for example. Of great interest is the spectral distribution of the background with respect to the one of the signal. One of the dominating background sources is the noise induced by wind. Figure 4.8 shows the noise spectrum in the deep sea for different wind speeds.

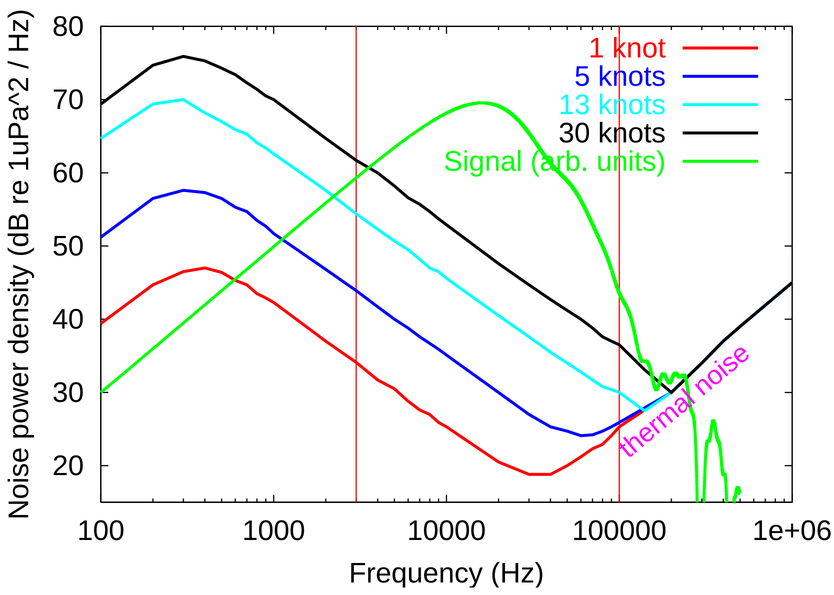

Figure 4.8: Noise spectra for different wind speeds and the expected spectrum of the signal, the signal nicely fits into the minimum of the noise [21].

The frequency band from 1 kHz to 100 kHz is largely dominated by the wave movement (the sea state), the spectrum decreases for higher frequencies. Thermal noise —increasing with frequency— dominates the noise spectrum above 100 kHz. The expected signal lies in the minimum of the noise spectrum, see Fig. 4.8. This coincidence is helpful for the challenging task of acoustic neutrino detection.
As shown above, there are several possible background sources. To investigate the feasibility of an acoustic particle detector the evaluation of the background at a potential site is essential. This encompasses long term studies of the background on long and short time scales. Short time fluctuations of the background originate from transient sources like ship traffic and sea mammals. These signals can render the detector essentially mute during the time of the occurrence. M. Neff is investigating the rate of neutrino like signals and has observed a dependence of the rate as a function of the day time, see Fig. 4.9. Neutrino-like signals in this case mean that a detected signal has a bipolar content which unfortunately holds for many detected signals.

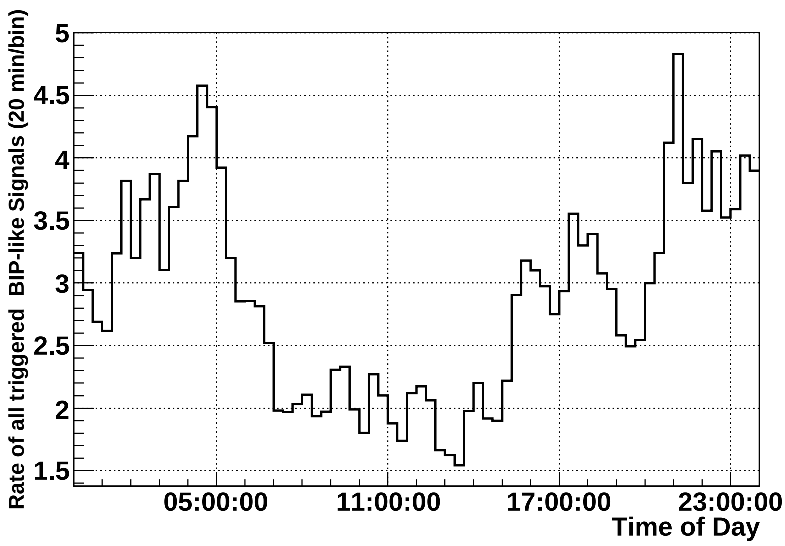

Figure 4.9: Mean distribution of signals with bipolar content of the time of day for time period of two months.

Also of great interest is the persistent background, the ambient noise. As mentioned above the background largely varies with the sea state. This variation could be verified at the site of the ANTARES detector, see Fig. 4.10. The background is highly dependent on the current sea state which in turn is a result of the strength of the wind. The correlation coefficient between the weather and the observed ambient noise is about 80%. Fortunately weather conditions are favourable for neutrino detection most of the time as can be seen in the colour coding of Fig. 4.11. It indicates low wind speeds most of the time thus leading to low background noise in the detector. The mean noise level is about 10 mPa which leads to a signal energy threshold of about 10^{18} eV

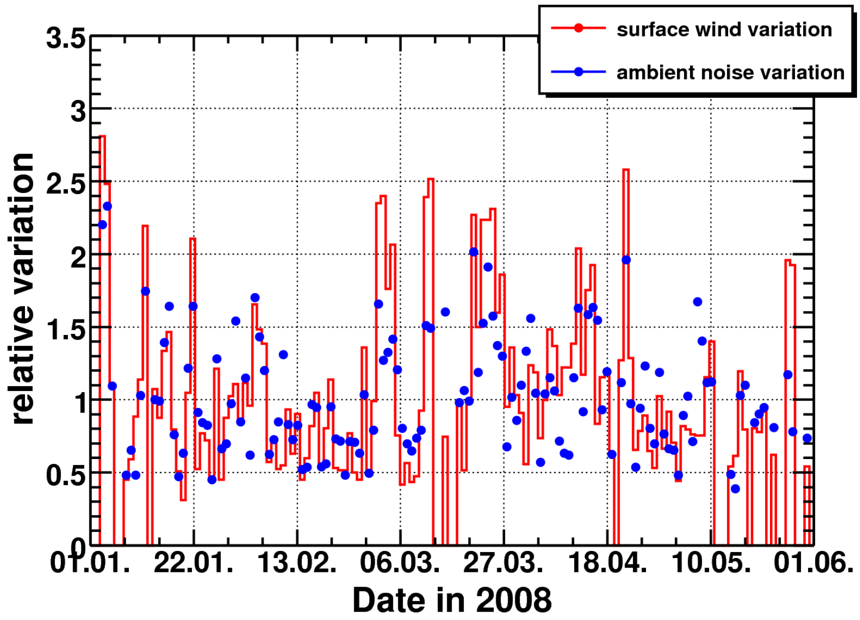

Figure 4.10: The ambient noise level at the ANTARES site and the wind speed measured at a weather station at Cap Cepet (30 km north-west of the ANTARES site) in the first half of the year 2008. A correlation between the two variables can be seen. The agitation of the sea surface is the main source of noise in the scanned frequency range ($1 - 50$ kHz).

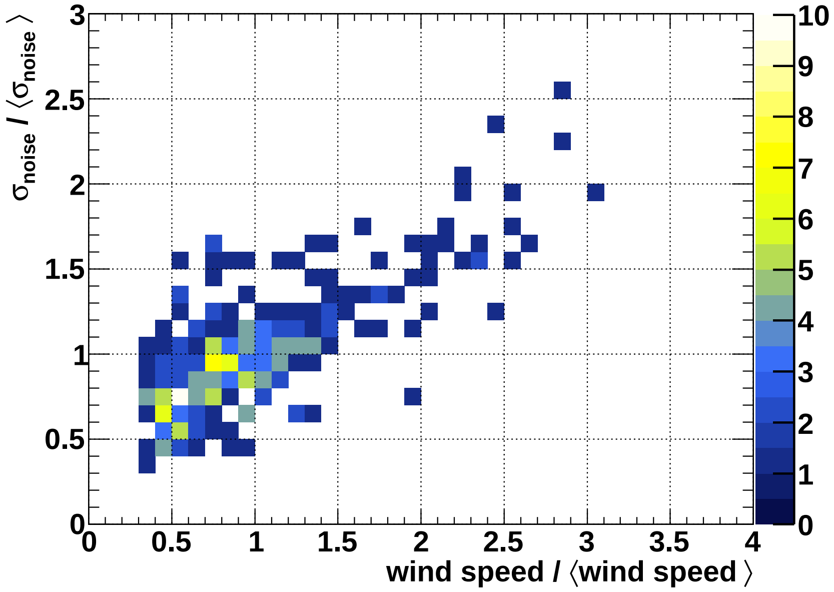

Figure 4.11: Daily averages of the noise level and the wind speed were derived and divided by the annual mean for the year 2008. The scatter plot of the two variables confirms the dependence of the noise on the weather observable with a correlation factor of 76%.

Chapter 5

Data reduction and signal processing

Contents

In this chapter a few techniques for signal processing will be explained and exemplary applications shown. The introduced procedures are used to improve the signal-to-noise ratio, for signal identification and for data reduction.

5.1 Band-pass filter

A very simple technique for signal processing is the application of a band-pass filter. Since neutrino-induced acoustic signals are primarily expected in a frequency band of 5 kHz $-$ 50 kHz suppressing the other frequencies significantly improves the signal-to-noise ratio. Simulations of neutrino-induced cascades with energies of $E_{\text{cascade}} > 10^{19}$eV show that a band-pass filter alone can be sufficient to suppress the background to a level enabling to trigger on a possible signal, e.g. by a simple threshold trigger[22].

5.2 Cross-correlation

Signals with a small signal-to-noise ratio (SNR) can be found by applying a cross-correlation[1]:

$$A(t) = ([r+s] \otimes s)(t) = \int_{-\tau/2}^{+\tau/2} d\tau' [r+s](t+\tau')s(\tau') \tag{5.1}$$

[1] A technique very similar to matched filtering, described in e.g. [23].

where $s(\tau)$ is the template of the expected signal and $(r+s)(\tau)$ is the measured pressure amplitude containing background r and possibly a signal s. $A(t)$ will have local maxima at times t where the signal template is similar to the recorded data indicating the existence of a signal at a time t. The identification of a possible signal is again triggered by the crossing of a threshold. An example for the application of a cross correlation filter can be seen in Fig. 5.1. Although in this example a threshold trigger would not suffice to identify the signal, additional methods for improving the signal-to-noise ratio can be applied. One of these methods will be explained in the following section.

5.3 Stacking

An effective method to improve the signal-to-noise ratio is *stacking*. Applied for decades e.g. in geophysics for the detection of seismic waves, this method uses arrays of sensors to identify a coherent signal. In the case of uncorrelated noise r and a fully correlated signal s in sensors i, j the mean instantaneous signal power for n sensors is

$$\left\langle S^2 \right\rangle = \left\langle \left(\sum^n s_n \right)^2 \right\rangle = N^2 \left\langle s^2 \right\rangle \text{ with } \left\langle s_i s_j \right\rangle = \left\langle s^2 \right\rangle,$$

while the mean noise reduces to

$$\left\langle R^2 \right\rangle = \left\langle \left(\sum^n r_n \right)^2 \right\rangle = N \left\langle r^2 \right\rangle \text{ with } \left\langle r_i r_j \right\rangle = \left\langle r^2 \right\rangle \delta_{ij},$$

thus resulting in a signal-to-noise ratio of

$$\frac{S}{R} = \sqrt{N} \frac{s}{r} \tag{5.2}$$

where, in our case, the sums run over the individual signals from all N hydrophones and $\langle\rangle$ represents the mean. The $\sqrt{N}$-dependence is the best-case scenario for completely uncorrelated noise, but clearly indicates the benefit of using a larger number of sensors operated in clusters as they can be used to improve the signal-to-noise ratio. In geophysics, detecting seismic waves at local stations, this method can be applied passively by reading out the sensors in parallel since the duration of the signal is large compared to the difference in arrival time at the different sensors. In our case, due to the signal length and dimensions of the sensors, an active procedure known as *beam-forming* has to be used. This method will be discussed in detail in Sec. 7.

The application of the introduced methods are demonstrated with results from simulations in Fig. 5.1 and 5.2. In the simulation the data for the noise and the signal were simulated assuming a sampling frequency of 200 kSps. The noise spectrum was modelled using the data from Fig. 4.8 for 13 knots of wind[2]. A cascade energy of 10^{19} eV at a distance of 200 m and a system of

[2] 1 knot = 1.852 km/h

six hydrophones have been assumed. For this example the signal arrival time is the same for all hydrophones. Figure 5.1 (top) shows the output of a single hydrophone with a signal at about 0.0019 s. Identifying the signal is impossible in this case.

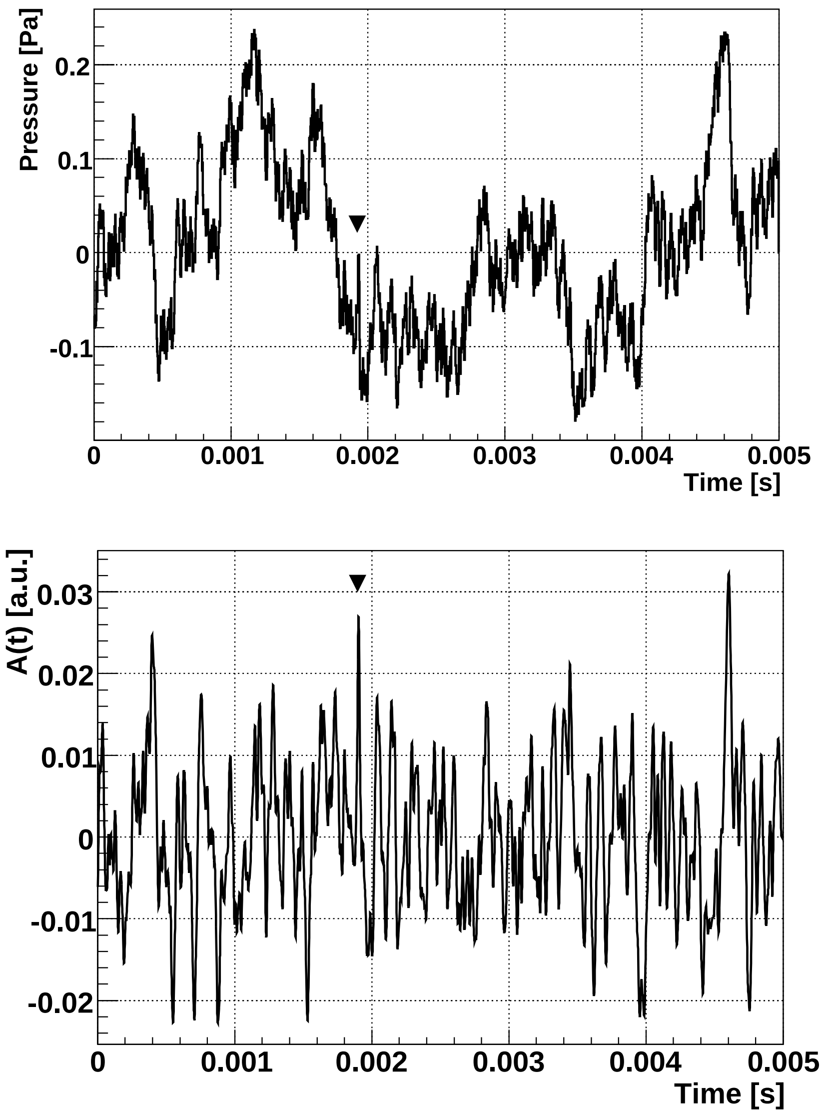

Figure 5.1: Top: Simulated output of a single hydrophone with a noise level corresponding to 13 knots of wind and a signal of a 10^{19} eV shower at 200 m distance, occurring at about 0.0019 s (see marker). Bottom: After application of a cross-correlation filter unwanted frequencies are removed. The SNR for the signal indicated by the marker is improved.

Applying a cross correlation significantly improves the signal-to-noise ratio of a single hydrophone as can be seen in Fig. 5.1. Stacking the output of all six hydrophones improves the signal-to-noise ratio to a point where a threshold trigger can be applied, see Fig. 5.2. Evidently a combination of all introduced methods is useful in order to successfully identify a signal. The advantage of using clusters of hydrophones in order to identify signals is a promising approach for future detectors. Furthermore, a cluster greatly simplifies the reconstruction of sources, which will be discussed in Sec. 7.

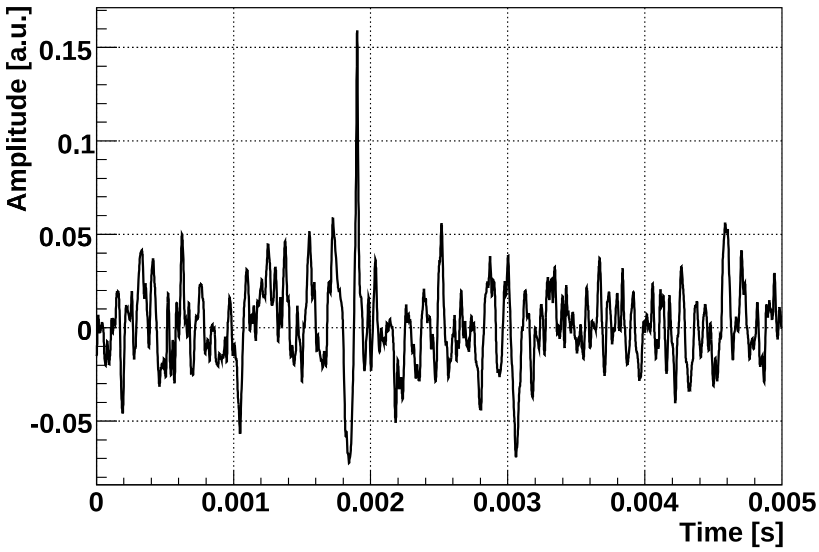

Figure 5.2: Stacked output of six hydrophones, after application of the cross-correlation. The signal at 0.0019 s becomes clearly visible.

5.4 Signal envelope

There are different possible methods to compute the envelope of a signal. A commonly used method is to take the square of the recorded signal and applying the result to a low-pass filter. In order to maintain the correct amplitude, the squared signal has to be multiplied by a factor of two since only the lower half of the signal energy is kept and the square root taken to adjust for the distortion created by squaring the signal. Alternatively the envelope of a signal can be computed by applying a Hilbert-transformation which has a much higher complexity than the method introduced. Figure 5.3 shows a signal and its envelope computed as described, using a low pass filter removing all frequencies above 16 kHz.

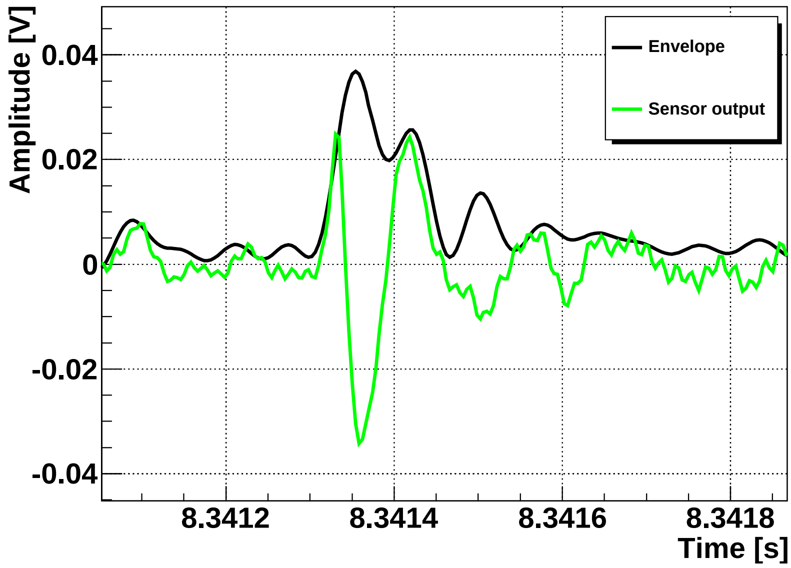

Figure 5.3: Recorded transient signal of unknown origin and its envelope.

Chapter 6

Prerequisites for data analysis

Contents

Before data of the AMADEUS system can be analysed a few corrections and processing steps have to be performed. This section discusses procedures especially needed for the location reconstruction of point sources.

6.1 Storey dimensions

Direction reconstruction is a prerequisite for source location reconstruction which is explained in Chapter 8. It is performed on each storey individually and thus requires precise knowledge of the sensor positions within one local hydrophone cluster. Due to the stiff fixation it is possible to measure the positions of the sensors in a cluster before deployment in the sea. The knowledge of the distances of three hydrophones to a reference point on the cluster structure and the distances between all hydrophones allows to obtain their locations unambiguously. Figure 6.1 shows a schematic of an acoustic storey.

A more detailed description of obtaining the positions in relation to each other will be explained in the following.
The following coordinate system was chosen. Hydrophones one (H1), three (H3) and five (H5) lie in a horizontal plane with z equal 0. The hydrophone H1 is at the origin. The x-axis points in the direction of H3. Geometrical calculations render the positions

$$\begin{aligned} r_{H_1} &= (0;0;0) \\ r_{H_3} &= \left(\overline{H_1H_3};0;0\right) \\ r_{H_5} &= \left(\overline{H_1H_5}\cos(\beta);\overline{H_1H_5}\sin(\beta);0\right) \end{aligned}$$

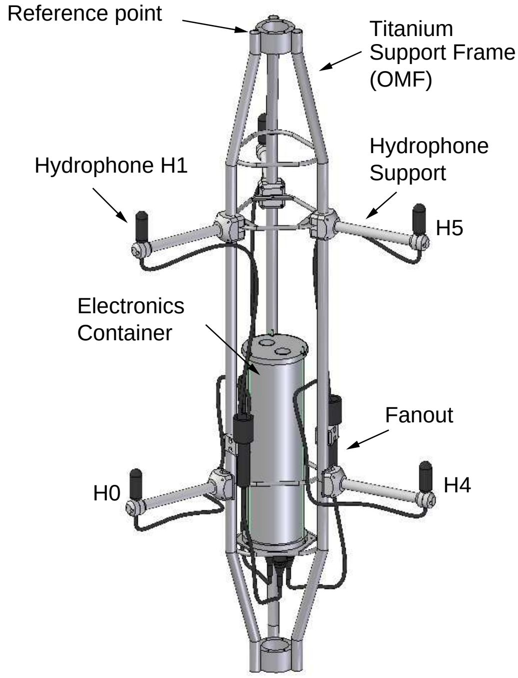

Figure 6.1: Schematic view of a storey. To calculate the positions of the hydrophones the distances of the hydrophones to each other are measured. Additionally the distances of the Hydrophones one, three and five to a reference point are measured enabling computation of the absolute positions of the hydrophones in the coordinate system of the storey.

of the three hydrophones with

$$\beta = \arccos\left(\frac{\overline{H_3H_5}^2 - \overline{H_1H_5}^2 - \overline{H_1H_3}^2}{-2\cdot\overline{H_1H_5}\cdot\overline{H_1H_3}}\right).$$

The positions of the hydrophones zero, two and four are given by

$$\begin{aligned} r_{H_{n_x}} &= \frac{\overline{H_1H_n}^2 - \overline{H_1H_n}^2 - \overline{H_{5_x}}^2}{-2H_{5_x}} \\ r_{H_{n_y}} &= \frac{\overline{H_3H_n}^2 - \overline{H_1H_n}^2 - (H_{n_x} - H_{3_x})^2 + H_{n_x}^2 - H_{3_y}^2}{-2H_{3_y}} \\ r_{H_{n_z}} &= -\sqrt{\overline{H_1H_n}^2 - H_{n_x}^2 - H_{n_y}^2}\,, \end{aligned}$$

where $r_{H_{n_x}}$, $r_{H_{n_y}}$ and $r_{H_{n_z}}$ are the x-, y- and z-coordinate of the n-th hydrophone ($n \in 0, 2, 4$), respectively. The reference point on the frame of the storey is calculated in a similar manner and is

$$
\begin{aligned}
r_{P_x} &= \frac{\overline{H_3P}^2 - \overline{H_1P}^2 - H_{5_x}^2}{-2H_{5_x}} \\
r_{P_y} &= \frac{\overline{H_5P}^2 - \overline{H_1P}^2 - (r_{P_x} - H_{3_x})^2 + r_{P_x}^2 - H_{3_y}}{-2H_{3_y}} \\
r_{P_z} &= \sqrt{\overline{H_1P}^2 - r_{P_x} - r_{P_y}}\,.
\end{aligned}
$$

Once the coordinates of the hydrophones and the reference point have been computed they have to be transformed to a general coordinate system which is the same for all storeys. This is achieved by rotating the storey by an angle defined by the reference point and the x-axis of the storey coordinate system and translating the coordinates by the displacement of the reference point with respect to its position in the storey coordinate system.

The calculation of the positions of the piezos within the acoustic modules works in a similar way.

6.2 Signal timing corrections

The correct timing of the detected signals is of utter importance as most analyses performed require accurate signal timing information. An exception is the study of the direction independent background noise as no temporal correlations between sensors are need. Direction reconstruction on the other hand requires the individual signal arrival times which are then processed further. Correct timing relative to the start of a data taking run is insured by an ANTARES internal clock with a 50 nano second sampling. During data analysis, however, a problem with the correct assignment of the times to the data samples was discovered. To further explain the problem a closer look at the ANTARES data format has to be taken. Data samples in the ANTARES data format are grouped in so-called items. Each of these item contains 128 samples and is tagged with an item time allowing to compute the time for each sample, given the sampling rate. The items generated are then placed in frames of predefined length of 104.8576 milliseconds. Each frame is also tagged with a time-stamp giving the start time of each frame and a frame number sequentially counting each produced frame since the start of a run. These frames are generated on each ANTARES storey and sent to shore where the frames of all sensors are combined forming time-slices. Correct timing of the frames is ensured by a reset time stamp (RTS) signal which resets the internal clock of a storey every four frames leading to a total duration of 419.4304 milliseconds ($2^{23} \cdot 50\,\mathrm{ns}$). All data taking is synchronised using the RTS. During data analysis it was discovered that the frame time was not always reset according to the RTS. Larger time values for the samples in the first frame in each rts cycle were possible. As time assignment of the AMADEUS data works by counting frames, evaluating the item time and add for each sample according the sampling rate this obviously posed a problem. It was discovered that the first item in a frame could contain data samples from a previous frame created by the release mechanism of the frame in the storey DAQ hardware. In order to solve the given problem the item time stamp of each item had to be accounted for performing corrections if necessary.

6.3 Positioning

Source reconstruction, see Chapter 8, is dependent on the position and orientation of each individual storey. Therefore calibrating the position[1] of the storeys is a crucial link in the chain of event reconstruction. The ANTARES detector is equipped with an acoustic positioning system comprising one transceiver on the base and four receivers on the storeys per line. These emitter signals, of known frequency and emission time and sent every two minutes, can also be used for the positioning of the acoustic stories of the AMADEUS system as their emission frequency and strength is well within the recording abilities. Two methods to reconstruct the storey position and orientation have been investigated so far, see Fig. 6.2. One uses the reconstructed signal direction (the reconstruction method will be explained in Chapter 7) from individual storeys. Detailed studies of this method have shown that the directional reconstruction accuracy is not sufficient to position the storeys within a few centimetres [24]. Another method, developed in cooperation with R. Lahmann, is being used. The general idea is: The time difference between the known emitter time of the positioning system and the detection time of the hydrophones give the distance to the emitters. Using the known positions of these emitters, the individual hydrophone positions can be reconstructed. They have a known position within a storey (see Sec. 6.1) which allows to determine the orientation and position of the storey. This technique will be explained in more detail in the following.

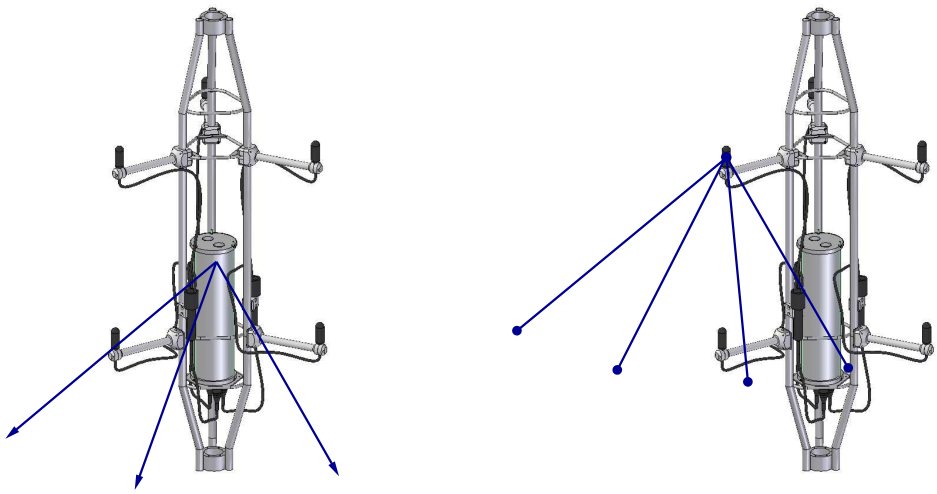

Figure 6.2: Left: Storey positioning using direction reconstruction. The directions to separate emitters are identified. This angular information can be used to determine the position of the storey. Right: The positions of single hydrophones are triangulated measuring the distance of several emitter to the hydrophone by comparing the emission and the reception time.

Every two minutes the ANTARES positioning system emits a predefined cycle of acoustic

[1]The position of the individual storey varies with time due to the forces of the deep-sea current of up to 35 cm/s on the line.

pulses ranging from 45 kHz to 60 kHz. The cycle start time and the emissions times are written to a database for later access. Knowing the emission times of each signal originating from the base of the lines, the first task is to accurately measure the reception times. A specialized filter recognizing the emitter signals of the positioning system was implemented in order to make this task easier. After the signal identification the envelope of the signal is calculated and the signal reception time defined by the passing time of a threshold. This is done for every acoustic sensor of the AMADEUS system. After determination of the reception times the signal run-times, from each emitter to each receiver, are used for sensor triangulation [2]. Given the slight change of sound velocity ($\sim 7\,\mathrm{m/s} \approx 0.5\%$) as a function of depth the mean velocity, ignoring the sea current, is chosen for triangulation. The mean velocity is given by sound velocities of the vertical positions of the emitter and the receiver. Once the positions of the individual hydrophones are computed, the results are used to fit the positions of the hydrophones to the positions measured prior to deployment. This can be done since the hydrophone positions within a cluster are fixed in position by their support structure. The repeated measurement of the storey dimensions of a recovered Line showed discrepancies at the centimetre level and a mean deviation of 1.34 cm, which is in the order of the measurement accuracy [3]. Fitting the reconstructed positions to the measured ones is achieved by minimizing the distance of measured hydrophone positions to the computed hydrophone positions.

$$\min\left(\sum_{i,j}^{n,m}\left(d_{i,j}(x,y,z,\theta,\phi,\epsilon)\right)^2\right) \tag{6.1}$$

The result of the minimisation gives both the orientation and the position of the storey. Every storey of the ANTARES detector is equipped with a 3-D magnetic field sensor (compass and tilt meter) in order to measure its orientation. Giving an independent measurement of the orientation a comparison of the two data sets is presented in Fig. 6.3. Completely independent from each other, these two methods render very similar results. While the basic structure of the orientation as a function of the time is the same for both methods the histogram 6.4 shows a systematic shift in the difference distribution. The deviation of $\approx 1.3^\circ$ is probably due to magnetic north and north defined in the coordinate system. The data obtained by reconstructing the position and orientation uses the UTM[4] coordinate system as a reference. A difference between the two directions would result in such an offset (see Fig. 6.4).

The positioning of the stories works well enough for the desired task of acoustic particle detection. While the uncertainty of the orientation is in the order of one degree the uncertainty of the positioning is about 20 cm, derived by comparing the data of this method with the one used by the ANTARES positiong system. Both are within acceptable limits for source location reconstruction.

[2]The emitter positions have been determined by cross calibration [25].

[3]This line was deployed, working on the sea bed for 302 days and then recovered for maintenance. The storey dimensions were measured before deployment and after recovery.

[4]The Universal Transverse Mercator (UTM) coordinate system divides the earth surface into rectangles. This allows the use of of a two dimensional Cartesian coordinate system to specify locations on the surface of the Earth.

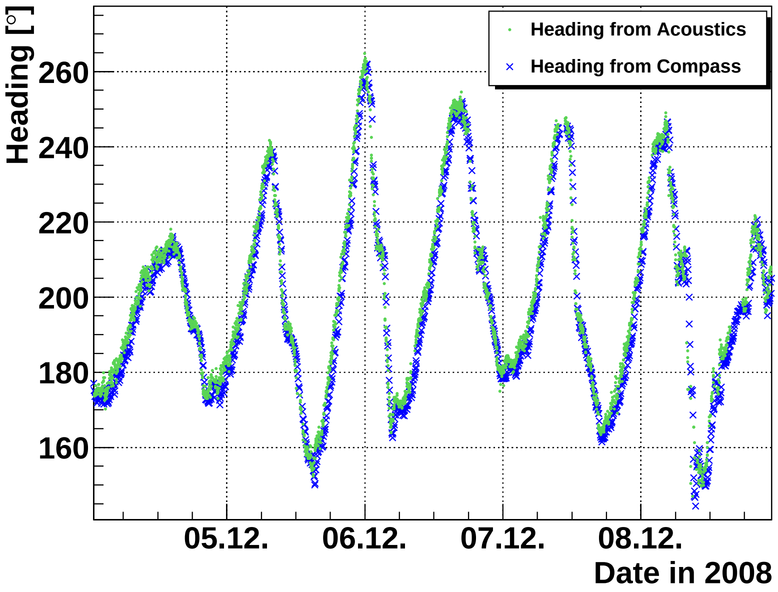

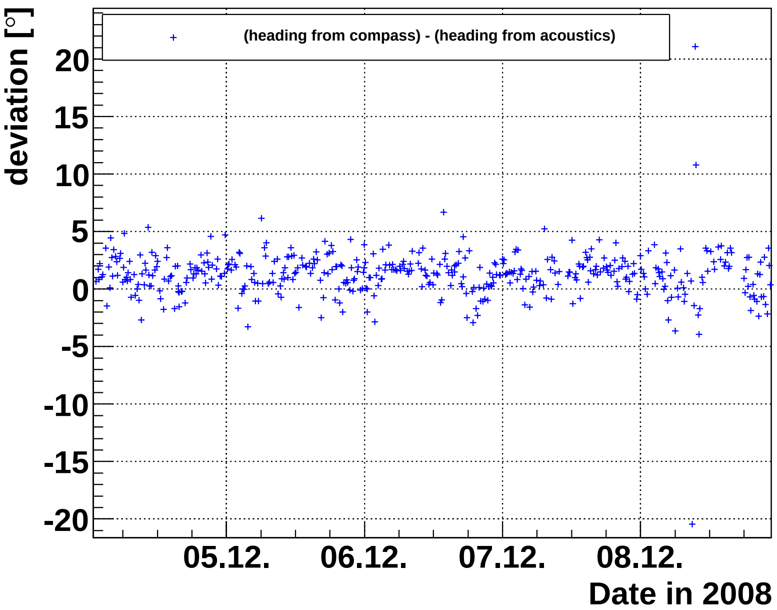

Figure 6.3: Top: Heading of an acoustic storey (storey 6, IL) both determined from the compass data and the results obtained from the position reconstruction. The results of both methods are in very good agreement. Bottom: The difference of the heading taken from the compass data and from the acoustic triangulation. The histogram shows a systematic shift of about $\sim 1.3^\circ$, see Fig. 6.4. The mean difference is $\sim 1.3^\circ$ and the RMS $\sim 1.6^\circ$.

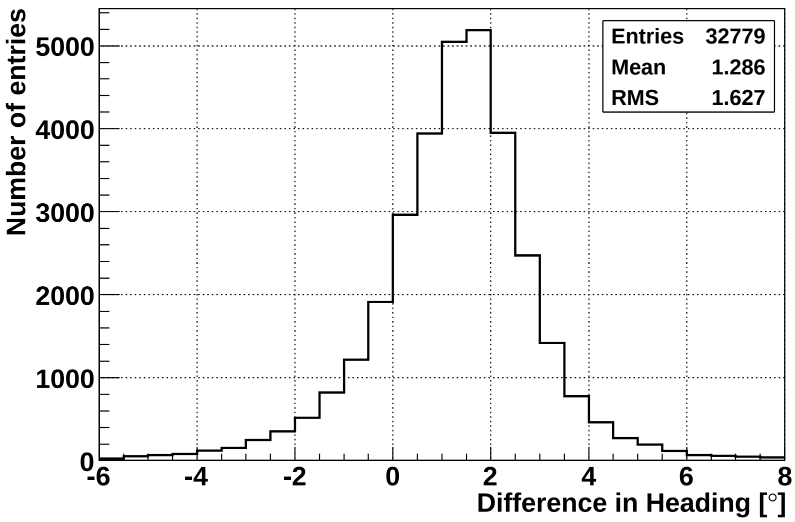

Figure 6.4: Histogram of the difference between the values obtained by the two methods for the orientation of storey six of the Instrumentation Line, see also Fig. 6.3.

Chapter 7

Direction reconstruction

Contents

The AMADEUS storeys each forming a local cluster of hydrophones, have been specifically designed to simplify direction reconstruction. In the following, the investigated direction reconstruction methods and all necessary steps will be explained. Analyses using the methods will be presented.

7.1 Signal selection

The data acquisition system of AMADEUS uses a number of on-line signal filters which select and classify signals before data storage. The different identified signal types are:

- Threshold crossed, i.e. the signal amplitude passed a threshold greater 2.5 times the RMS
- Pinger, signals emitted by the positioning system and found by an amplitude threshold of 8 times the RMS and analysing the frequency of the signal

- Possible Pinger, same as pinger without matching frequency.
- Bipolar type signal, signal with bipolar content found by a cross-correlation method

The next analysis steps are applicable to all types. After selecting one type only data of this type will be processed. The signal arrival time is defined as the time a signal exceeds a predefined threshold. This value depends on the RMS of the recorded data therefore the RMS is determined first. After this the envelope of the recorded signal is computed, as described in chapter 5.4, and used for all further signal analysis. The data is processed by scanning for signals exceeding a predefined threshold. If the threshold is passed the signal trigger time is recorded. For further processing the following signal features are stored together with the envelope of the recorded signal.
They are:

- recording sensor
- Signal reception time
- Maximum amplitude
- Mean amplitude (for the time above the threshold)
- Variance
- Signal duration (time above threshold)
- Orientation of the storey (from compass data)

The data is acquired individually for each sensor for a defined period of time. After preprocessing the signals and extracting their features they are grouped for each storey for the direction reconstruction. Grouping is achieved by looking at a transient signal of one sensor on a storey and checking for signals in the other sensors within a time window (1 ms) given by the dimension of the storey and the velocity of sound in water ($\sim 1500\,\mathrm{m/s}$). Additionally, the signals must have comparable signal amplitudes and durations. In case of AMADEUS the signal detection rate is low and the probability of chance coincidences almost negligible. Therefore the similarity requirements are not necessarily needed. After signal grouping the data is passed on to the direction reconstruction, discussed in the following chapter.

7.2 Direction reconstruction

7.2.1 Beam-forming

One method for direction reconstruction is beam-forming which scans the entire solid angle (4π) for the highest sound intensity. This is achieved by shifting the signals p_n of every single hydrophone n in time. The time shift corresponds to the difference in path length of the sound wave for a given direction. Hence each direction in space corresponds to a set of time differences Δt_n in the data. For a direction $\vec{k}$ and an array of N hydrophones with coordinates r_n $(n = 1, 2..., N)$, the overall signal at the time t is given by

$$b(\vec{k}, t) = \sum_{n=1}^{N} w_n p_n(t - \Delta t_n(\vec{k})) \,, \tag{7.1}$$

where the w_n represent weighting factors for the hydrophones. These factors can be adjusted to match the directional sensitivity of the hydrophones. Once $b(\vec{k}, t)$ is calculated the global maximum within the event time frame of about 1 ms is stored from each direction. The maximum of these values indicates the signals direction, the time shift for which all signals interfere constructively. In the following calculations $w_n \equiv 1$ was used. The time differences Δt_n are computed assuming a plane wave[1] and a constant speed of sound within the storey. The algorithm scans 4π with a predefined step size by applying pre-calculated time differences from a look-up-table to the data. Once all directions are scanned, the maximum value of the produced output indicates the direction of the signal. Figure 7.2 shows the output of the beam-forming algorithm for the time signal presented in Fig. 7.1. In this case the beam-forming algorithm was applied to the raw signal.

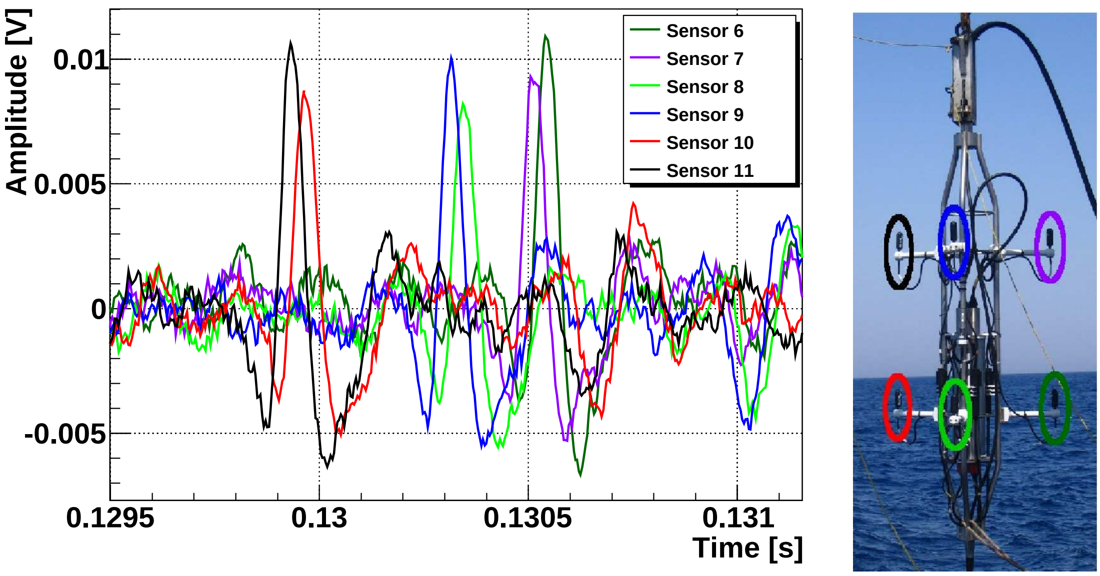

Figure 7.1: Time signature of a transient signal as received by each hydrophone (sensors 6 to 11) of the 2nd storey on the Instrumentation Line.

[1]For point sources this is not entirely true, but it is a sufficiently good approximation if the distances are large compared to the dimensions of the hydrophone antenna.

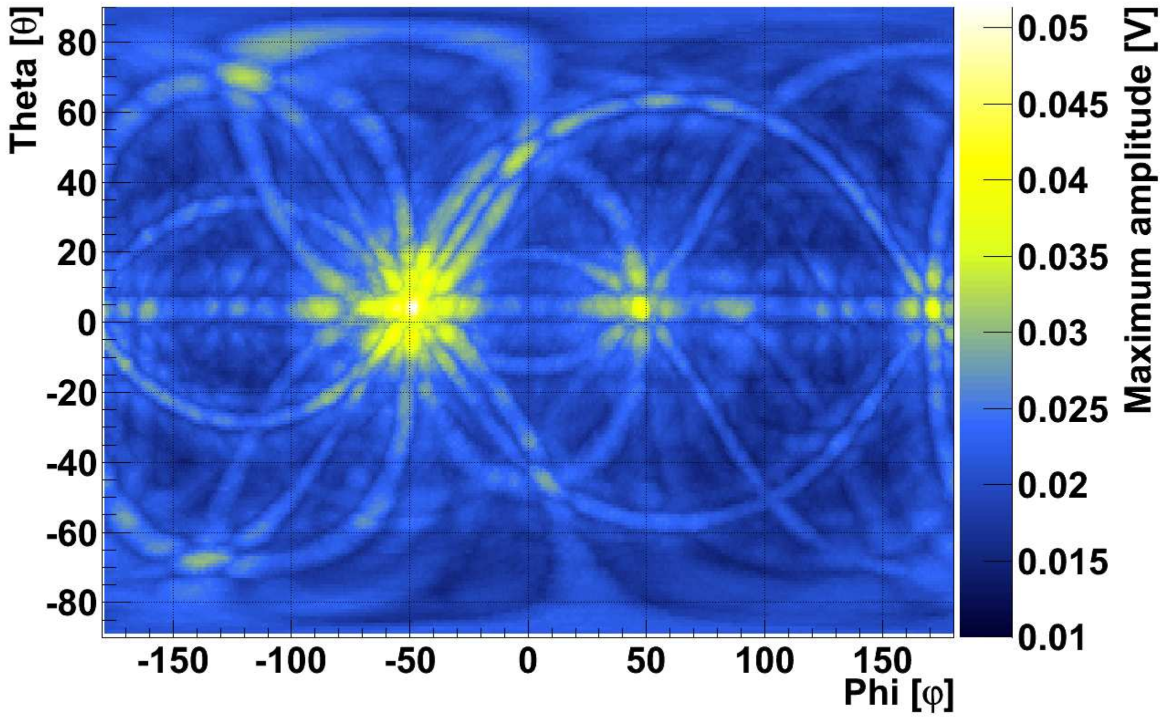

Figure 7.2: The output of the beam-forming algorithm. The maximum can be clearly seen at about 4° in the θ angle and $-49°$ in the ϕ angle. There all sensor signals overlap. Rotation patterns are resulting from solutions where two or more hydrophones create a larger output.

7.2.2 Time difference

Another method for direction reconstruction uses the timing information of a transient signal within a cluster. An approaching plane wave will reach each hydrophone within a cluster at different times depending on the direction the signal comes from. These signal arrival times t_{i_m} are extracted from the recorded data following the procedure described in Chapter 7.1 and the time differences between the hydrophones computed. These times are then compared to the expected time differences t_{i_e} pre-computed for each storey. This is done using equation

$$f(\theta, \phi) = \sum_i (t_{i_m} - t_{i_e})^2 \tag{7.2}$$

The expected time t_{i_e} can be rewritten to $t_0 + \Delta z_i / c$, where t_0 is a reference time, Δz_i the spatial difference between a reference position and the current hydrophone and c the velocity of sound.

Minimizing the resulting function allows to calculate for t_0.

$$
\begin{aligned}
\frac{\delta f(\theta,\phi)}{\delta t_0} = \sum_i^n 2(-1)\left(t_{i_m} - t_{i_e}\right) &\stackrel{!}{=} 0 \\
\sum_i^n \left(t_{i_m} - t_0 - \frac{\Delta z_i(\theta,\phi)}{c}\right) &= 0 \\
\sum_i^n \left(t_{i_m} - \frac{\Delta z_i(\theta,\phi)}{c}\right) &= n t_0 \\
\frac{1}{n}\sum_i^n \left(t_{i_m} - \frac{\Delta z_i(\theta,\phi)}{c}\right) &= t_0 \\
\left\langle t_{i_m} - \frac{\Delta z_i(\theta,\phi)}{c}\right\rangle &= t_0
\end{aligned}
\qquad (7.3)
$$

The output of the algorithm renders a three dimensional plot with a global minimum indicating the direction of the acoustic wave analysed. Figure 7.3 shows the output of the algorithm applied to the transient signal shown in Fig. 7.1. The minimum is well defined and clearly indicates the direction of the signal. Since the time residual plot is created with entries for every direction reconstruction the global minimum can always be found.

The angular resolution of both algorithms, beam-forming and time-difference, is dependent on the step size of the algorithms and the precise knowledge of the hydrophone positions. While the step size can be adjusted, the uncertainty of the hydrophone positions, both from the storey dimensions and storey position calibration remains. The angular resolution can thus ideally be determined with an external source. This will be discussed in Chapter 7.3.

7.3 Angular resolution

Knowing the angular resolution of a system is vital in order to assess its detection accuracy. The angular resolution of the individual stories of the AMADEUS system was obtained using the emitters of the positioning system of the ANTARES detector. The positioning system consists of a number of emitters at fixed positions which is ideal for this task. To get the directional resolution one month worth of emitter emission data was analysed. The signal emission period is two minutes resulting in about $20,000$ signals for this time frame for each emitter. Figure 7.4 shows a scatter plot of the reconstructed directions for one emitter of the ANTARES positioning system. The resolution in both zenith (θ) and azimuth (ϕ) was determined by fitting a two dimensional Gaussian to the reconstructed positions, providing an angular resolution of $0.5°$ in θ and $3.3°$ in ϕ.

There are a variety of uncertainties summing up to the resolution obtained. Each line is anchored to the sea bed by a dead weight and held upright by a buoy. Therefore the line can bend and twist in the current. Since the storeys are semi-free to move in space, only connected by an electro-mechanical cable, each reconstructed direction requires a correction which is also

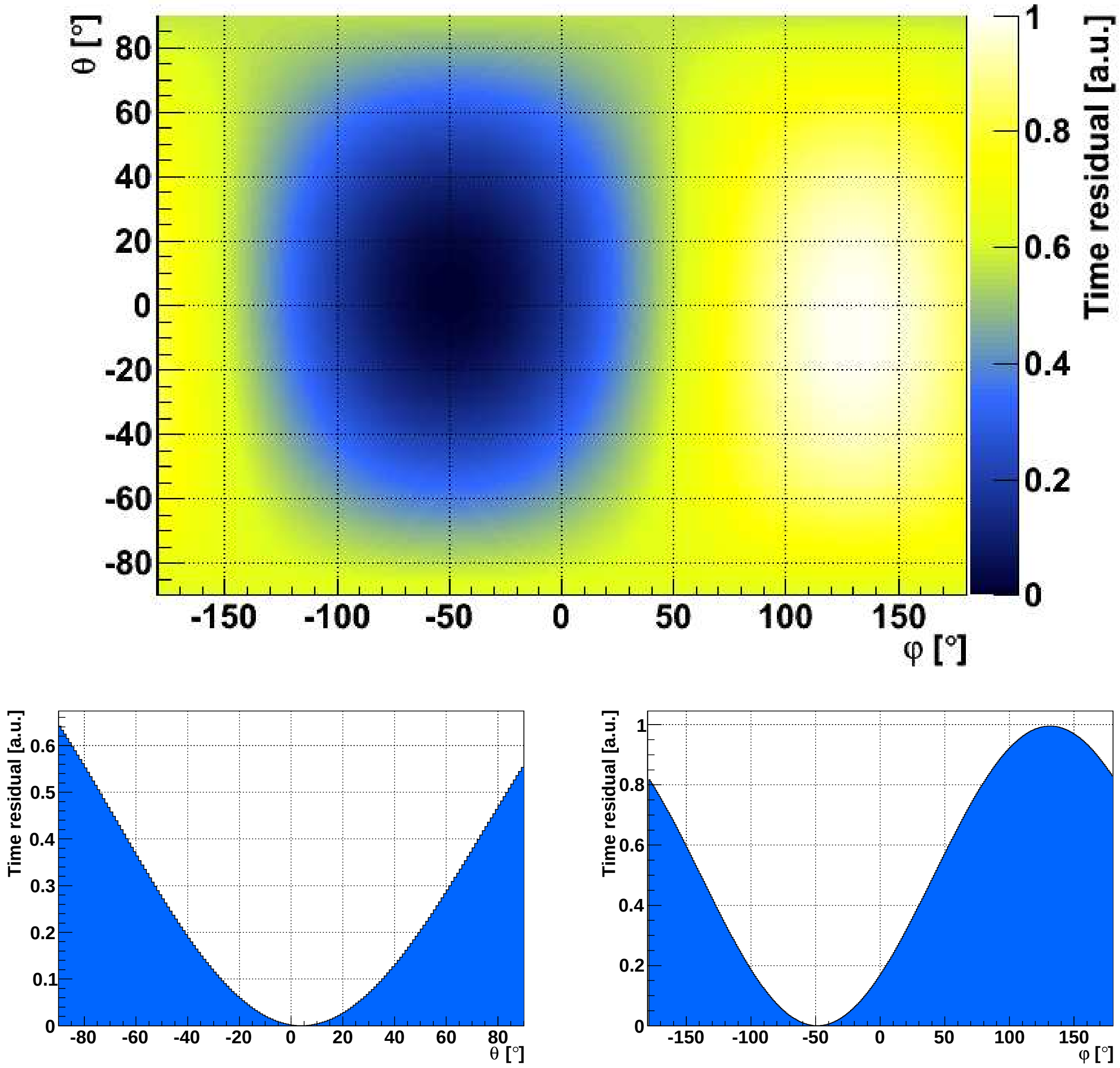

Figure 7.3: Top: The result of the sum in equation 7.2. The global minimum identifying the reconstructed direction at $\theta = 4^\circ$ and $\phi = -49^\circ$can clearly be seen. Bottom: A projection of the minimum in the zenith (θ) and the azimuth angle (ϕ). Since the time residual is calculated for all directions the global minimum is always found.

afflicted with an error. While the line shape is governed by the buoyancy of the mechanical structures and the force generated by the sea current on those structures, the rotation is mostly arbitrary. The line shape results in a negligible tilt of the storey from the upright position of the storey (RMS $\approx 0.2^\circ$). Rotation, however, needs to be accounted for. This is done by using the data of the on-board compass, present on every storey. All possible errors sum up to the values mentioned above. The achieved accuracy is adequate for acoustic neutrino detection.

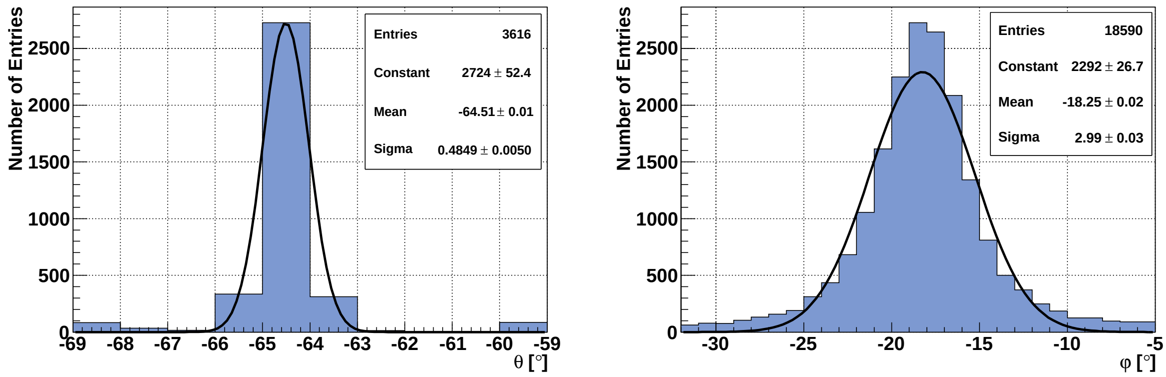

Figure 7.4: Direction reconstruction of emitter five of the ANTARES positioning system from Storey 22. The error for the reconstruction is $\sim 0.5°$ in θ (left plot) and $3.3°$ in the ϕ angle (right plot).

7.4 Sky-map

The direction reconstruction allows to investigate the noise distribution of the complete underwater environment around the detector. Fig. 7.5 shows a qualitative mapping of the arrival directions of transient acoustic signals originating in the surrounding of the ANTARES detector. The data were recorded during the time period between 01.10.2008 and 01.11.2008. All filtered signals during this time period were used. Taking this data set, the directions of all transient signals with an amplitude greater than four times the RMS were reconstructed. The RMS was calculated for a 10 s time interval around the respective signal time. The origin of the coordinate system represents storey 22 of Line 12 at about 400 m above the sea floor. A virtual observer resides on this storey, looking north towards the horizon of the storey, thereby defining the origin. The arrival directions are plotted using the area conserving Hammer-Aitoff projection. Figure 7.5 shows several interesting features. In the lower hemisphere the ANTARES positioning system can clearly be identified by its emissions. The upper hemisphere containing about 85% of the transient signals shows a lot more activity. Interestingly a few hotspots as well as tracks can be identified. The hotspots correlate well with the directions of harbours around the detector, as can be seen in Fig. 7.6.

In the direction of Marseilles (300°), for example, an excess of signals can be seen. Identifying these directions allows for only one conclusion, that the tracks correspond to ship traffic. Even though signals emitted by ships will not be detected all the way from Marseilles, most ships, especially ferries, will follow shipping routes pointing from or towards a harbour, so there will be an increased number of signals originating from such routes. As a ship comes closer to the detector its direction, with respect to the detector angular reference frame, changes significantly creating one of the noticeable tracks in the plot. Increasing the distance to the detector, the ship can contribute to one of the hotspots depending on its destination. A notable feature of the hotspots pointing towards the directions of different harbours is their lateral dimension. Assuming they do originate from ships heading in these directions there should not be any signals

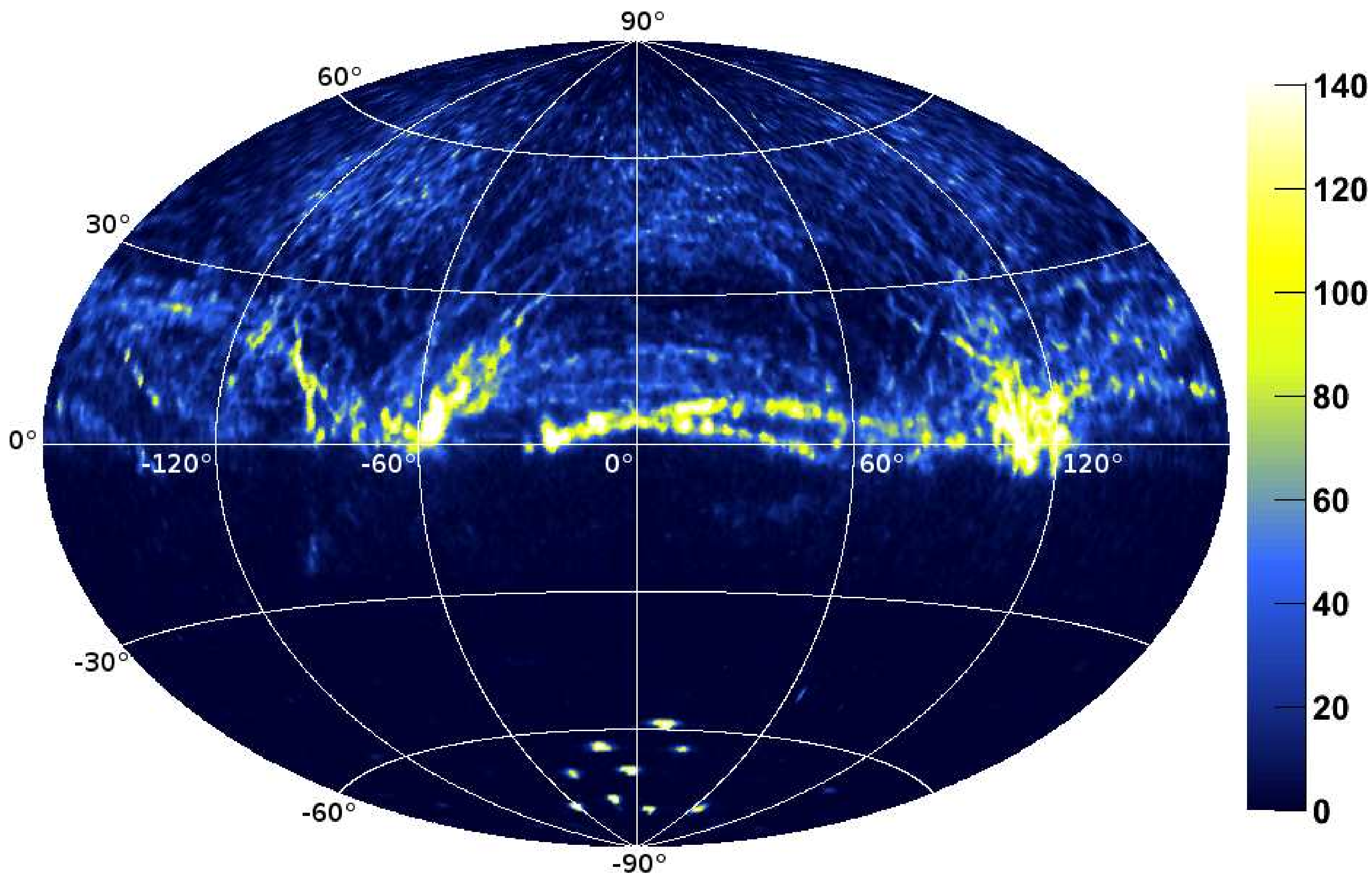

Figure 7.5: Mapping of the arrival directions of transient signals from the time period 01.10.2008 to 01.11.2008. A virtual observer is looking north towards the horizon. On the bottom of the plot the ANTARES positioning system can be seen. The upper hemisphere shows most of the activities, as expected. Visible tracks seem to originate from ship traffic. Hotspots in the plot correlate with direction pointing towards the harbours nearby.

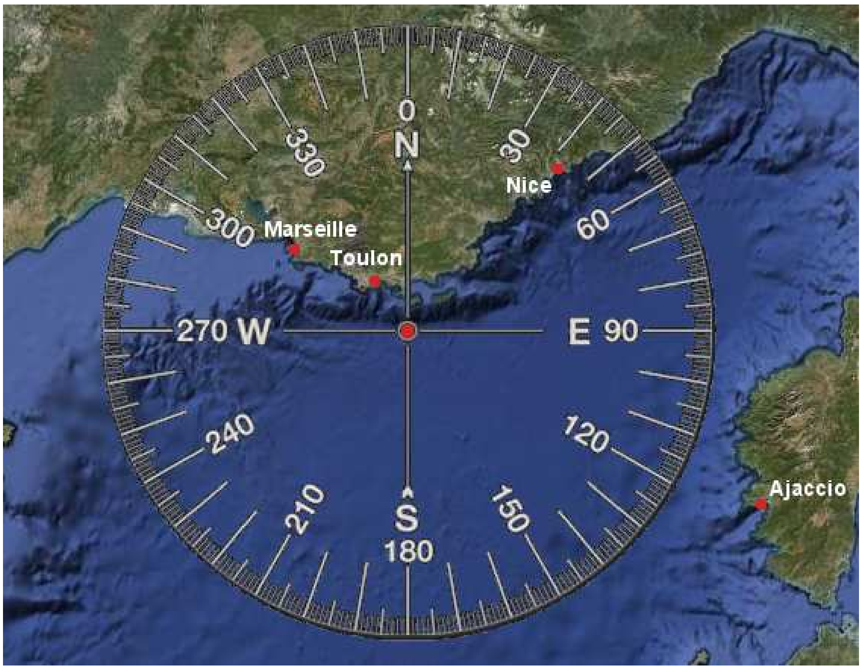

Figure 7.6: A map of the region around the detector for comparison with the direction identified in Fig. 7.5. The ANTARES detector is located at the centre of the compass rose.

detected below the horizon of the storey for straight line sound propagation and the curvature of the Earth's surface neglected. The curvature of the earth is in fact completely negligible for distances in the range of a few hundred kilometres. Straight line sound propagation, however cannot be assumed for large distances. Evaluating equation (4.19) for distances greater than 1 km leads to the results presented in Fig. 7.7. The results indicate that identified directions in the range from $\theta = -5.5^\circ$ to $\theta = 5.5^\circ$ can be assigned to sources coming from the surface at horizontal distances between 12 km and 30 km. This, of course, is only true for sources located on the sea surface which can only be positively confirmed in case a source location reconstruction is performed, which will be explained in detail in the following chapter. A reconstructed data set of source positions will indicate that the conclusions drawn here are in fact appropriate.

The sky-map gives a general idea of where signals are coming from and helps to identify the origins of the signals. Since all types of signals were used for this analysis no explicit conclusion with respect to acoustic neutrino detection can be drawn. With respect to background reduction one could however concentrate on signals originating from the lower hemisphere.

7.5 Direction reconstruction of a moving emitter

For the identification of the sources of the noise, a closer look at one of the tracks was taken. Figure 7.8 shows an example of such a track. The directional data was taken from storey 22 on Line 12 and shows a moving emitter passing east of the detector. The azimuthal angle φ

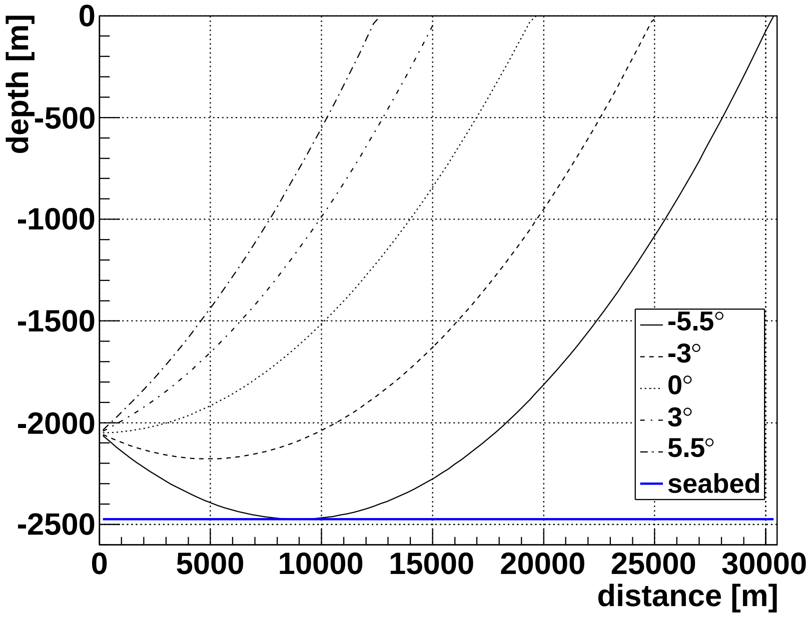

Figure 7.7: Sound ray propagation assuming a constant sound velocity gradient using Eq. 4.19.

varies from north east (45°) over east (90°) to east south east (110°) while the zenith angle only varies from 60° to 20° always pointing upward. Interruptions of the track in Fig. 7.8 are due to the emissions of the ANTARES positioning system rendering the acoustic system deaf for that period of time. For this example all signals in the selected time period were analysed, resulted in the reconstruction of reflections and other sources active at the time.

This demonstrates the capability of the AMADEUS detector to clearly identify moving targets.

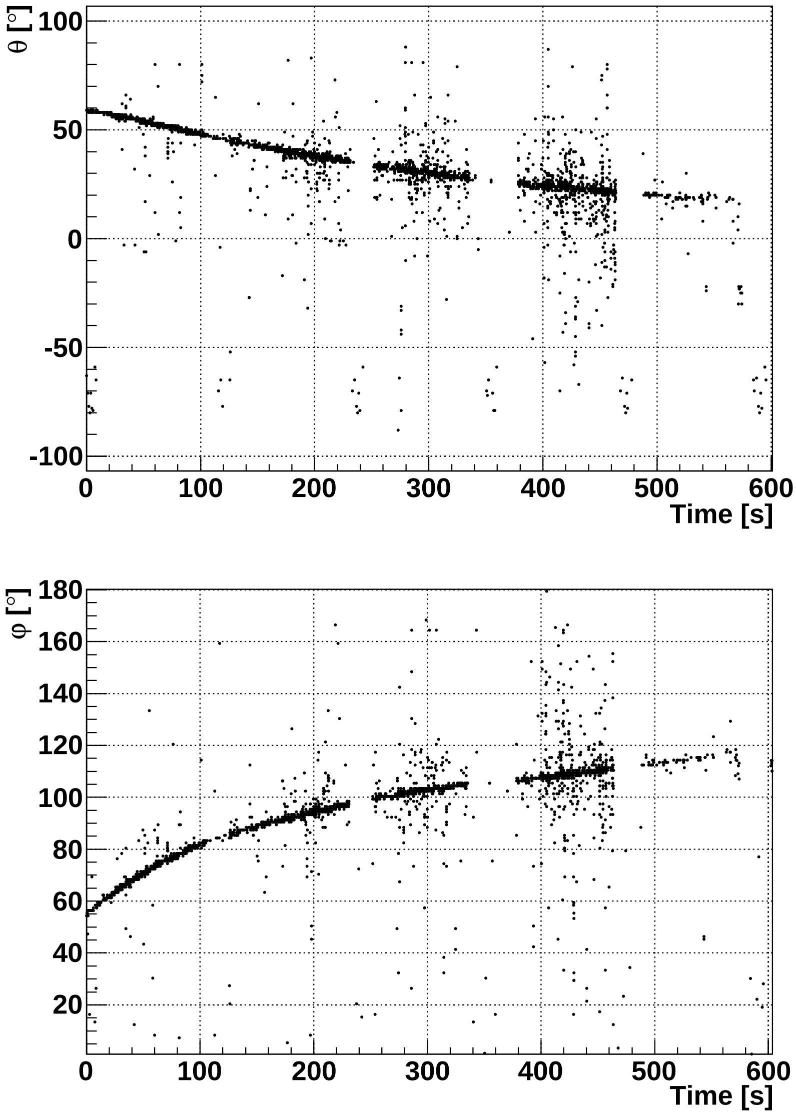

Figure 7.8: Reconstruction of the zenith (θ, upper plot) and azimuthal angle (φ, lower plot) as a function of time of a moving emitter. Interruptions in the detection of the signal are a result of the ANTARES positioning system rendering AMADEUS ”deaf” for the duration of the signal emission.

Figure 7.9: Left: Picture of Line 12 on its transport palette aboard the Castor on route to the ANTARES site. The acoustic and optical sensors are protected by opaque bubble wrap until a short time before deployment. The yellow buoy keeps the Line straight. Right: An acoustic storey on the hook waiting to be lowered into the water.

7.6 Deployment of Line 11

The ANTARES detector, due to its special requirements, is situated at a remote deep sea location resulting in complex operations for detector instalment and maintenance. Each of the 12 Lines had to be deployed separately in so-called ”Sea Operations”, taking about a day for one Line. The deployment of the 11th of the 12 Lines was done on the 26th of April 2008. Deployment of the ANTARES Lines involves the transportation of the Line to the ANTARES site (see Fig. 7.9), located about 30 km south of Toulon in France, followed by a lengthy procedure of lowering the Line storey by storey into the water. Once the Line is fully submerged it is lowered by a winch (see front right of Fig. 7.9, left) at a rate of about one kilometre per hour until it reaches the sea floor at 2447 m.

During the process of lowering, the position of the Line is constantly monitored in order to steer the Line to the desired position on the sea bed. This is done using a number of transducers located on the bottom of the Line, on the hook supporting the Line, on the boat and on the sea bed. The frequencies used are 9, 12 and 15 kHz with 9 kHz emitters located on the bottom and the top of the submerged Line. The AMADEUS system of the detector was running at the time of the deployment and was thus able to track the submerging Line as well. This was done using two different techniques discussed in the following.

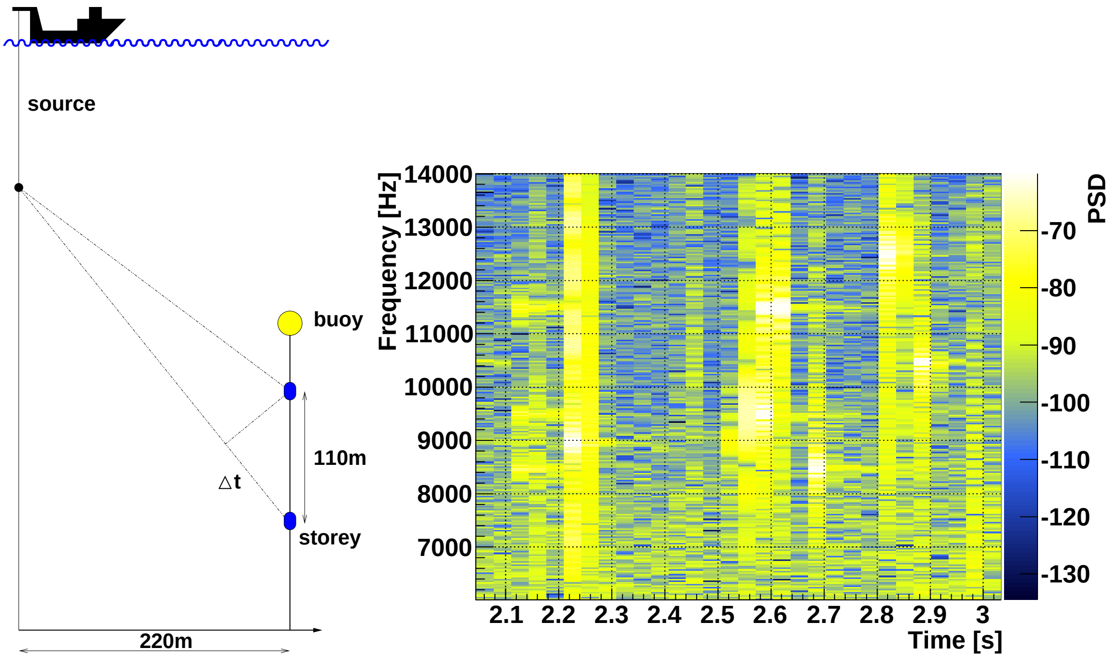

Figure 7.10: Left: Schematics of the deployment and the geometry used for reconstruction. Right: Pinger cycle with an arbitrary time offset used for the Line positioning.

7.6.1 Two storey tracking

Two storey tracking utilizes the signal arrival times of an acoustic emission at two separate stories. The reception time for each storey is defined by the mean reception time of the sensors on the storey. The difference in the arrival time at two stories can then be used to track the Line. For a schematic view see Fig. 7.10 left. Correlating signals on different stories required the use of signal selection techniques specifically tuned for the signals used by the Line positioning system in order to select the correct signals for tracking the Line. Since the frequencies of the emitters were known, it was possible to use the power spectral density of the recorded data to identify the signal in the frequency domain. The power spectral density was computed for time windows of 0.03 s. Once a signal was detected in the desired frequency band the signal time was recorded. In addition to the frequency selection, a coincidence trigger was applied, expecting signals in a time window defined by the stories' spatial distance.

The Lines' position as well as the lowering rate was kept approximately constant during the deployment operation once the Line was completely submerged. The time information and the assumption of a plane wave results in a zenith angle of the emitter of:

$$\theta(t) = \arctan\left[\frac{h_i - v_L t}{d_{L1,L2}}\right]. \tag{7.4}$$

where h_i is the initial vertical distance of the sensor to the emitter, v_L the lowering rate and $d_{L1,L2}$ the horizontal distance between the deployed Line and the Line equipped with the acoustic system. In Fig. 7.12 the reconstructed emitter angles were fitted with equation 7.4, leaving the lowering velocity as a free parameter. The resulting value of $0.3206 \pm 0.00015\frac{\mathrm{m}}{\mathrm{s}}$ well matches the rough speed of $\approx 1\frac{\mathrm{km}}{\mathrm{h}} \approx 0.3\frac{\mathrm{m}}{\mathrm{s}}$ given by the deployment crew. The results include a few miss-reconstructed events most likely due to reflections. Signals coming from a direction of about 85° can be assigned to the ship while the signal roughly following the movement of the Line originate from the emitter located on the hook at the top of the Line.

7.6.2 Single storey tracking

Single storey tracking was done to verify the result obtained with the two storey tracking method as well as to test the performance of the direction reconstruction method utilized for a single storey.

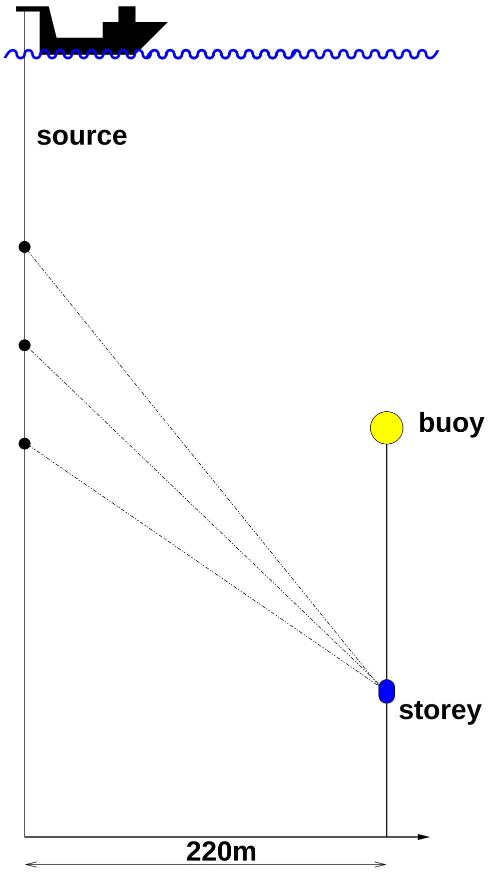

Figure 7.11: Schematic drawing of the single storey Line tracking. Directions of the signals coming from the emitter are reconstructed using the direction reconstruction method described in 7.2.2

.

In this case the arrival time differences between the hydrophones on one storey were used to identify the zenith angle of the approaching wave, see Chapter 7.2.2. Signal selection was done by applying a filter passing several frequency bands. This multi band-pass filter passes the signals central frequency (9 kHz) and its first two harmonic frequencies within a band of 500 Hz. A threshold trigger was then applied to the selected transient signals. Signals of different hydrophones on one storey arriving within a time window (0.001 s, given by the sound velocity and the dimensions of a story) and similar characteristics, such as signal amplitude and duration, were grouped. The grouped signal arrival times were used for direction reconstructed using the time difference method described in Section 7.2.2. The results obtained were again fitted using Eq. 7.4 rendering consistent submersion speed of $0.3208 \pm 0.000129\frac{\mathrm{m}}{\mathrm{s}}$. Differences in the reconstructed directions in Fig. 7.12 originate from the difference in vertical positions of the observer, one is the physical position of the storey and one is the midpoint between two stories. This could theoretically be corrected for, but since both methods were regarded as a test of the capabilities of the system this was not done.

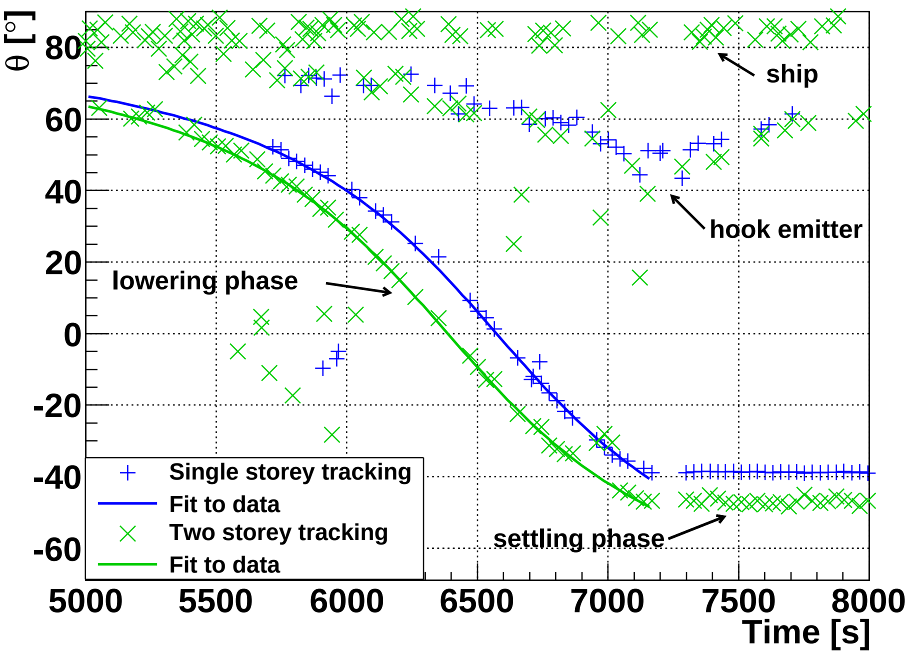

Figure 7.12: Reconstructed directions as a function of time. The data points very well match the fit functions indicating a lowering rate of 0.321 m/s.

Both methods for direction reconstruction have proven to work well. Single storey tracking has the big advantage of simple signal selection. Due to the shorter time windows, on the storey scale, it is a lot easier to identify signals originating from the same source.

7.7 Line 9 monitor

On the 2nd of July 2009, a sea operation took place to recover Line 9 for maintenance. Unfortunately, the acoustic release mechanism, triggered by a sequence of tones, did not work as expected leaving Line 9 in an unknown state of mechanical fixation. Without visual inspection of the base of the line in order to investigate the cause for the malfunctioning release mechanism it was impossible to say if the Line was still properly fixed or would eventually release. In case of a release, the Line would rise to the surface and drift in the current. In order to minimize the probability of loosing the Line, the immediate information of its release is helpful. Therefore the Erlangen acoustic group was asked to use the AMADEUS system to monitor the status of the line by tracking its depth. Tracking was possible because of two autonomous emitters on the release system of the line. In a common effort, by Kay Graf, Max Neff and the author of this thesis, software was implemented allowing the ANTARES collaboration to monitor the status of the line. The monitor consisted of a special software signal trigger, sensitive to the characteristics of the emitter signals, a depth reconstruction and a web interface displaying the data obtained. The signal trigger, implemented by Max Neff, was achieved by cross-correlating the recorded

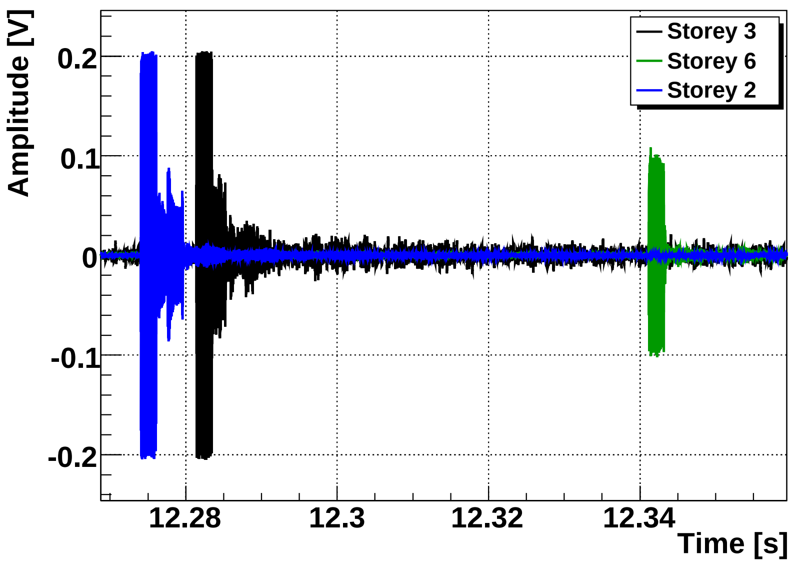

Figure 7.13: Time signature of the signal emitted by Line 9 received by storeys 2, 3 and 6 of the IL07. The signal reception times, defined by the crossing of a threshold, are used for depth reconstruction.

signal with the expected signal, a 9 and a 15 kHz 2 ms sinusoidal signal. Once a signal was detected, the arrival times of the signal at the acoustic stories of the Instrumentation Line was determined, the depth reconstruction applied following the procedures described below, and all relevant information of this event recorded.
The information recorded were:

- Run-number of occurrence
- Frame index of occurrence
- Frequency of the signal
- IDs of storey and sensor with detected signals
- Reconstructed depth of the emitter

Given the arrival times of the signals and knowing the distance of the Line with the acoustic system to Line 9, the depth could continuously be monitored. The depth of the line computes to

$$d = d_{sensor} - \frac{d_{IL-Line9}}{\tan\left(\arccos(d_{eff}/d_{storey})\right)}. \tag{7.5}$$

For a graphical interpretation see Fig. 7.14.

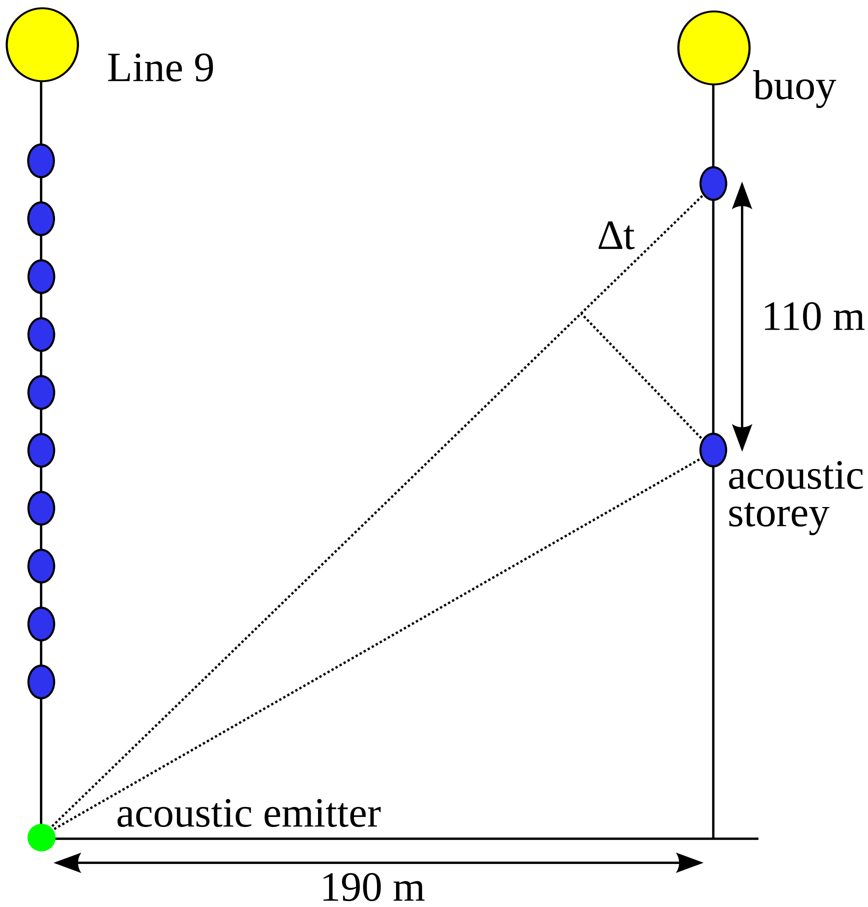

Figure 7.14: Schematical overview for the monitoring of the depth of Line 9.

Depth monitoring was done in two phases. During the first phase the emission rate was 0.1 Hz. This was initiated when the release mechanism was triggered so the Line can be tracked during its ascent. It kept running as long as the on-board battery of the first release mechanism beacon has enough power (about $100,000$ cycles). In order to have redundant systems, two release beacons are installed on the base of each line. Once the first release mechanism ran out of power the emitter on the second one was activated every 30 minutes with 3 emissions separated by 10 s. This was achieved by a dedicated autonomous mini line transmitting a request signal with a frequency at 15 kHz and acknowledged by a 9 kHz emission from the Line 9 beacon. Significantly reducing the emission frequency to three signals every 30 minutes immensely increased the lifetime of the battery of the second release mechanism. Fig. 7.15 shows the reconstructed depths for the two emission phases. In both plots the depth can easily be identified, even with reflections leading to a false depth reconstruction.

The data presented in Fig. 7.15 was displayed on a website continuously being updated, enabling the members of the ANTARES collaboration to monitor the status of the line. Additionally an automated alert message was sent to the Erlangen acoustics group in case of strange behaviour of Line 9. During the following ROV[2] operation Line 9 was securely fixed to the sea bed making sure it would not emerge on its own. Until then the Line 9 tracking system performed well informing the ANTARES collaboration of the status of Line 9.

[2]Remotely Operated Vehicle, an unmanned submarine to perform maintenance and construction tasks.

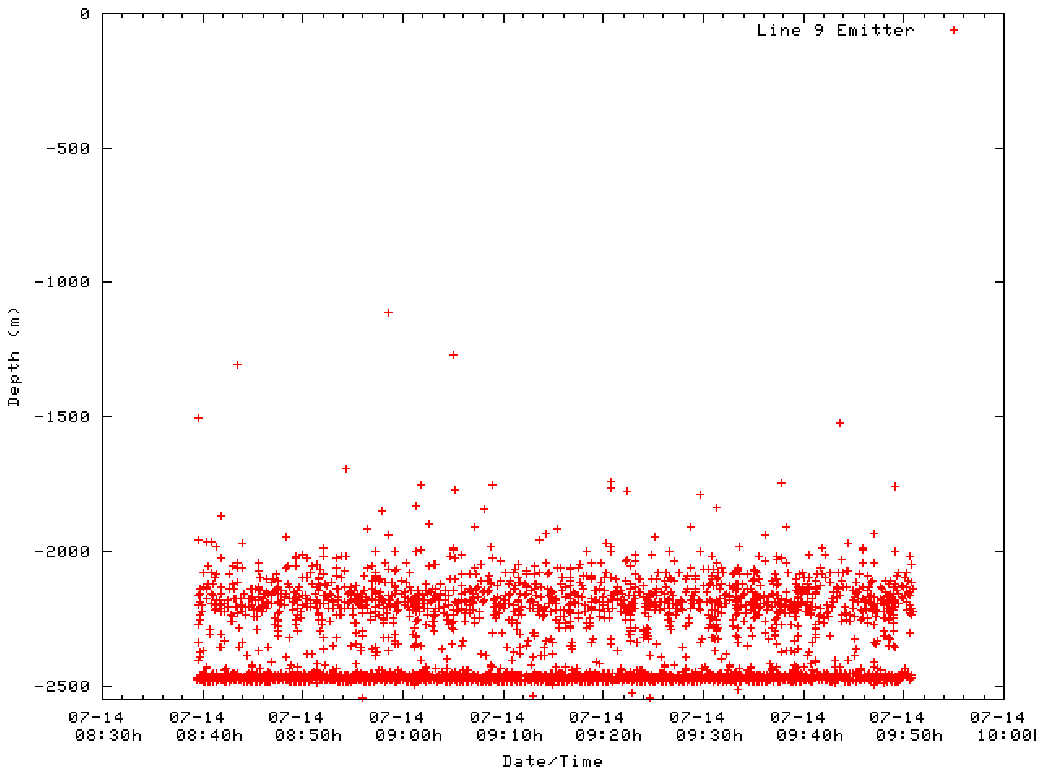

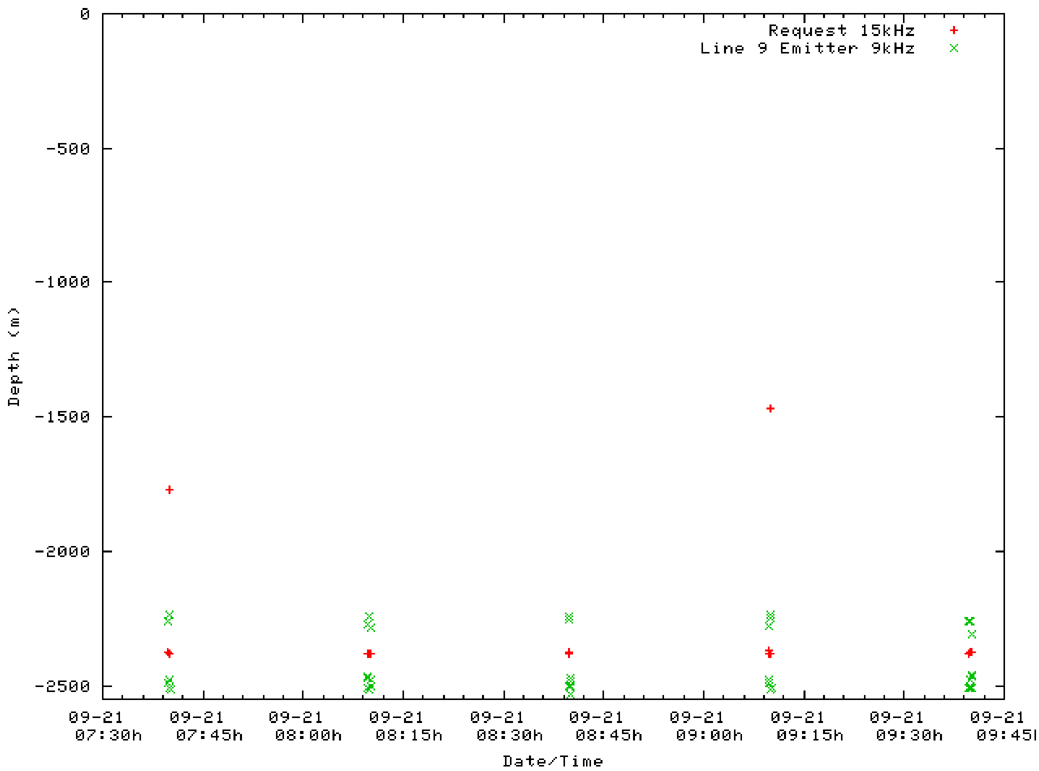

Figure 7.15: Reconstructed depth of the Line 9 emitter as a function of time. The upper plot shows the data for the short delay emission period while the lower plot displays the data for the long delay emission. Long delay emission is achieved by sending a request to the emitter.

Chapter 8

Source location reconstruction

Contents

The AMADEUS detector design is optimised for position reconstruction. As mentioned above, the short distances between the hydrophones within one cluster reduce the chance probability of detecting several signals at the same time. Therefore the assignment of the triggered events in several hydrophones to one signal is straight forward, given event rates < 1 kHz. In the case of high event rates the short time window of 1 ms, given by the size of cluster and velocity of sound, allow for fast signal processing. Additionally the spacing between the hydrophones within one cluster is large enough to reconstruct the direction with good accuracy by using the arrival time differences. The directional information of several clusters can then be used for source position reconstruction. This will be discussed in the following sections.

8.1 The source location reconstruction algorithm

The source location reconstruction algorithm presented here utilises the directional information given by the local clusters of the AMADEUS system, as described in Sec. 7.2. For cluster i that detected a signal, the reconstructed direction is given by the unit vector $\vec{k}_i$. Together with the position of each cluster $\vec{a}_i$, this defines a line in space

$$\vec{d}_i = \vec{a}_i + n_i\vec{k}_i \, , n_i \in \mathbb{R}. \tag{8.1}$$

The location of a source is, in principle, given by the intersection point of the lines $\vec{d}_i$. Due to the uncertainties in the direction reconstruction the source location is defined as the point closest to all lines. Localising the point of closest approach for all lines is realised by calculating the square distance from a point $\vec{s}$ to the reconstructed lines

$$L_i^2(\vec{s}) = (\vec{s} - (\vec{a}_i + n_i\vec{k}_i))^2$$

where n_i is the length of the vector $\vec{k}_i$. Varying L^2 allows to compute n_i.

$$\begin{aligned}\frac{\partial L_i^2(\vec{s})}{\partial n_i} &= 2(\vec{s} - (\vec{a}_i + n_i\vec{k}_i))\vec{k}_i \stackrel{!}{=} 0 \\ &\hookrightarrow n_i = (\vec{s} - \vec{a}_i)\vec{k}_i\end{aligned}$$

This results in

$$L_i^2(\vec{s}) = \left[\vec{s} - \vec{a}_i - \left((\vec{s} - \vec{a}_i)\vec{k}_i\right)\vec{k}_i\right].$$

$\vec{s}$ is computed by minimising $\sum_i L_i^2$ with a gradient minimisation algorithm.

8.2 Event selection

Proper event selection is crucial in order to correctly identify the position of a given source. It is achieved by selecting an identified signals' direction and correlating its temporal information on one storey with the temporal information of directions identified on other stories. This is achieved by demanding a coincidence within a time window defined by a plane wave and the storey positions. Given a plane wave and an identified direction on a reference storey, the effective distance between the reference and another storey, as seen by the plane wave, computes to

$$\mathrm{dist}(\theta, \phi) = \sqrt{c^2 + a^2}\cos\varphi \sin\left(\theta - \arctan\frac{c}{a}\right) \tag{8.2}$$

where a is the horizontal distance and c the vertical distance. θ and ϕ are identified by the direction reconstruction algorithm, see also Fig. 8.1.

Evaluating formula 8.2 and dividing it by the velocity of sound gives the time between the detection of a plane wave by two storeys in space. Assigning a time frame of $\pm 30\,\mathrm{m}/c_S$ allows to identify a coincidence window for a given direction identified.

In addition to the coincidence window, a second check is performed before the final source location is computed. If two signals are identified within a coincidence window their resulting directions are checked for convergence. This is done by computing the distance between the origins of each vector, the storey positions, and checking if this distance is reduced if both vectors are followed a predefined distance interval. Data analysis has shown that a distance interval of 10 m works well to perform this check.

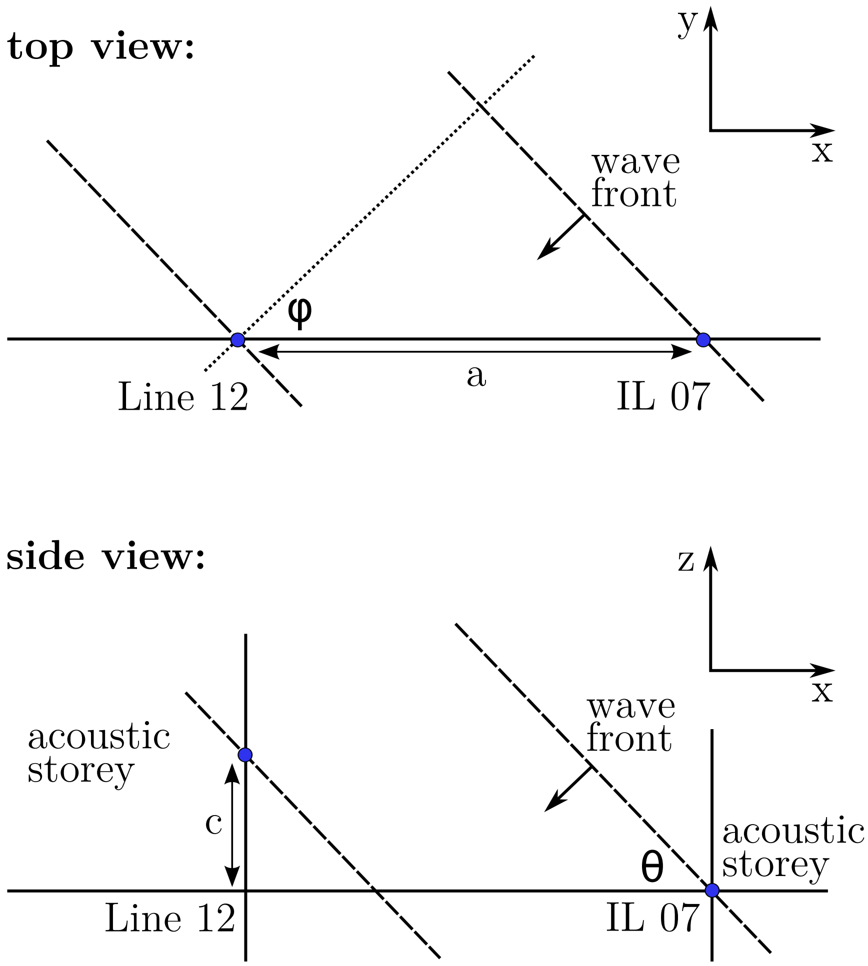

Figure 8.1: Geometry used for deriving formula 8.2. The given effective distance for a passing plane wave with direction θ and ϕ is padded with small window ± 30 m to account for uncertainties.

8.3 Simulations

The source location reconstruction method presented in Sec. 8.1 was tested with simulations. A set-up resembling that of AMADEUS consisting of six hydrophone clusters was used. The test was conducted as follows: First a source coordinate was defined at up to 1000 m distance, from where a spherical sound wave was emitted, propagating through the water at a constant speed of 1545 ms^{-1}. As sketched in Fig. 4.2, a particle-induced sound pulse does not propagate as a spherical wave. But, since the technique discussed is independent of the radiation pattern, a spherical wave was chosen as the most general case. A depth dependent velocity gradient causing the acoustic wave to be refracted was neglected due to the small effect given the distances analysed, see Sec. 4.3.2. The arrival times of the spherical wave at each single hydrophone were computed and the beam-forming algorithm (1° steps) was used to determine the directions of the wave for each storey. These directions were then used to reconstruct the source location. See Fig. 8.2 for the geometrical arrangement of acoustic sensors and the definition of the coordinate system.

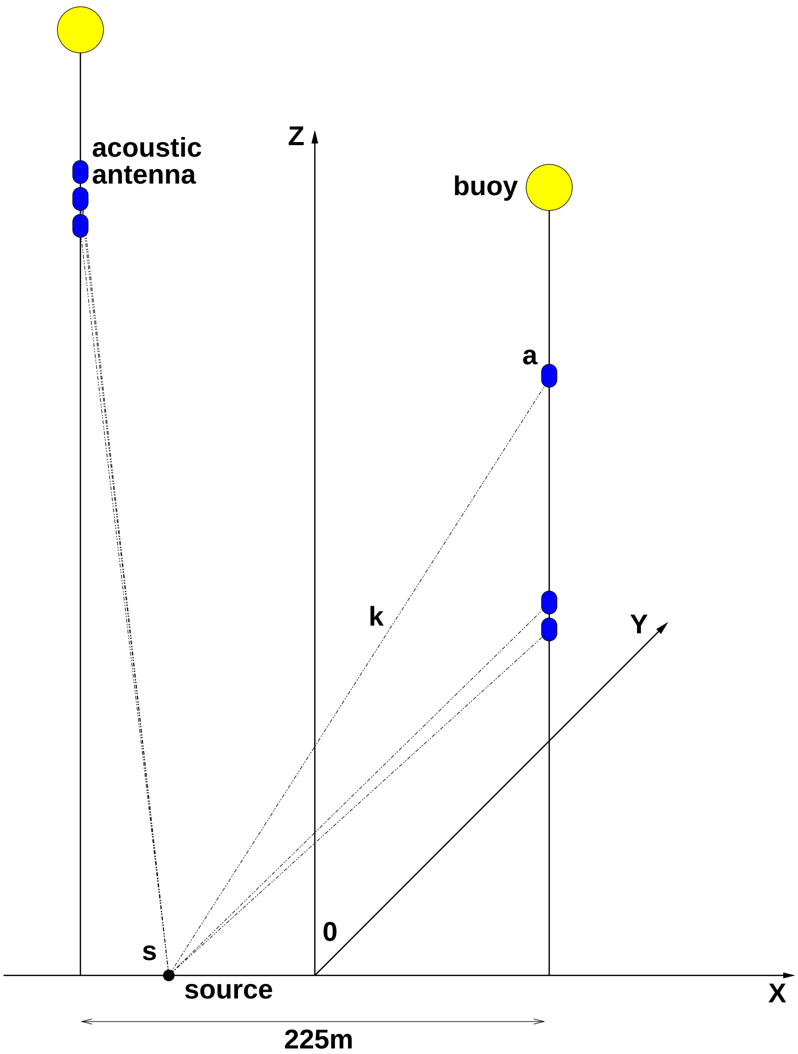

Figure 8.2: The geometry of the simulated acoustic set-up. The lines are 225 m apart, the vertical position of the stories are 180 m , 195 m and 305 m for the line on the right and 390 m, 405 m and 420 m for the Line on the left.

In the following, the error of the position reconstruction is defined as the difference between real and reconstructed source positions. Results of the simulation are given in Fig. 8.3. For the upper plot in Fig. 8.3 the z-coordinate of the source was kept constant while modifying the x- and y-coordinate. Errors range from about four meters in the close vicinity of the detector up to 25 m for more distant sources. A small asymmetry in the source reconstruction quality can be seen which is due to the asymmetric detector. The lower plot in Fig. 8.3 shows the z-dependence of the resulting error. Errors for sources placed on the z-axis hardly exceed 2 m up to 600 m. The error increases due to the angular resolution (less than $0.5°$) of the beam-forming algorithm. Generally the error of the source location reconstruction increase with smaller angles between the reconstructed directions. Given large angles for the sources along the z-axis the smaller error for these source compared to the sources on the sea bed can be explained. Both plots demonstrate that using local clusters for direction reconstruction and using that information to reconstruct a source is a good approach for point source localisation.

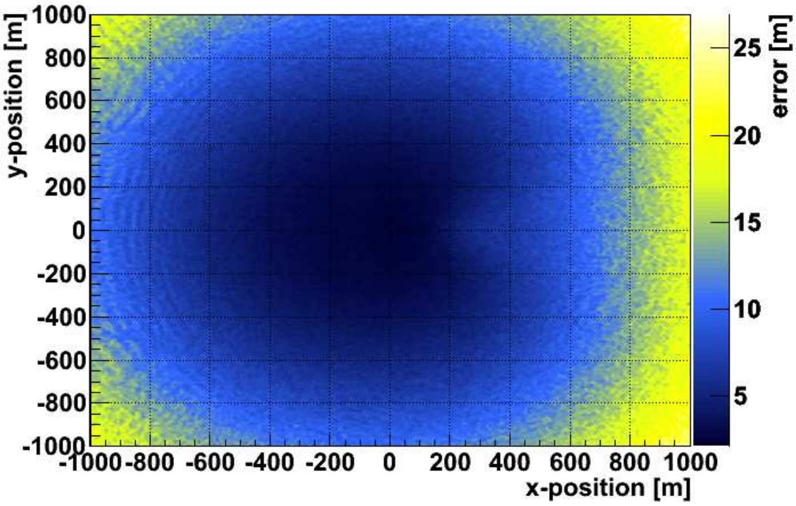

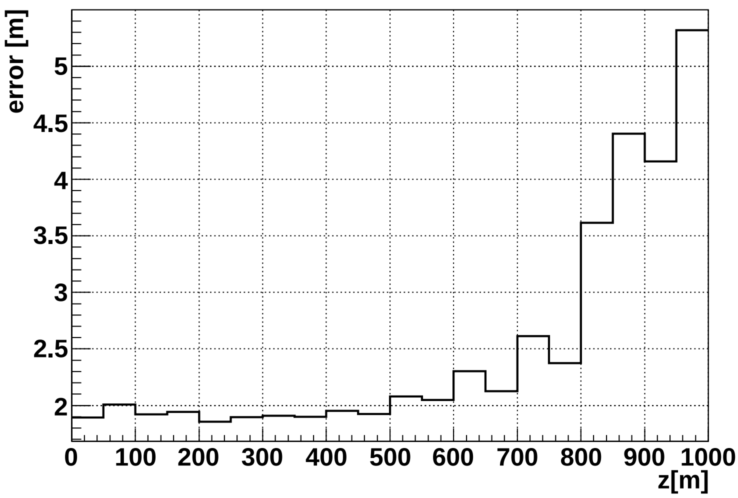

Figure 8.3: The position reconstruction error for the cluster set-up presented in Fig. 8.2. The error is the distance from the assumed source to the reconstructed source position. Top: Sources were placed in the xy-plane with $z = 0$. Bottom: Sources were placed along the z-axis.

8.4 ANTARES positioning system

The ANTARES positioning system offers a perfect test set-up for the source location algorithm, allowing to determine and compare the error with the simulated values. Figure 8.4 shows the xy-projection of the reconstructed positions of the emitters for a period of three months. Although at first glance the points seem to be spread rather broadly, the ANTARES sea floor layout can clearly be identified. The reconstructed positions used for this plot were only subject to very loose cuts consisting of a signal-type cut, signals identified as an emitter signal by the on-line filter, and a limited volume, 300 m above and below the expected positions and about 500 m in x and y. The volume cut was applied after the source location reconstruction. Emitter signal identification is done using a cross correlation trigger and is thus also sensitive to reflections and emitter-like signals, thereby reducing the overall accuracy. The signals can be identified more efficiently with respect to e.g. reflections with more stringent filters and using the known emission times, as shown for the positioning of the stories (Section 6.3). However, since the identification of unknown sources would suffer from the same background it was chosen not to do so in order to obtain a realistic estimation of the position reconstruction accuracy.

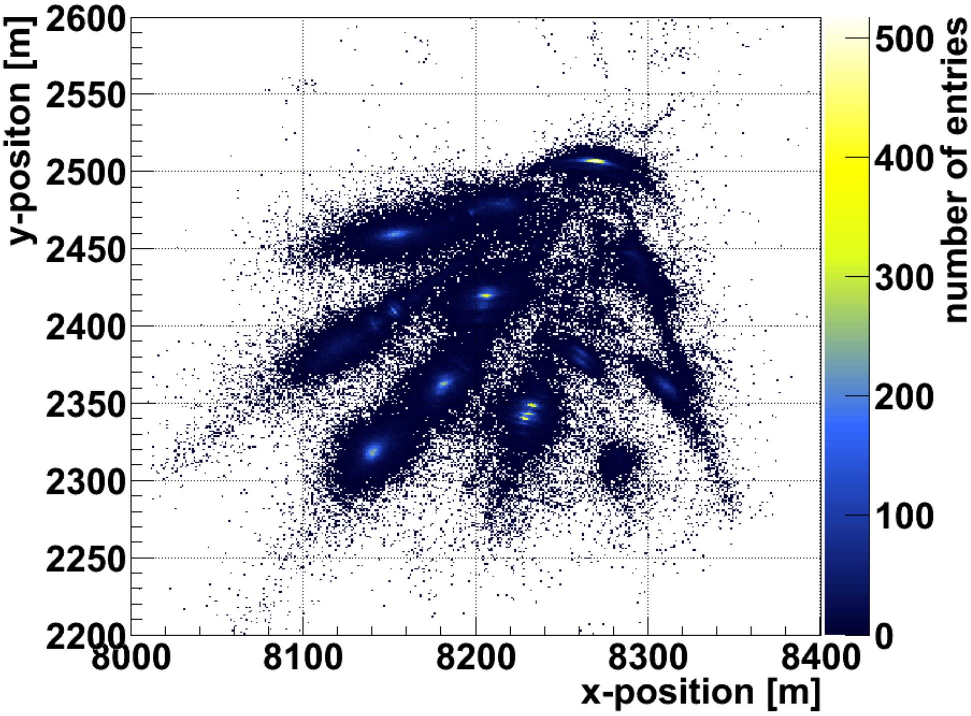

Figure 8.4: xy-projection of the reconstructed positions of the ANTARES positioning system. The data points were subjected to a volume cut only looking at 300 meters above and below the expected emitter positions.

For the evaluation of the accuracy two storeys were excluded. Storey 23 on Line 12 (see Fig. 3.3) presented some difficulties with respect to emitter identification resulting in missing position data for that storey during the studied time interval. Storey 21 on the same Line was excluded to keep a homogeneous detector with respect to the sensor design.

Taking a closer look at the data presented in Fig. 8.4 reveals the accuracy of the source reconstruction. A two-dimensional Gauss-function was fitted to each excess. Figure 8.5 shows the reconstructed positions with one sigma error bars. Additionally the nominal positions of the emitters are displayed.

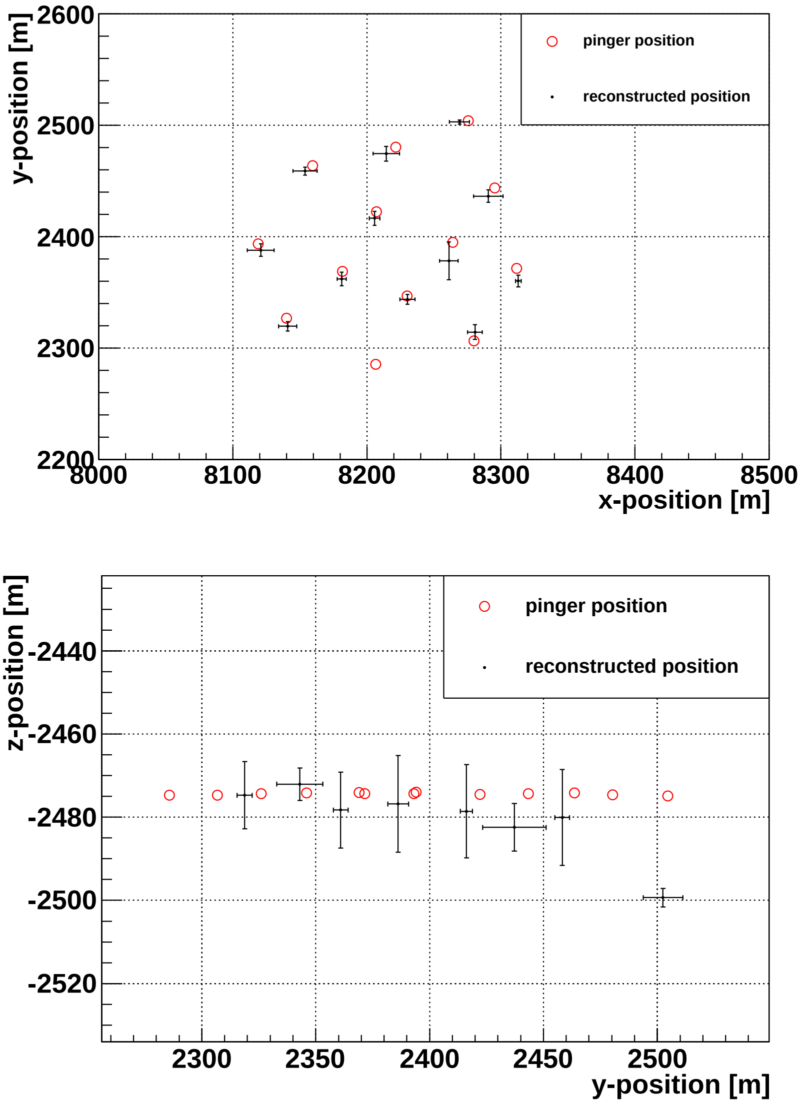

Figure 8.5: Reconstructed positions of the positioning system emitters. Top: xy-projection; Bottom: yz-projection. Positions given in UTM coordinates

The mean errors for the positions are:

$$\langle\sigma_x\rangle = 6.8\,\mathrm{m}$$
$$\langle\sigma_y\rangle = 6.1\,\mathrm{m}$$
$$\langle\sigma_z\rangle = 7.9\,\mathrm{m}$$

The errors computed in the simulation are close to the evaluated errors except for the z-value. Since the simulation uses a total of six clusters instead of just four in the real case scenario a difference is expected. In addition to the reduced number of clusters the error in positioning, which was not included in the simulation, introduces an additional uncertainty. All in all the accuracy of the source reconstruction is quite good and sufficient for its purpose of acoustic particle detection. The energy of a particle cascade is given by the amplitude of a detected signal. Since the attenuation length of sound in water is large (on a km scale) small errors in the source location reconstruction, as shown here, will hardly effect the reconstruction of the cascade energy.

8.5 Track of a moving emitter

Taking a look at the source distribution in the acoustic *sky-map* (Fig 7.5), one of the most prominent structures are the track-like signatures. An example of such a track can be seen in Fig. 8.6. The plots show the change in both θ and φ of two hydrophone clusters as a function of time. A rather extreme change in θ suggests a close approach to the detector. The φ values change from $\sim -50^\circ$ to $\sim 100^\circ$ indicating an origin in the direction of Marseilles and a destination in the direction of Ajaccio as can be deduced when comparing the direction with those in Fig. 7.6. Signals from that moving source were detected for distances of up to ten kilometres. Attenuation, the noise level at the observation time, as well as refraction limit the maximum distance a signal can be detected from the AMADEUS detector.

Results of the reconstructed positions are presented in Fig. 8.7 and show a source passing the detector with a minimum distance of about two kilometres from the hydrophone clusters. The source was moving at a constant velocity of 12 knots (1 knot = 1.852 km/h). Only signals with a vertical distance of 500 m from the sea surface were taken into account. The signals analysed had to be of similar amplitude and duration and had to be detected by at least two stories on two different lines.

Fluctuations in the reconstructed position of the source are due to uncertainties of the reconstruction. One standard deviation of the distance from the reconstructed positions to the fitted line computes to $115\,\mathrm{m}\pm15\,\mathrm{m}$ resulting in an angular resolution of a little over $^3\circ$ consistent with the angular resolution of the storeys. The great distance would require to account for the refraction of the signal. Since the signal passes a velocity gradient it is refracted. In addition to the velocity gradient due to the change in pressure as a function of the depth, signals originating from the surface pass a temperature gradient also changing the sound velocity and thus further complicating the reconstruction. While this effect can be neglected for the azimuthal angle it will effect the reconstruction of the zenith angle leading to a standard deviation of $250\,\mathrm{m}\pm10\,\mathrm{m}$ for the depth of the reconstructed positions.

Keeping in mind that refraction was neglected and the source is far from the detector the results presented quite impressively demonstrate the capabilities of the system.

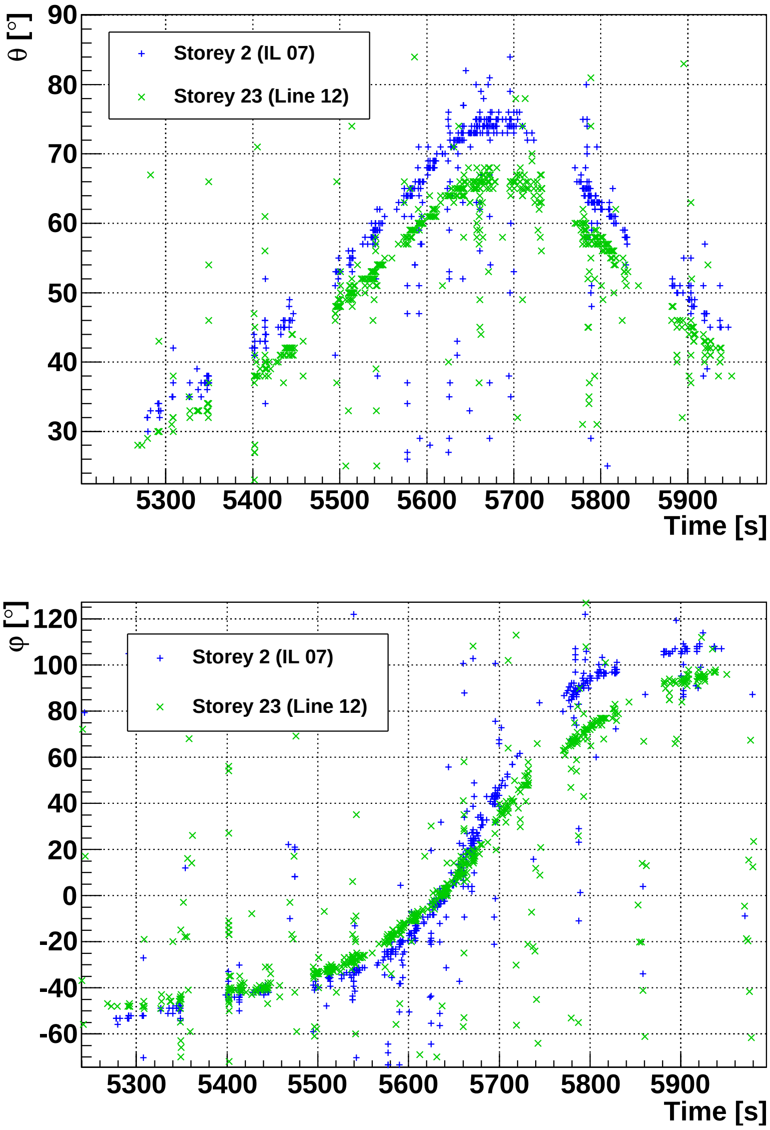

Figure 8.6: Zenith (θ) and azimuth angle (φ) as a function of time of a moving emitter. The plotted data are used for the source position reconstruction presented in Fig. 8.7. The time scale refers to the time elapsed since the start of the data taking run.

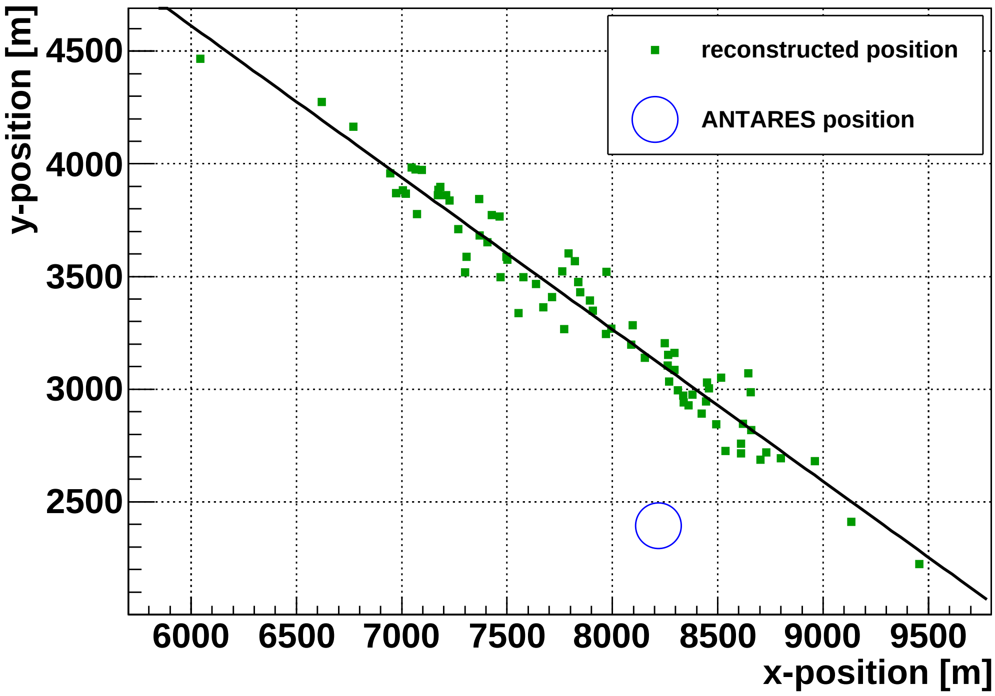

Figure 8.7: Reconstructed positions of a moving source passing the ANTARES detector The emitter moves at a constant speed of 12 knots. A straight line was fitted to the data to guide the eye.

8.6 Spatial distribution of transient signals

The capabilities of the AMADEUS system with respect to source location reconstruction have been presented in the previous sections. Both stationary and moving emitters can be identified and their location determined. With these capabilities proven to work the spatial distribution of signals with bipolar content was analysed. As mentioned in Sec. 7.1, signals recorded by the AMADEUS system are identified allowing for analysing a special signal type.
Bipolar signals are identified by cross correlating the recorded data with a signal template[1] and applying a threshold to the cross-correlated signal. A known problem of this simple signal identification technique is that it selects all signals with bipolar content above a predefined threshold (2.5·RMS). Unfortunately, a large number of signals, such as a sinusoidal signal, have bipolar content resulting in a large number of signals identified as bipolar. More sophisticated signal classification techniques, taking into account more signal characteristics, are currently being investigated but are not available for this work.

[1] A signal template in this case refers to an exemplary signal as expected from a neutrino-induced acoustic pulse, see Fig. 4.1.

Using the data set containing signals with bipolar content, their spatial distribution was examined. This was done by reconstructing all signals of this data set with an amplitude exceeding four times the RMS of the noise at the time, resulting in an average threshold of about 40 mPa. To obtain an appropriate estimate for the signal source distribution, data from a total time period of 700 hours were analysed, resulting in a total of $270,000$ reconstructed events in a volume of 4 km^3. This volume is defined by a square of 2×2 km in the horizontal plane, with the centre of the acoustic system in its centre, and a height of 1 km with the sea bed as its lower bound.
Figure 8.8 shows the reconstructed signal source positions. A large number of reconstructed positions are within or in direct vicinity of the ANTARES detector. Further away from the detector the density of reconstructed sources clearly decreases. The density of reconstructed signal ori-

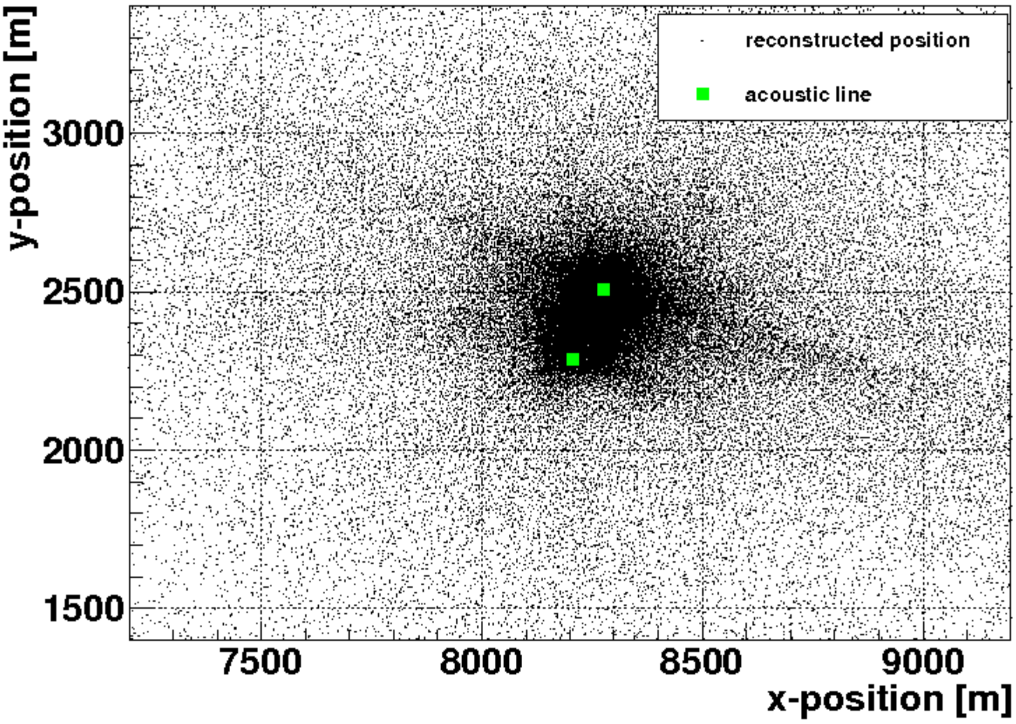

Figure 8.8: Reconstructed source locations in the vicinity of the ANTARES detector. A decrease of the density of reconstructed signals with distance from the detector can clearly be seen. The positions of the Lines equipped with acoustic sensors are marked by green squares. (Coordinates in UTM)

gins with bipolar content as a function of the distance to the detector centre is shown in Fig. 8.9. In the centre of the detector the density of signals is the highest and decreases with distance from the detector, as could already be seen in Fig. 8.8. The kink in the signal source density presented in Fig. 8.9 correlates with the boundaries of the detector indicating the detector being a source itself. This is likely to be a result of both detector-created signals and reflections from the detector structures. Figure 8.9 also shows a signal source density calculated for a subset of the presented data consisting of signal durations of $< 50\,\mu$s. Given the threshold for this analysis a signal duration of $< 50\,\mu$s is a reasonable requirement, see Fig. 4.1. Requiring this maximum signal duration reduces the amount of reconstructed signal source positions from $270,000$ to $150,000$ in the given volume and thus the signal source density. The shape of the signal source density function remains unchanged. For this subset, signals with a duration of $< 50\,\mu$s, additional cuts were applied corresponding to signal amplitudes as produced by neutrino-induced cascades with energies $E_{casc} < 5 \times 10^{20}$, $< 5 \times 10^{19}$ and $< 5 \times 10^{18}$ eV. For greater distances only signals with large amplitudes were detected, signal amplitudes corresponding to a neutrino-induced cascade of $E_{casc} < 5 \times 10^{18}$ eV were only detectable within the boundaries of the detector.

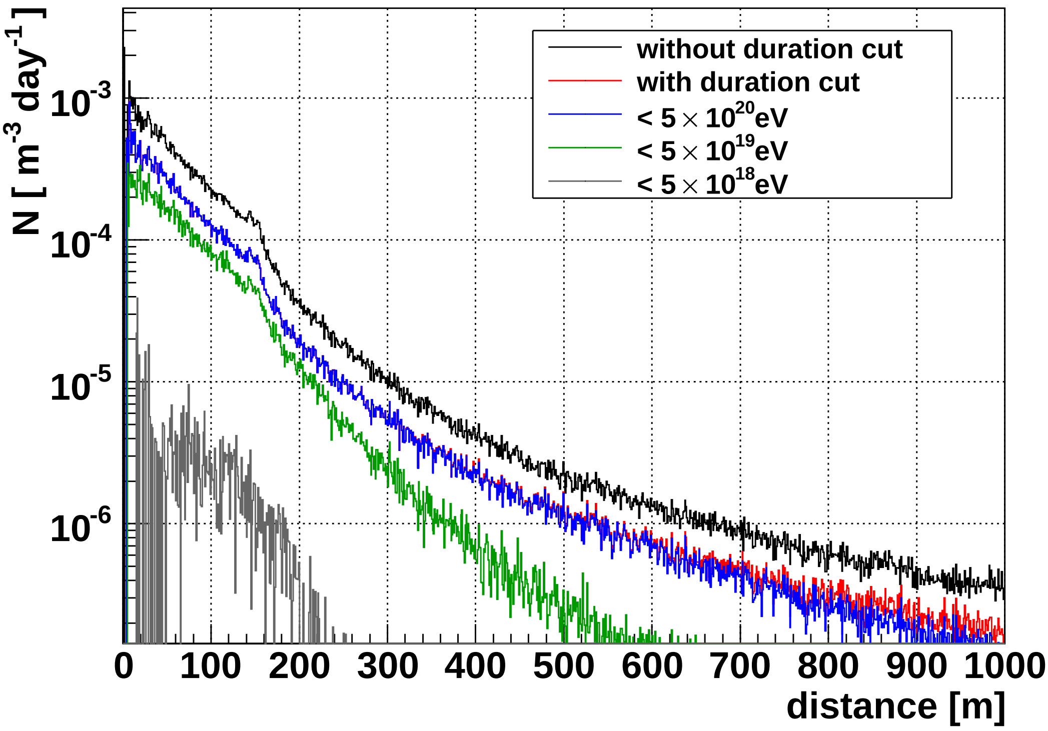

Figure 8.9: Mean density of bipolar like signals as a function of the distance from the centre of the acoustic system for the time period October 2008. The kink in the density also marks the boundary of the detector. Signal source densities were calculated for all reconstructed signals (without duration cut), for a subset including signals of $< 50\,\mu$s duration (with duration cut) and for signals amplitudes corresponding to a neutrino-induced cascade energy of $< 5 \times 10^{20}$eV, $< 5 \times 10^{19}$eV and $< 5 \times 10^{18}$eV. The amplitude selection was applied the data only containing signals with a duration of $< 50\,\mu$s.

Taking a look at the signal amplitudes as a function of the time (see Fig. 8.10), a number of spikes can be seen. These spikes are correlated to emitters, such as ships, passing the detector. The large amount of signals in direct vicinity of the detector are also due to reflections on the structures of the detector, as indicated by the data presented in Fig. 8.11. Figure 8.11 shows

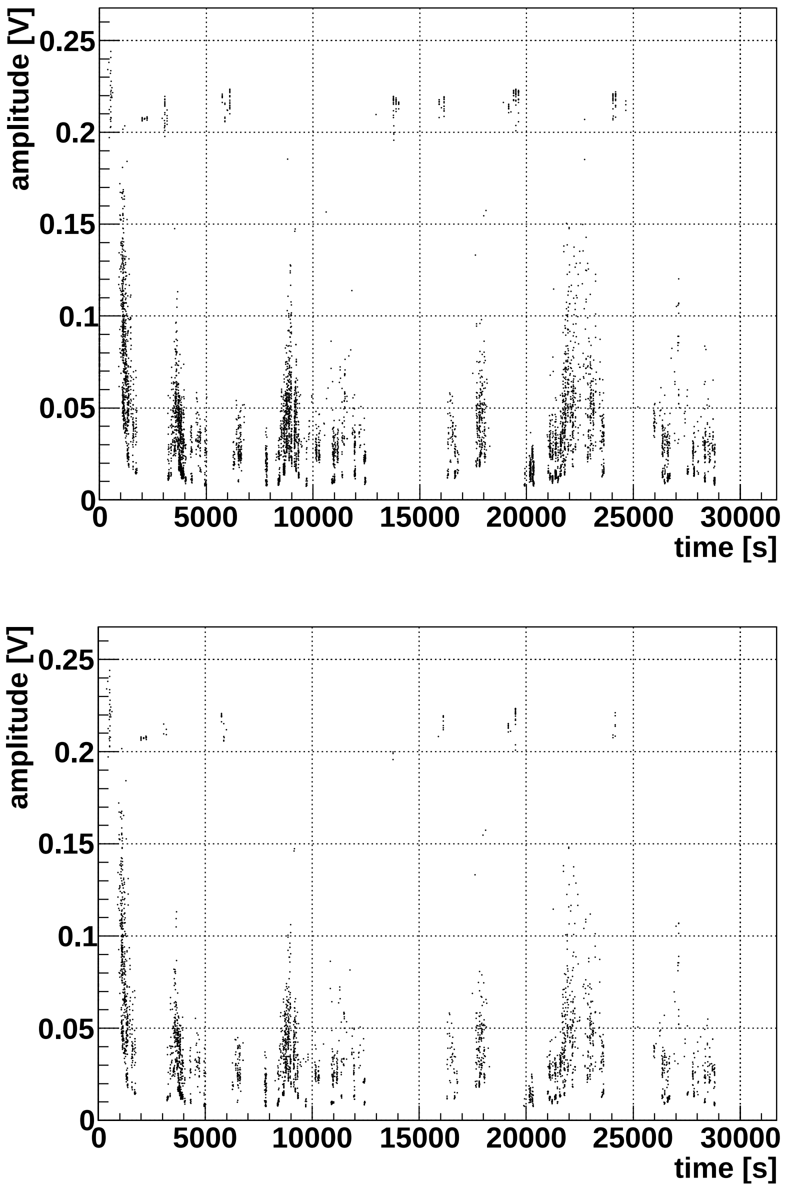

Figure 8.10: Amplitudes of detected signals as a function of time. Top: without a signal duration cut. Bottom: with a duration cut.

the reconstructed source positions around the detector for the time between 8000 s and 10000 s in Fig. 8.10, which contains a spike. The reconstructed positions near the surface are coded in a different colour to show a track which would otherwise be hard to spot in this projection. The presence of this source is accompanied by a number of other signals mainly originating from within the detector. For the density calculation the signals from this surface source are not included, but the potential reflections are. Applying a signal duration cut of 50 μs reduces the

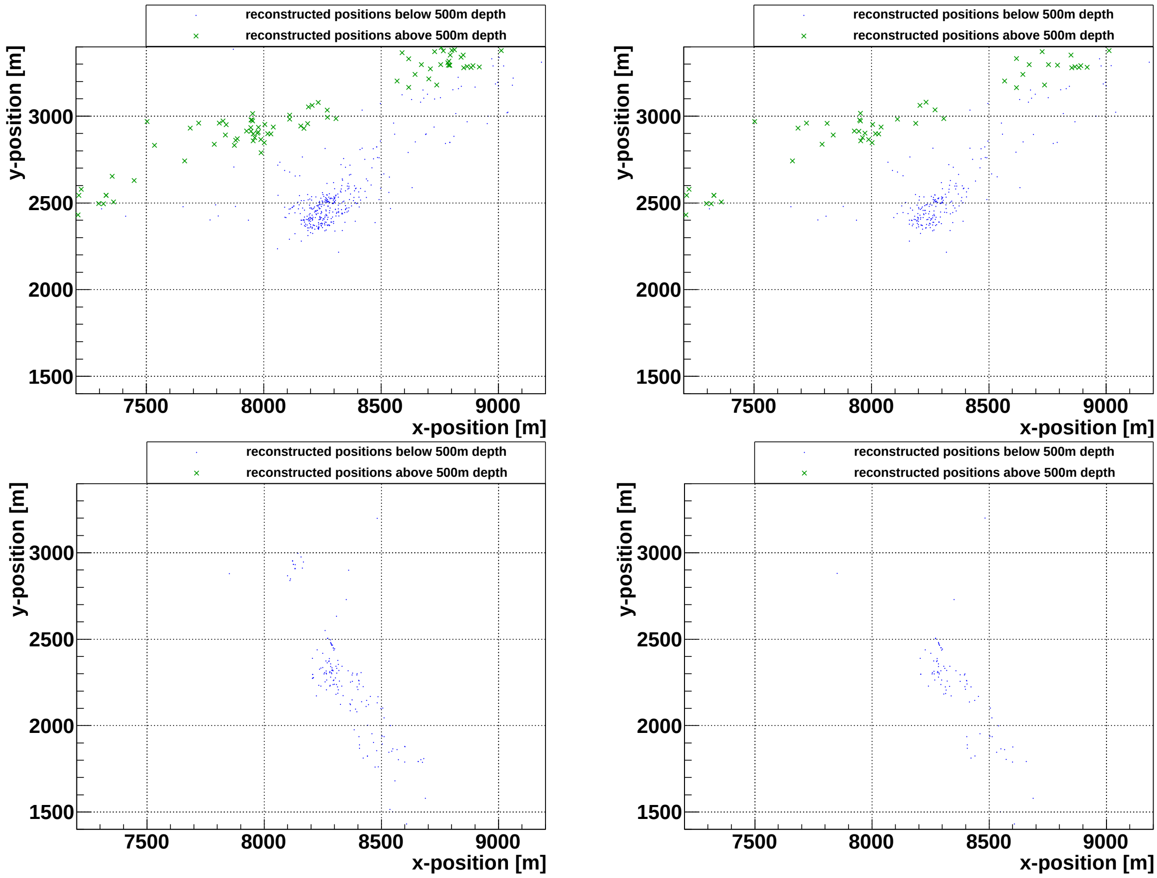

Figure 8.11: Top left: Reconstructed source positions for the time between 8000 s and 10000 s of the data presented in Fig. 8.10. Top right: The same data with an additional signal time duration cut of 50 μs. Bottom left: Reconstructed source positions for the time between 5000 s and 7000 s of the data presented in Fig. 8.10. Bottom right: The same data with an additional signal time duration cut of 50 μs.

overall number of signals but the basic picture remains unchanged. The reconstructed positions of a more quiet time period (between 5000 s and 7000 s), also shown in Fig. 8.11, shows a lower signal density and indicate a correlation between signals inside the detector and outside sources, since no track was reconstructed. For this sample no surface source was detected.
The reduction of signal sources by applying a signal duration cut hints the potential of signal classification. With more sophisticated signal classification techniques a further reduction in the number of signal sources is very likely, but one also has to consider choosing an acoustically cleaner location when planning a future acoustic neutrino detector. While this detector is very

close to shipping routes as presented in Figs. 8.11, 8.7, 7.5 a location further from such routes would most likely reduce the amount of detected signals. Given a maximum detection distance of about 30 km for such sources a distance from standard shipping routes greater than this value would be required in case signal identification techniques do not prove to be effective enough. If signal identification proves effective a low noise environment will result in a more efficient detector.

Chapter 9

Summary

The work presented here is about acoustic particle detection, a possible alternative to optical detection of highly energetic neutrinos. It is based on the principle of a neutrino induced particle cascade depositing its energy in a medium, thus heating the medium, water in this case. The rise in temperature causes the medium, depending on its properties, to either expand or contract thereby producing a bipolar pressure wave which can then be detected by sensors. Signal amplitudes produced by this mechanism roughly scale with $A \sim 10\,\mathrm{mPa} \cdot E_{casc}/1\,\mathrm{EeV}$ at a distance of 200 m from the cascade, where E_{cas} represents the energy of the cascade. Depending on the background these signals can be detected and used to study particle interactions at high energies. In order to investigate the feasibility of acoustic particle detection the water Cherenkov detector ANTARES, located 30 km off the coast of France in the Mediteranean Sea at a depth of 2500 m, was additionally equipped with acoustic sensors, the AMADEUS system. It consists of 36 sensors distributed in six local cluster of six sensors each. The goal of the acoustic system AMADEUS is to investigate the acoustic background with respect to short and long term variations, study the rate of signals mimicking neutrino interactions and to investigate source direction and source position reconstruction techniques. These goals are all essential in order to assess the feasibility of an acoustic particle detector in water. The energy threshold is dependent on the background level, its mean at the ANTARES site is $\sim 10\,\mathrm{mPa}$ thus defining an energy threshold of $\sim 1\,\mathrm{EeV}$. Background levels of the AMADEUS system were correlated with the wind-speed above the ANTARES detector giving a correlation coefficient of $\sim 80\%$. While background surveys can be achieved with a single sensor, direction and source location reconstruction requires the evaluation of the data of several sensors. One focus of this work was to evaluate direction reconstruction techniques making use of local clusters each consisting of six hydrophones in a volume of $\sim 1\,\mathrm{m}^3$. Local clusters allow for a quick and accurate direction reconstruction of a transient signal. The techniques evaluated are a beam-forming and a time difference based algorithm, both assuming a plane wave propagation of the acoustic signal. This is valid given the dimensions of the clusters. Beam-forming is achieved by shifting the data recorded by each sensor within a cluster in the time domain and taking the sum of all six sensors. Each direction corresponds to set of time shifts, creating an antenna sensitive to one direction. To identify the direction of a signal the entire solid angle is scanned in 1° steps and the maximum amplitude given for every analysed direction stored. The signal direction is then given by the global maximum of this scan, the direction for which all signals add up constructively. This method works very well and has the advantage of not requiring the identification of a transient signal, a major draw back of this method is the long computation time necessary. Another method rendering the same results works by analysing the signal detection times for each sensor within a cluster. The detection times, defined by the passing of a threshold, are compared to expected signal arrival times for each direction. The signal direction is defined by the minimum of this comparison. Given the same angular resolution using signal detection times is about 100 times faster than the previously introduced beam-forming method making it the primary direction method used for data analysis. Both methods require the precise knowledge of the relative positions of the sensors within a cluster, which were measured before the deployment of the AMADEUS system. The angular resolution of the direction reconstruction is about 3° in the azimuthal and less than 1° in the zenith angle. The components of the ANTARES detector are attached to a cable anchored to the sea floor and held upright by a buoy resulting in two degrees of freedom, rotation and tilt, caused by the sea current. The resolution in the azimuthal angle is dependent on the knowledge of the orientation, which is afflicted with an error of about 1.4°, and the position of the storey, about 20 cm accuracy, thus leading to the azimuthal angular resolution mentioned above. Since the currents are relatively low at the ANTARES site ($\sim$ 5m/s) the storeys are hardly displaced from their upright position thus resulting in a zenith resolution that is governed by the binning of the algorithm.

Signals detected by the AMADEUS system mainly originate from the upper hemisphere ($\sim$ 80%) and most of these are likely to be of biological or mechanical origin. The direction reconstruction capabilities were also demonstrates by tracking moving emitters.

Given the directional information provided by each cluster of hydrophones the position of a source can be identified. It is given by the intersection point of the lines defined by the position of each cluster and the identified direction. Simulations studies of the source location reconstruction method, presented in this work, determined an error in the order of 5 m in close vicinity of the detector, increasing with distance and reaching about 25 m at 1 km from the detector centre. The actual error, determined with the help of known emitter positions, was found to be $\sim$ 6 m for sources within the volume of the ANTARES detector, in good agreement with the simulation results. The capabilities of the AMADEUS system with regard to source reconstruction were impressively demonstrated by tracking a moving emitter at the sea surface at a distance of up to three kilometres.

Finally a density of signals with bipolar content at the ANTARES site was derived indicating a decreasing number of signals with the distance from the detector and identifiying the detector as a source itself.

While one key element, the identification of signals is still a work in progress, another, the source location reconstruction of transient signal, has proven to work very well. Source reconstruction has very much benefited from the use of local clusters as they allow for quick direction reconstruction minimizing the time window needed to be processed, and greatly simplifying source location reconstruction. The benefit of these local clusters clearly out-weights the additional costs of the extra sensors making a design similar to the AMADEUS local clusters the ideal choice for a future acoustic neutrino detector.

Chapter 10

Zusammenfassung

Die hier präsentierte Arbeit beschäftigt sich mit akustischer Teilchendetektion, eine mögliche Alternative zur optischen Detektion von hochenergetischen Neutrinos. Diese Methode basiert auf dem Prinzip, dass ein in einem Medium wechselwirkendes Neutrino eine Teilchenkaskade erzeugt, welche ihre Energie lokal deponiert und damit das Medium, Wasser in unserem Fall, erhitzt. Die lokale Erwärmung erzeugt eine Kontraktion bzw. Expansion, abhänging von den Eigenschaften des Mediums, und damit ein bipolares Signal, welches mittels Sensoren detektiert werden kann. Die Amplituden der erzeugten Signale skalieren mit $A \sim 10\,\mathrm{mPa} \cdot E_{casc}/1\,\mathrm{EeV}$ bei einem Abstand von 200 m von der Kaskade wobei E_{casc} die Energie der Kaskade bezeichnet. Abhänging vom Hintergrund können diese Signale genutzt werden um Teilchenwechselwirkungen bei hohen Energien zu untersuchen.
Um die Machbarkeit der akustischen Teilchendetektion zu untersuchen, wurde der Wasser-Cherenkov Detektor ANTARES, errichtet im Mittelmeer in 2500 m Tiefe 30 km südlich der französischen Küste, zusätzlich mit akustischen Sensoren bestückt. Das so genannte AMADEUS System besteht aus 36 Sensoren verteilt auf sechs lokale Cluster. Das akustische System wurde errichtet um den Untergrund bzgl. lang- und kurzzeitiger Korrelationen zu untersuchen, die Rate neutrinoähnlicher Signale zu bestimmen und Techniken zur Signalrichtung sowie Ursprungsortsbestimmung zu untersuchen. Diese Studien sind notwendig um die Machbarkeit der akustischen Teichendetektion zu beurteilen. Der akustische Untergrund am ANTARES Detektor ist stark mit der Windgeschwindigkeit über dem Detektor korreliert (Korrelationskoeffizient von ca. 80%). Im Mittel beträgt der Untergrund am Standort des ANTARES Detektors ca. $\sim 10\,\mathrm{mPa}$ und bestimmt damit eine Energieschwelle von $\sim 1\,\mathrm{EeV}$. Für die richtungsunabhängigen Untergrundstudien genügt ein einzelner Sensor während Richtungs- sowie Quellortsbestimmung die Verwendung mehrere Sensoren bedarf. Ein Fokus dieser Arbeit ist die Untersuchung von Methoden zur Signalrichtungs- sowie Quellortsbestimmung mittels lokaler Cluster, welche aus jeweils sechs Sensoren in einem Volumen von $\sim 1\,\mathrm{m}^3$ bestehen. Lokale Cluster bieten den Vorteil einer schnellen und präzisen Richtungsrekonstruktion eines transienten Signals. Die hierfür untersuchten Methoden sind ein Beam-forming und ein Zeitdifferenzen basierter Algorithmus, beide ausgehend von einer ebenen Welle. Diese Annahme ist angemessen in Betracht der hier zugrundeliegenden Dimensionen der Cluster. Beam-forming ist realisiert indem die aufgenommenen Daten der einzelnen Sensoren innerhalb eines Clusters zeitlich zu einander ver-

schoben und dann addiert werden. Diese Operation erzeugt eine Antenne die sensitiv auf eine Richtung in Abhängikeit der Zeitverschiebung ist. Um die Richtung eines Signals zu bestimmen wird der gesamte Raumwinkel in 1° Schritten gescannt und die maximale Amplitude für jede Richtung gespeichert. Die Richtung des Signals ist durch das globale Maximum, die Richtung für jene alle Signale konstruktiv interferieren gegeben. Diese Methode funktioniert äußerst gut und hat den Vorteil keine Signalidentifikation zu benötigen. Eine Nachteil ist die beanspruchte Rechenzeit. Eine andere Methode, welche die selben Resultate liefert, basiert auf der Analyse der Signalankunftszeiten an den einzelnen Sensoren innerhalb eines Clusters. Die Ankunftszeiten, definiert durch einen Schwellwert, werden mit erwarteten Ankunftszeiten verglichen. Die Signalrichtung wird hierbei durch den Minimalwert dieses Vergleichs bestimmt. Mit gleicher Winkelauflösung ist diese Methode ca. 100 mal schneller als die Beam-forming Methode. Die Zeitdifferenzenmethode stellt damit die erste Wahl dar. Beide Methoden benötigen die exakten Positionen der Sensoren innerhalb eines Clusters, welche vor der Ausbringung des AMADEUS Systems bestimmt wurden. Die Winkelauflösung der Richtungsrekonstruktion ist ca. 3° für den Azimut- und etwas weniger als 1° für den Zenitwinkel. Da die Komponenten des ANTARES Detektors an einem am Meeresboden verankerten und durch eine Boje aufrecht gehaltenem Kabel montiert sind verbleiben ihnen zwei Freiheitsgrade der Bewegung, Rotation in Längs- und Querachse, hervorgerufen durch die Meeresströmung. Die Winkelauflösung für den Azimutwinkel ist abhängig von der Kenntnis der Ausrichtung, welche mit einem Fehler von 1.4° behaftet ist, und dem Ort, ca. 20 cm Unsicherheit, des Clusters. Da die Strömungsgeschwingikeit am ANTARES Standort relativ gering ist ($\sim$ 5m/s) werden die Cluster kaum von ihrer aufrechten Lage verdrängt was dazu führt dass die Auflösung primär vom Binning des verwendeten Algorithmuses abhängt.

Signale die durch das AMADEUS System detektiert wurden kommen hauptsächlich von der oberen Hemisphäre ($\sim$ 80%) und stammen mit hoher Wahrscheinlichkeit von mechanischen und biologischen Quellen. Die Richtungsrekonstruktionsfähigkeiten des Systems wurde unter anderem mit der Verfolgung bewegter Quellen demonstriert.

Mittels der Richtungsinformation einer Mehrzahl von Clustern von Hydrophonen und deren Positionen kann der Quellort eines Signals bestimmt werden. Er ist durch den Schnittpunkt, der durch den Ort und die Richtung aufgespannten Geraden der einzelnen Cluster gegeben. Durch, in dieser Arbeit demonstrierte, Simulationen der Quellortsbestimmungsmethode wurde eine Unsicherheit von ca. 5 m in der näheren Umgebung des ANTARES Detektors, welche mit dem Abstand zum Detektor auf 25 m bei einem Abstand vom 1 km zunimmt, ermittelt. Die eigentliche Unsicherheit, ermittelt mithilfe des Positionierungssystems des ANTARES Detektors, beträgt $\sim$ 6 m für Quellen in der Nähe des Detektors, was in guter Übereinstimmung mit den Simulationsdaten ist. Die Möglichkeiten des AMADEUS System wurde auch eindrucksvoll anhand einer bewegten Oberflächenquelle demonstriert.

Zum Schluss wurde eine Quelldichte für Signale mit bipolaren Anteil in der Umgebung des ANTARES Detektors bestimmt, welche einen hohen Anteil der Quellen im Detektor zeigt und mit steigendem Abstand abnimmt.

Während ein Schlüsselelement, die Klassifizierung transienter Signale, noch in der Entwicklungsphase steckt, kann die Ortsbestimmung als fortgeschritten betrachtet werden. Die Ortsbestimmung, wie sie hier präsentiert wurde, profitiert stark von der Verwendung lokaler Cluster, da diese eine effiziente Richtungsrekonstruktion ermöglichen und damit eine Ortsbestimmung deutlich vereinfachen. Der Vorteil der durch diese Cluster entsteht übertrifft bei weitem die zusätzlichen finanziellen Kosten und stellt damit ein wichtiges Element für einen zukünftigen akustischen Neutrinodetektor dar.

Bibliography

[1] Gene Roddenberry. Star Trek. NBC, 1966.

[2] Viktor F. Hess. Über Beobachtungen der durchdringenden Strahlung bei sieben Freiballonfahrten. *Physik. Zeitschr.*, XIII:1084–1091, 1912.

[3] F. Reines and C.L. Cowan. The Neutrino. *Nature*, 178:446–449, 1956.

[4] C. L. Cowan, F. Reines, F. B. Harrison, H. W. Kruse, and A. D. McGuire. Detection of the free neutrino: A Confirmation. *Science*, 124:103–104, 1956.

[5] Raj Gandhi, Chris Quigg, Mary Hall Reno, and Ina Sarcevic. Neutrino interactions at ultrahigh energies. *Physical Review D*, 58:093009, 1998.

[6] Constantino Tsallis, Joao C. Anjos, and Ernesto P. Borges. Fluxes of cosmic rays: A delicately balanced stationary state. *Physics Letters A*, 310:372, 2003.

[7] NASA. http://www.nasa.gov/centers/goddard/news/topstory/2007/active-galaxy-prt.htm, 2007.

[8] Kenneth Greisen. End to the cosmic ray spectrum? *Phys. Rev. Lett.*, 16:748–750, 1966.

[9] G. T. Zatsepin and V. A. Kuzmin. Upper limit of the spectrum of cosmic rays. *JETP Lett.*, 4:78–80, 1966.

[10] J. *et al.* Abraham. Measurement of the energy spectrum of cosmic rays above 1 EeV using the Pierre Auger Observatory. *Phys. Lett.*, B685:239–246, 2010.

[11] C.L. Naumann. *Development of Sensors for the Acoustic Detection of Ultra High Energy Neutrinos in the Deep Sea*. PhD thesis, Univ. Erlangen-Nürnberg, 2007.

[12] M. Neff. Studie zur akustischen teilchendetektion im rahmen des antares-experiments: Entwicklung und integration von datennahmesoftware, 2007.

[13] G. A. Askarian. *At. Energ.*, 3:152, 1957.

[14] G. A. Askarian, B. A. Dolgoshein, A. N. Kalinovsky, and N. V. Mokhov. Acoustic detection of high energy particle-showers in water. *Nucl. Instrum. Meth.*, 164:267–278, 1979.

[15] Kay Graf. Teststrahlmessungen zur akustischen Neutrinodetektion: Thermoakustische Schallerzeugung in Wasser, July 2004. FAU-PI1-DIPL-04-002.

[16] K. Graf, G. Anton, J. Hößl, A. Kappes, T. Karg, U. Katz, R. Lahmann, C. Naumann, K. Salomon, and C. Stegmann. Testing thermo-acoustic sound generation in water with proton and laser beams. Presented at the 1st International ARENA Workshop, DESY Zeuthen, Germany, May 17-19, 2005.

[17] R. Nahnhauer, (ed.) and Sebastian Boeser, (ed.). Acoustic and radio EeV neutrino detection activities. Proceedings, International Workshop, ARENA 2005, Zeuthen, Germany, May 17-19, 2005. *IOP*, 2006. Prepared for International Workshop on Acoustic and Radio EeV Neutrino Detection Activities (ARENA 05), Zeuthen, Germany, 17-19 May 2005.

[18] S. Bevan *et al.* Simulation of ultra high energy neutrino interactions in ice and water. *Astro. Part. Phys.*, 28(3):366, 2007. arXiv:astro-ph/0704.1025v1.

[19] Timo Karg. Detection of ultra high energy neutrinos with an underwater very large volume array of acoustic sensors: A simulation study, 2006. arXiv:astro-ph/0608312.

[20] Chen and F.J. Millero. Speed of sound in seawater at high pressures. *Acoust. Soc. Am.*, 62(5):1129–1135, 1977.

[21] Nikolai G. Lehtinen, Shaffique Adam, Giorgio Gratta, Thomas K. Berger, and Michael J. Buckingham. Sensitivity of an underwater acoustic array to ultra-high energy neutrinos. *Astropart. Phys.*, 17:279–292, 2002.

[22] C. Richardt. Acoustic particle detection: Strategies for data reduction and point source reconstruction, 2006.

[23] Sean Danaher. First data from ACoRNE and signal processing techniques. *J. Phys. Conf. Ser.*, 81:012011, 2007.

[24] S. Brehm. Studien zur positionsbestimmung der akustischen antares-stockwerke, 2009.

[25] M. Ardid for the ANTARES Coll. Positioning system of the antares neutrino telescope. *NIM*, A 602:174, 2009.